LAGUERRE MODELS FOR GRAIN GROWTH

THÈSE N° 1466 (1995)

PRÉSENTÉE AU DÉPARTEMENT DE MATHÉMATIQUES

ÉCOLE POLYTECHNIQUE FÉDÉRALE DE LAUSANNE

POUR L'OBTENTION DU GRADE DE DOCTEUR ÈS SCIENCES TECHNIQUES

PAR

Xinjian XUE

MSc in Engineering, Shanghai University of Technology

de nationalité chinoise

acceptée sur proposition du jury:

Prof. Th. M. Liebling, directeur de thèse
Prof. A. Mocellin, corapporteur
Prof. M. Rappaz, corapporteur
Dr F. Righetti, corapporteur
Dr H. Telley, corapporteur

Lausanne, EPFL
1996

Acknowledgments

First of all, I am deeply grateful to Prof. Th.M. Liebling for having provided the facilities and environment for the completion of this work in his chair. I owe him special thanks for his support, understanding and stimulating discussion. I would like to thank him for his guidance during my studies in Lausanne, not only limited to the research field, which will always remain fresh in my memory.

I would like to express my deep gratitude to Prof. A. Mocellin for leading me to the world of materials science and for his invaluable tutoring and encouragement. I am grateful to Prof. M. Rappaz for having critically reviewed this thesis. Special thanks are due to Dr. H. Telley and Dr. F. Righetti for their cheerful collaboration and for sharing their experience in the dynamic Laguerre diagram and grain growth simulation. Actually, it is following their steps that I am entering the tessellated space.

I am also grateful to all my committee members for carefully proofreading my thesis and providing constructive criticism.

I very appreciate the chance to converse about our work with Prof. N. Rivier at Université de Strasbourg, Prof. M.A. Fortes at Instituto Superior Técnico, Lisbon, Prof. S. Kurtz at the Pennsylvania State University, Prof. K. Lücke at RWTH, Aachen, and Prof. A. Ecer and Prof. H. Akay at Purdue University. These discussions helped me discover some of the possible research problems I need to address as well as future application areas of our Laguerre model.

I am greatly indebted to all my colleagues for the very friendly atmosphere in our chair. I am not forgetting you all: Dr. A. Prodon, Dr. V. Delaloye, Mr. D. Didier, Miss Ch. Lütolf, Mr. N. Moeri, and all my chair-mates for all the heuristic and intellectual conversations. I would like to thank Dr. F. Shen for having read this manuscript.

Last but not least, I would like to thank my family who are always supportive and caring.

Résumé

Les métaux, alliages et céramiques sont des matériaux polycristallins dont la structure de base est le grain. On appelle la surface de contact entre les grains le joint. Avec une condition convenable de recuit, c'est-à-dire un temps suffisamment long et une température suffisamment élevée, les grains vont grandir, donc, la structure microscopique va changer au cours du temps. Dans ce processus, appelé la croissance de grains, la taille moyenne de ceux-ci augmente mais le volume du matériau est conservé. La force de croissance est le résultat de la diminution de l'énergie de joint qui accompagne la réduction de l'aire totale de joint.

Dans l'étude des matériaux polycristallins, un des buts fondamentaux est la prévision complète du développement de la structure microscopique étant donné les conditions de recuit. Ces deux dernières décennies, la simulation informatique a été appliquée pour tenter d'expliquer l'interaction des grains dans ce processus.

Sur la base des travaux de Telley et Righetti, nous avons poursuivi le devéloppement du diagramme de Laguerre dynamique dans le tore unité plat en trois dimensions. Un amas de grains est idéalisé comme un diagramme de Laguerre dans l'éspace. Une équation définissant le mouvement des sites pondérés du diagramme de Laguerre est déduite du principe de migration des joints proposé par Burke et Turnbull. Pour simuler ce processus, le temps est discrétisé et l'équation est approchée linéairement par morceaux. Donc, la position et le poids du site changent linéairement dans un intervalle de temps suffisamment petit. Les transformations topologiques induites par ce mouvement sont déterminées et réalisées dans un ordre approprié. Pour suivre l'évolution du diagramme, l'équation du mouvement de chaque site est mise à jour dans l'intervalle de temps. Nous avons tenu compte d'hétérogénéité de l'énergie de joint. Les résultats de la simulation montrent que les caractéristiques principales de ce processus physique, à savoir la loi de puissance de croissance des grains, la distribution de la taille et de la forme des grains et le comportement de la distribution sont reproduits assez fidèlement.

Pour simuler le processus de croissance des grains accompagné du dévelopement d'une texture, le modèle de Laguerre en deux dimensions a été étendu au cas impliquant seulement deux types de grains. Les essais de simulation correspondants ont reproduit le comportement cinétique du processus et produit des exemples de microstructures représentatives. En plus, par la simulation de longue durée, un comportement oscillatoire du processus a pu être mis en évidence sous certaines conditions. Donc, le modèle de Laguerre ainsi élargi offre un complément important au modèle statistique proposé par Abbruzzese et Lücke.

Abstract

Most metals, alloys and ceramics are polycrystalline materials in which the basic microstructure is the grain and grain boundary. Under suitable annealing condition, i.e., a sufficiently long time and a sufficiently high temperature, the grains grow and therefore the microstructure changes over time. Such a process in which the mean grain size increases and the volume of material is conservative is called grain growth. The driving force for the growth results from the decrease of interfacial energy which accompanies reduction of total grain boundary area.

A major objective in materials science is the complete prediction of microstructural development in polycrystalline materials as a function of annealing condition. For the last two decades, computer simulation has been applied in order to describe this complex process of grain interaction.

In this study, based on Telley and Righetti's work, the dynamic Laguerre diagram defined in the three-dimensional unit flat torus is further developed. An aggregate of polycrystalline grains is idealized as a Laguerre diagram in space. Based on Burke and Turnbull's grain boundary migration principle, an equation which governs the motion of weighted sites of a Laguerre diagram is derived. For computer simulation, time is discreterized and the equation is piecewisely linearized. In consequence, the position and weight of the site linearly change in a sufficiently small time interval. The topological transformations induced by the motion are determined and performed in an appropriate order. To follow up the evolution of the diagram, the motion equation of each site is updated in the time interval. The anisotropy of grain boundary energy depending on the misorientation of grain boundaries has been taken into account. Simulation results show that the main attributes of the physical process, i.e., the grain growth power law, the distributions of grain size and shape and the scaling behavior of the distribution are reproduced by the mathematical model.

To simulate the texture developing grain growth process, Telley's 2D Laguerre model for isotropic normal grain growth in single phase system has been extended to the heterogeneous case. The simplest textured grain growth, i.e., two texture components present in a grain system, has been simulated. The model has reproduced the kinetic behavior of the process and brought to light the evolution of microstructure of the simulated material. Moreover, by long time simulations, the possibility of long-term oscillation of the process has been evidenced for the first time. Thus, the extended 2D Laguerre model can be looked as an important complement of Abbruzzese and Lücke's statistical model.

Contents

List of Figures

Chapter 1

Introduction

Most metals, alloys and ceramics have a crystalline structure. Namely, their atoms are arranged in a periodically repeating geometrical array, or are long range ordered. If the long range order exists over distance of $0.1mm$ in a metallurgical system or so, in other words, the ordered region is very large compared to the atomic spacing ($2\mathring{A}= 2 \times 10^{-10}m$), then the term "long range" can be applied. Each ordered region is called a crystal or grain and the interface between crystals is called crystalline boundary or grain boundary, while the entire solid is termed polycrystal. The lattice level microstructure of a polycrystal is schematically illustrated in Figure 1.1 in two dimensions (from [And85]). Less microscopically, in Figure 1.2, the geometrical and topological character of grain and its boundary is exemplified. This picture is a micrograph of a specimen of titanium dioxide ceramic TiO_2 (from [Car87]).

Since macroscopic properties of polycrystalline materials, such as mechanical strength, toughness, electrical conductivity and magnetic susceptibility strongly depend on the materials' microstructure, understanding of the microstructure and its evolution is thus of fundamental importance, not only for its intrinsic interest, but also for its technological significance [Cot76]. In polycrystalline materials, the most significant microstructural features are grains and boundaries. It is well known that after recrystallization all grains are formed and may keep on growing under suitable annealing conditions (temperature, pressure, time duration and so on), meanwhile the volume of the materials is conservative. Therefore, such growth is an average grain size increasing and the number of grains decreasing process which can be further classified as normal and abnormal. The former is generally characterized by two main attributes:

(i) Uniform appearance – there is a relatively narrow range of grain sizes and shapes;

(ii) Scaling – the form of the distribution of the normalized grain size (i.e., the grain size normalized by the mean grain size) and grain shape is time-invariant.

The process has been investigated in a wide variety of materials from pure metals to complex alloys up to technical ceramics.

In a classic paper of the early 1950, Burke and Turnbull [Bur52] derived a parabolic relationship for the average grain growth kinetics. They modeled the migration of a

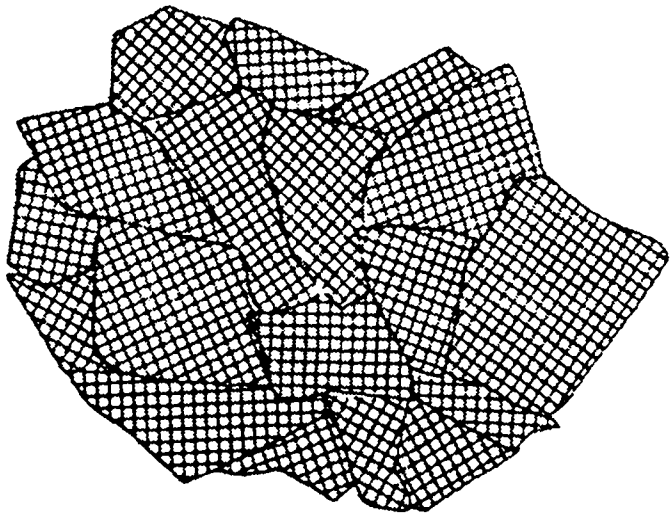

Figure 1.1: Schematic illustration of polycrystal (from [And85]).

grain boundary as occurring by the transportation of atoms across the boundary under a pressure arising from the surface curvature. In their model, the surface curvature forces exerted on an isolated section of boundary tend to push it towards the curvature center thus reducing its area and hence the energy associated with it. In a pure single phase system, the velocity of boundary migration is equal to the product of its mobility and the curvature pressure. In another classic paper, Smith [Smi52] stated that the major theme in theoretical research on normal grain growth was the interplay between the topological requirements for space filling and the kinetics of change in the mean grain size with time, which in his own words is, "normal grain growth results from the interaction between the topological requirements (of space filling polyhedra) and the geometrical needs of surface tension equilibrium". In the last two decades, computer simulation has been playing a key role in exploring this interplay. A comprehensive review was given by Atkinson [Atk88] on the theories of isotropic grain growth in pure single phase system and 2D computer simulation methods. With the advent of sophisticated experimental techniques, recently has some improvement been achieved in understanding the fundamentals of grain boundary energy and mobility [Has71, Got92, Wol92]. It is now possible to simulate the process more precisely by considering the anisotropy of grain boundary energy and mobility in computer simulation model [And84, Kun93, Kaw93].

As the process inherently occurs in three dimensions, a proper simulation in its own space should allow one to clarify different theories and hypotheses on it. Here, the term "its own space" means the three dimensional unit flat torus, noted as $\mathbb{T}^3$, if the periodic boundary condition of an aggregate of crystals is considered. Because the typical behavior of an infinite aggregate of grains can be interpreted by that of a finite one in this space. As further idealization in computer simulation, a grain is represented as a polyhedron and an aggregate of grains as a complex of polyhedra. Among the known complexes of polyhedra, the Laguerre diagram nicely approaches to the grain system in the sense of

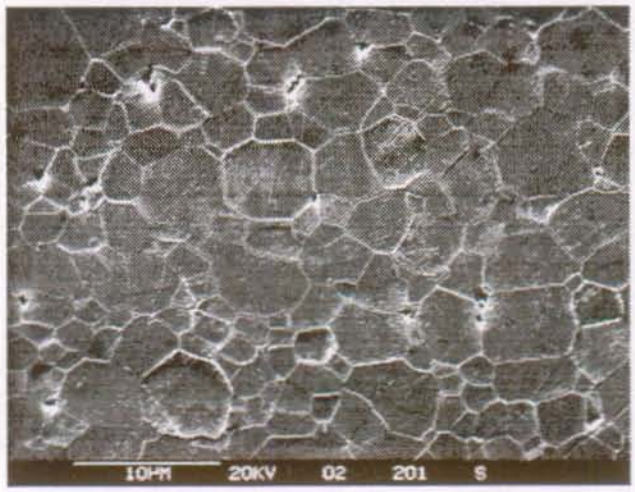

Figure 1.2: The microstructure of ceramics TiO_2 (from [Car87]).

geometry and topology [Tel89a].

Based on Telley's work on 2D dynamic Laguerre diagram [Tel89a, Tel90, Tel92b] and Righetti's work on construction of 3D Laguerre diagram [Rig92], a 3D dynamic Laguerre diagram and a corresponding maintenance algorithm are established in this study under mild degeneracy conditions. By the 3D dynamic Laguerre diagram, a 3D Laguerre model for normal grain growth [Tel89a] is established [Xue94]. Normal grain growth process in polycrystalline materials has been simulated by the model [Lie95, Xue95]. The dynamic Laguerre diagram defined in $\mathbb{T}^3$ provides a powerful tool to simulate dynamic cellular system. The ensuing 3D Laguerre model makes it possible to reproduce the process in its own space. Computational results show good agreement of the simulations with empirical data from real polycrystals, e.g., self-similarity, power growth law and so on.

The anisotropy of grain growth has been considered under Gottstein and Schwarzer's [Got92] assumption, i.e., the grain boundary energy depends on the simulated material crystallography and the misorientation of grains and the grain boundary mobility is isotropic. Under this assumption, 3D anisotropic grain growth has been simulated. The distribution of misorientation and its evolution have been measured.

The heterogeneous grain growth has been simulated under Abbruzzese and Lücke's [Abb86] assumption, i.e., only finite sorts of grains are present in a grain system. The grain growth in the system is called the texture developing grain growth process, as the crystallographic textures are likely to develop under such circumstance. 2D heterogeneous grain growth has been carried out in its simplest case, i.e., two texture components (or two types of grains) present in the system. Computational results provide not only the kinetic behavior of the process but also the microstructure of the cell system, which can be viewed as a complement to Abbruzzese and Lücke's statistical model's results [Abb86]. The possibility that under certain grain boundary specific energy matrices G, oscillatory competition between two populations of cells can arise has been clearly demonstrated by simulation.

This thesis is organized as follows. In Chapter 2, the principles of normal grain growth and available 3D simulation models are summarized and the development of Laguerre diagram is traced back to the seventeenth century. In Chapter 3, the dynamic Laguerre diagram defined in $\mathbb{T}^3$ and its maintenance algorithm are studied. In Chapter 4, the 2D Laguerre model is generalized into 3D. In Chapter 5, the 2D model is extended to the heterogeneous case. In these two chapters, our simulation results are compared to other simulation results and experimental data.

Chapter 2

Literature Review

In this chapter, the experimental observations and theoretical explanations on normal grain growth and three-dimensional computer simulation models are reviewed. The development of Laguerre diagram and its application in modeling and simulation of polycrystalline materials are summarized.

2.1 Principles of normal grain growth

The microstructure in polycrystalline materials will be deformed when it is (cold- or hot-) worked. After that, under suitable annealing temperature and time (annealing conditions, for short), a novel microstructure will be established. This process is called recrystallization which occurs after the original grains are deformed by the rolls till new grains grow to impinge on each other as shown in Figure 2.1 (from [Ver75]). Thereby the deformed structure is replaced by a new strain-free polycrystalline structure. At this stage, the material has a new grain size which is the minimum size that can be attained for the particular material composition, amount and form of prior deformation and annealing conditions. A continuation of annealing leads to further migration of the grain boundaries through the recrystallized structure and hence produces a structure containing a smaller number of enlarged grains. This is now called the grain growth process. The basic phenomenon involved in these two processes is the migration of grain boundaries through the structure. The driving force in recrystallization is provided by the removal of the stored energy associated with the deformed state. After recrystallization, the structure is considered as strain-free. Then, in grain growth, the driving force is supplied by the reduction of total grain boundary area in the strain-free structure.

The process of grain growth has two basic forms, namely normal and abnormal. The former is characterized by the maintenance of an approximately uniform grain structure in which the distribution of normalized grain size and shape remains approximately constant throughout the specimen while the average grain size increases. This is sometimes referred to as "continuous grain growth". Alternatively, in the abnormal grain growth process some large grains grow much more rapidly than others. Hence, the distribution of normalized grain size and shape is time-dependent. Correspondingly, it is referred to as "discontinuous

grain growth" [Cot76]. Our discussion will be confined to normal grain growth.

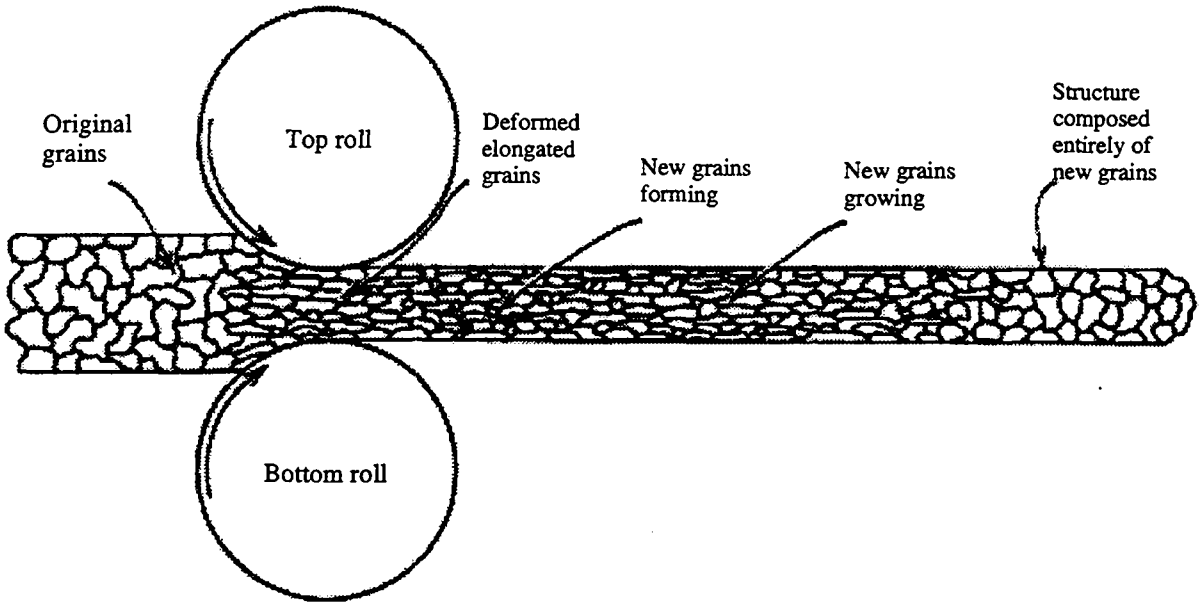

Figure 2.1: Recrystallization and grain growth during hot rolling (from [Ver75]).

2.1.1 Experimental observations

A large number of experimental observations concerning the basic changes of size and shape of grains during normal grain growth are summarized in the following list [Bur52]:

(i) Normal grain growth occurs not by the merger of the neighboring grains but by the migration of the boundaries which surround the expanding grains.

(ii) The rate of migration of any particular boundary is not constant in a series of successive annealing periods and the direction of migration may change from time to time. In other words, the velocity of migration of grain boundary is discontinuous with respect to annealing time.

(iii) A given grain may grow into a neighboring grain on one side and simultaneously be consumed by a different neighbor on another side.

(iv) The rate of consumption of a grain frequently becomes more rapid just before the grain is about to disappear.

(v) A curved grain boundary usually migrates towards its curvature center.

(vi) When grain boundaries in a single-phase material meet at angles different from 120°, the grains included by the more acute angle will be consumed, with the result that all angles tend towards 120° as grain growth proceeds in isotropic assumption.

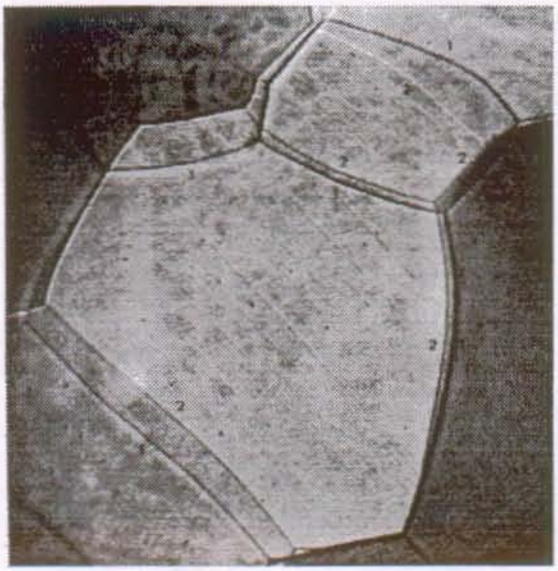

Figure 2.2: Grain boundaries migration in aluminum (from [Ver75]).

Figure 2.2 (from [Ver75]) shows the migration of grain boundaries occurring in aluminum during annealing. The positions of boundaries at time t_1 and t_2, $t_2 > t_1$, are indicated by "1" and "2", respectively.

Beck [Bec54] experimentally showed that during normal grain growth under isothermal annealing conditions, the average grain size can be related to the annealing time by a simple equation, thus:

$$D = Kt^{\eta} \tag{2.1}$$

where D is the average grain diameter in a specimen and t the annealing time. Parameters K and η are constants which depend on the material composition and the annealing conditions, but not on the grain size. Taking into account the initial grain size, Equation 2.1 is replaced by

$$D^{1/\eta} - D_0^{1/\eta} = ct \tag{2.2}$$

where D_0 is the initial average grain diameter and c a constant. Equation 2.2 is often referred to as *the grain growth power law*. Further experiments established that at any given annealing temperature, the isothermal normal grain growth rate only depends on the instantaneous grain size. By differentiating Equation 2.2, the rate is given by

$$\frac{dD}{dt} = \eta c D^{1-1/\eta} \tag{2.3}$$

where t, η and c have the same meaning as in Equations 2.1 and 2.2 and dD/dt represents the instantaneous growth rate. The values of η for polycrystalline materials quoted in [Cot76] range from 0.05 to 0.5. Fullman [Ful52] concluded that η tends to increase towards 0.5 as the annealing temperature increases and the impurity content decreases.

The ideal thermodynamic stability associated with the lowest internal energy of the structure is only attained if all the grain boundaries are eliminated, i.e., if the speci-

men becomes a monocrystal. However, normal grain growth usually stops long before a polycrystalline specimen has been converted into a monocrystal. Therefore, in practice a maximum attainable grain size exists depending on the material composition and annealing conditions.

2.1.2 Theoretical explanations

The first theoretical model for normal grain growth was proposed by Burke and Turnbull in 1952 [Bur52] as mentioned in Chapter 1. They supposed that the whole grain boundary energy is given by

$$E = \int \gamma ds \tag{2.4}$$

where γ is the specific grain boundary energy and the integral is over the grain boundary system. The surface curvature pressure exerted on an isolated portion of grain boundary tends to push it towards the curvature center thus reduces its area and hence the energy associated with it. In a pure single phase system, the migration velocity of an isolated section of grain boundary can be written as

$$v = MP \tag{2.5}$$

where M is the specific grain boundary mobility and P the curvature pressure. Equations 2.4 and 2.5 serve as a principal hypothesis in many models.

Based on Burke and Turnbull's work [Bur52], a statistical theory on normal grain growth, so-called mean field theory, was developed by Feltham [Fel57], Hillert [Hil65] and Mulheran [Mul92]. In their model, the investigated object is an isolated grain embedded in an environment which represents the average effect of the whole array of grains. The theory states that normal grain growth is such a process in which the grain size distribution $f(R)$ changes with time. Hillert analyzed the grain growth rate under the following assumptions:

(i) The size of any particular grain can be described by the radius of an equivalent sphere having the same volume.

(ii) The grain boundary migration rate is proportional to the "pressure difference" caused by its curvature and hence proportional to the reciprocal of its radius of curvature.

(iii) The rate of grain growth is proportional to that of grain boundary migration.

(iv) A critical grain size is demanded for grain growth to occur, such that grains larger than this size will grow and those smaller than it will be consumed.

then the grain growth rate is given by

$$\frac{dR}{dt} = k_H M \gamma \left(\frac{1}{R_H^c} - \frac{1}{R}\right) \tag{2.6}$$

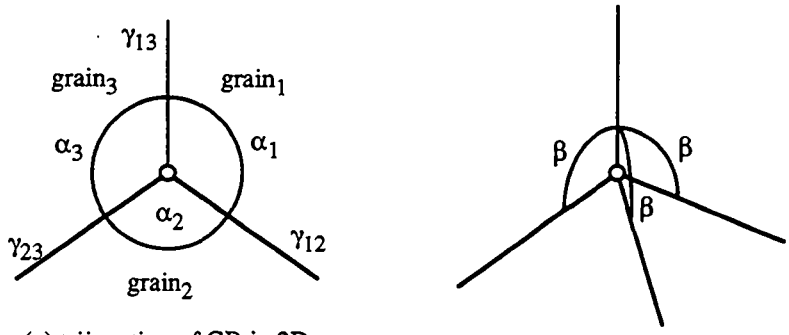

(a) trijunction of GB in 2D (b) a grain corner in 3D

Figure 2.3: Equilibrium conditions at grain edge and corner.

where k_H is a constant and its value is about 1 for 3D analysis and R_H^c the critical grain radius. According to the following relationship, R_H^c increases with time:

$$\frac{d}{dt}((R_H^c)^2) = 0.5 k_H M \gamma \tag{2.7}$$

In two dimensions, the equilibrium between grain boundary tensions at a triple junction point requires that grain boundaries meet at angles specified by the following equation [Smi48]:

$$\frac{\gamma_{12}}{sin\ \alpha_3} = \frac{\gamma_{23}}{sin\ \alpha_1} = \frac{\gamma_{13}}{sin\ \alpha_2} \tag{2.8}$$

where γ_{ij} is the specific interfacial energy of grain boundary meeting at a triple point and α_i is the appropriate dihedral angle as shown in Figure 2.3(a). In three dimensions, three grains meet on a grain edge and the equilibrium condition along the edge is the same as Equation 2.8, while at a grain corner, four grains meet each other. It has been shown [Smi48] that the equilibrium condition on the corner is that the angles between grain edges should be $\beta = 109.5°$ in pure isotropic single phase systems, as shown in Figure 2.3(b). As the relationship between the specific grain boundary energy and the shape of grains in polycrystalline materials is a compromise between the surface tension equilibrium and the requirements of space-filling, it is natural to derive such an idealized shape of grains in the materials: Under equilibrium conditions, grain shapes will be such as to give the minimum total interfacial energy which is compatible with each grain fitting perfectly between its neighbors.

On the topological characteristics of normal grain growth, Aboav [Abo70] found that in 2D cellular systems, a correlation exists between the number of sides of a cell and the average number of sides of its neighbors and is given by:

$$m_n = 5 + \frac{8}{n},\ n = 3, 4, ... \tag{2.9}$$

where n is the number of sides of a given cell and m_n is the average side number of its neighbors. Weaire [Wea74] explained Aboav's correlation by Euler's theorem and

suggested a more general equation:

$$m_n = 5 + \frac{6 + \mu_2}{n},\ n = 3, 4, ... \tag{2.10}$$

with

$$\mu_2 = \sum_{n=3}^{\infty} (n-6)^2 f_n \tag{2.11}$$

where f_n is the probability of n-sided cells in the system.

Lewis [Riv83] proposed that for 2D cellular system the average area of an n-sided cell, A_n linearly depends on n:

$$A_n = A\lambda_A(t)[n - (6 - \frac{1}{\lambda_A(t)})],\ n = 3, 4, ... \tag{2.12}$$

where A is the average area of cells in the system and $\lambda_A(t)$ a linear function of t which represents the aging of the system. Supposing $\lambda_A(t) = ct$, where c is a constant and differentiating Equation 2.12 with respect to t, the average area growth rate of n-sided cells in the system is then given by [Riv83]

$$\frac{dA_n}{dt} = C_R(n-6),\ n = 3, 4, ... \tag{2.13}$$

where C_R a constant which is proportional to the interfacial tension. The concept that the growth rate of a cell in 2D is proportional to its number of sides minus 6 was first proposed by Von Neumann in 1952 [Von52], hence, Equation 2.13 is often referred to as the Von Neumann law.

The Aboav-Weaire law, namely Equation 2.10 has been generalized to 3D [Edw94]. The average number of facets of neighboring cells of a f-faceted cell is given by

$$M_f = F - 1 + \frac{F + \mu_F}{f},\ f = 4, 5, ... \tag{2.14}$$

where F is the average number of facets of cells in the system and μ_F the variance of F. The Lewis law, i.e., Equation 2.12 has been generalized to 3D as well [Riv83]. The average volume of f-faced cells is given by

$$V_f = V\lambda_R(t)(f - F + \frac{1}{\lambda_R(t)}),\ f = 4, 5, ... \tag{2.15}$$

where V is the average volume of cells in the system and $\lambda_R(t)$ a function similar to $\lambda_A(t)$ in Equation 2.12.

By differentiating Equation 2.15 with respect to t, one obtains the three dimensional version of the Von Neumann law as follows:

$$\frac{dV_f}{dt} = C_X(f - F),\ f = 4, 5, ... \tag{2.16}$$

where C_X is a constant similar to C_R in Equation 2.13.

2.2 Three-dimensional simulation models

Two-dimensional computer simulation models have been reviewed by Atkinson [Atk88]. This section will focus on three-dimensional ones. Available models can be classified into three categories: statistical model, pseudo-atomic Potts model and vertex model.

2.2.1 Statistical models

Statistical models were first proposed for 2D normal grain growth simulation. As in such models, there is no geometrical structure of grain system, they can easily be generalized to 3D. The model deals with ensemble probabilities for a collection of grains and it solves a series of interrelated equations so as to find the behavior of typical grain types, in terms of topology class or size class. Actually, these models are the compartment models [Whi86].

Kurtz and Carpay [Kur80] constructed a detailed statistical theory of grain growth. They combined and extended the statistical and topological approaches of Smith [Smi48], Feltham [Fel57] and Rhines and Craig [Rhi74] in a way which overcomes the limitations of either approach taken separately. More precisely, they divided the grains into topological classes, in which grain size is supposed to be log-normally distributed. Therefore each class is specified by its number of facets and the median of grain diameter. The growth rate of classes is given by

$$\frac{dD_f}{dt} = \frac{f}{F}\frac{dD}{dt},\ f = 4, 5, ... \tag{2.17}$$

where F and D are the average number of facets and diameter of cells, respectively, in the system. $D(t)$ is supposed to obey the grain growth power law (Equation 2.2). Evidently, in Equation 2.17, the growth rate of topological classes linearly increases with the value of f. The transfer rate between classes has been solved under a number of simplifying assumptions. When a grain transfers between its neighboring classes it either loses or gains one facet. Growth is controlled by the rate of loss of grains from the lowest topological class (i.e., tetrahedra). Figure 2.4 is a schematic presentation of the model. In a fixed time interval, the transfer of larger grains to the next lower class results in a continuous growth in the mean diameter in the classes with $f < F$.

Concerning the size classes, Abbruzzese, Lücke and their co-workers [Abb86] established another compartment model from Hillert's mean field theory [Hil65]. In the model, the grains are divided into N_s size classes. Each class is indicated by the range of radius ΔR_i and its mean radius R_i. The critical radius of the system is given by

$$R_C = R(1 + \chi) \tag{2.18}$$

where χ is the variance of the grain size distribution in the system. The growth rate of class i is given by

$$\frac{dR_i}{dt} = M_i'(\frac{1}{R_C} - \frac{1}{R_i}) \tag{2.19}$$

where M_i' is the specific diffusivity of grain boundaries defined as

$$M_i' = 2M_i\gamma_i \tag{2.20}$$

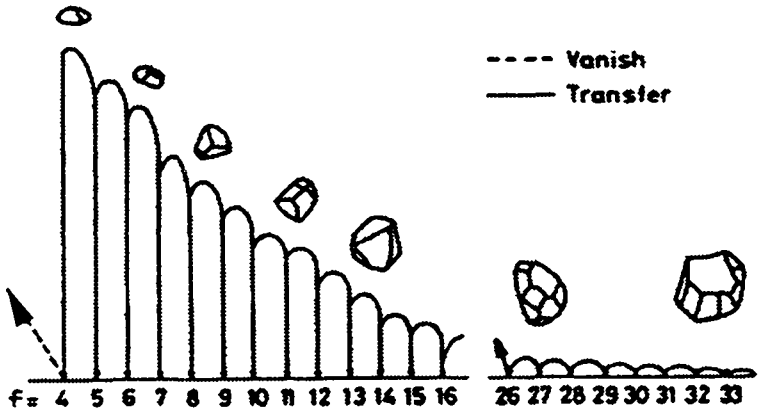

Figure 2.4: Kurtz-Carpay model (from [Kur80]).

In the isotropic case, M_i' has the same value for any $i \in N_s$. In one simulation step, a grain is restricted to at most transfer into its neighboring classes and then the transfer rate between neighboring classes is given by

$$\begin{cases} \dfrac{dn_i}{dt} = -\dfrac{1}{\Delta R}\left(n_i\dfrac{dR_i}{dt} - n_{i-1}\dfrac{dR_{i-1}}{dt}\right) : R_i > R_C \\ \dfrac{dn_i}{dt} = -\dfrac{1}{\Delta R}\left(n_i\dfrac{dR_i}{dt} - n_{i+1}\dfrac{dR_{i+1}}{dt}\right) : R_i < R_C \end{cases} \tag{2.21}$$

where n_i is the number of grains in class i. To be able to account the heterogeneous grain system, they suggested to divide all grains into N_sH classes. Each class is then indicated by individual diffusivity M_{ij}' as well as its radius. Following the same path, the growth and transfer rate can be determined.

The simulation results of statistical models can explain the overall kinetics of the system. However, the microstructure information of the simulated system provided by this kind of models is very limited.

2.2.2 Pseudo-atomic Potts model

In contrast to the statistical models, the pseudo-atomic Potts model deals with the detail of grain and grain boundary. In this model, the microstructure is mapped onto a discrete lattice which can be cubic, tetrahedral or whatever symmetry is chosen. In the initial state, each lattice site is assigned a number between 1 to q to represent the orientation of the matter at this lattice site. A grain boundary is defined to lie between sites of unlike orientation and the grain boundary energy is also specified. The boundary migration is simulated by the Monte-Carlo technique. A lattice site is selected at random and a new trial orientation is also chosen at random from one of the other $(q-1)$ possible

orientations. The transition probability is simulated as

$$W = \begin{cases} exp(-\frac{\Delta G}{k_B \mathrm{T}}), & \Delta G > 0 \\ 1, & \Delta G \leq 0 \end{cases} \tag{2.22}$$

where ΔG is the incremental energy caused by the change in orientation, k_B the Boltzmann constant and T the absolute temperature. Successful transition at the grain boundary to the orientation of nearest neighbor grain corresponds to a boundary migration. The migration velocity of a boundary segment, ν_i is then related to the local chemical potential difference ΔG_i and is given by

$$\nu_i = M[1 - exp(\frac{\Delta G_i}{k_B \mathrm{T}})] \tag{2.23}$$

Figure 2.5 shows a 2D microstructure which has been amply annealed, i.e., after sufficiently long simulation time. The simulation process can be manipulated by defining an appropriate neighborhood for a lattice site so that the process only weakly depends on the symmetry of the chosen lattice. Examples of 3D pseudo-atomic Potts simulation have been reported by Anderson and Grest [And89] and Righetti, Liebling and Mocellin [Rig89].

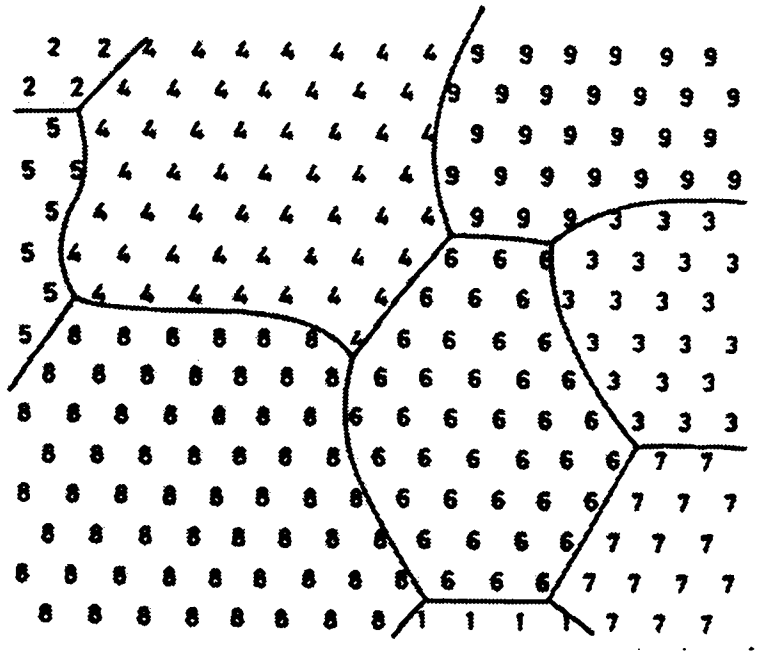

Figure 2.5: 2D pseudo-atomic Potts model (from [And84]).

As the model requires a dense lattice to emulate grain and its boundary migration, it is rather difficult to simulate an aggregate of grains which is large enough to provide reliable statistic of the process in current hardware circumstance. Another limitation of the model is that the simulation time of this model has no physical meaning, hence it is difficult to compare to the experimental data.

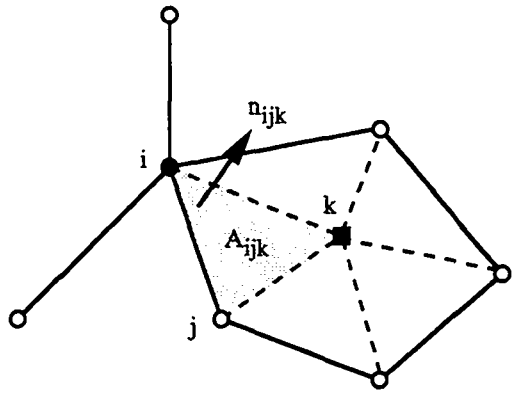

Figure 2.6: Triangulation of a facet by inserting a virtual vertex (from [Fuc95]).

2.2.3 Vertex model

The 2D vertex model was first proposed by Fullman in 1952 [Ful52], then modified by Soares, Ferro and Fortes [Soa85] and Kawasaki, Nagai and Nakashima [Kaw89]. Recently, Marsh, Masumura and Pande [Mar93] have adopted grain boundary curvature into this model. To our knowledge, to date, only Kawasaki-Nagai group [Kaw93, Fuc95] have generalized their 2D model to 3D. Based on Fuchizaki, Kusaba and Kawasaki's newest results [Fuc95], the 3D vertex model is summarized as follows.

It is assumed that a 3D boundary network has straight edges and planar interfaces at all instants. Moreover, each facet with more than three edges is triangulated by inserting a virtual vertex as shown in Figure 2.6. The virtual vertex is treated the same way as other vertices. The driving force for growth results from the interfacial tension acting on vertex. To minimize the interfacial tension, the driving force pushes the vertex towards its equilibrium position. Suppose the system is purely dissipative, then at each vertex, the driving force is balanced by a frictional force which is proportional to the velocity of the vertex. Therefore, the velocity of vertices is given by

$$\sum_{j,k}^{(i)} D_{ijk}(v_i + \frac{1}{2}v_j + \frac{1}{2}v_k) = \frac{1}{2}\sum_{j,k}^{(i)} n_{ijk} \times (r_j - r_k) \tag{2.24}$$

where r_j and v_j are the position and velocity of vertex j, respectively. D_{ijk} is a 3×3 matrix,

$$D_{ijk} = \frac{1}{6L} A_{ijk} n_{ijk} n_{ijk}^t \tag{2.25}$$

where n_{ijk} is the unit normal vector of triangle (ijk) and its orientation is determined by the right-hand screw rule, $\sum_{j,k}^{(i)}$ is over the triangles which are incident to vertex i, A_{ijk} is the area of triangle (ijk) and L the kinetic coefficient. The velocity of each vertex of the system can be obtained from simultaneous equations whose variable number is equal to that of original vertices plus that of virtual ones[1]. In the initial state, the virtual vertex

[1]Kawasaki, Nagai and their co-workers directly solved the differential equations by the Runge-Kutta method [Kaw93, Fuc95].

is supposed to coincide with the gravity center of the facet. After that, its position is self-consistently determined, i.e., it is not necessarily coplanar with other vertices of the facet[2].

Three types of topological transformations are allowed in the model. Given a critical length Δ_K, an edge whose length is less than or equal to Δ_K may be deleted or may create a new triangle depending on its incident triangles. If it is an edge of a tetrahedron, then the tetrahedron could be shrunk into a vertex. Computer simulation started from a 3D Voronoi diagram with initially 1,000 cells and stopped when only 100 cells remained.

As the system for $t > 0$ is no longer a convex cell complex, it is unsure whether the defined topological transformations can deal with all the topological events occuring in the system or not. Now that the topological events are only treated at the end of each simulation step, the corresponding topological transformation (if it exists) could not be done at the exact instant when the event arises. Therefore, the difference of kinetics due to the approximation merits further investigation.

To precisely detect and treat topological transformations, it is suggested to idealize the grain system as a Laguerre diagram. Because any convex and simple cell complex in 3D is indeed a Laguerre diagram which can be dynamically maintained over time. The development of the diagram and its application in the materials science will be reviewed in next section.

2.3 The making of the Laguerre diagram

In this section, the development of the Laguerre diagram is traced back to 1644. The application of the diagram in materials science and the development of the diagram oriented to grain growth simulation are reviewed.

2.3.1 Definition of Laguerre diagram

The Laguerre diagram (or the power diagram [Aur87]) is a generalized Voronoi diagram. The Laguerre-like diagrams first appeared in Descartes' work, "Principia Philosophiae" published in 1644. One of the diagrams was used to present the disposition of matter in the solar system and its environs (see Figure 2.7). In this figure, S is the sun, ε a star, RQD the path of a comet and polygonal areas the heavens [Des83, Oka92]. The author did not put any commentary on the diagram's construction in his text. More than two hundred years later, Dirichlet (1850) and Voronoi (1907) [Vor07] proposed a diagram in $\mathbb{R}^d$ which can be described as follows. Given a set S of N sites, where each site $a = (a_1, a_2, ..., a_d) \in \mathbb{R}^d$ gives the site coordinates, the distance between an arbitrary point $x \in \mathbb{R}^d$ and $a \in S$ is defined as

$$d(x, a) = [\sum_{i=1}^{d}(a_i - x_i)^2]^{1/2} \tag{2.26}$$

[2]Thereby, at any time $t > 0$, the cellular system is no longer a convex cell complex.

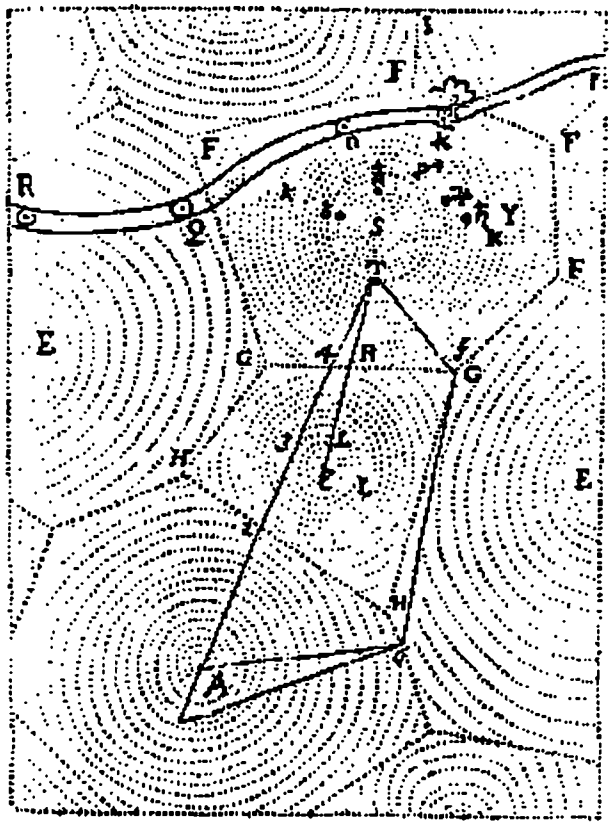

Figure 2.7: The disposition of matter in the solar system and its environs (from [Des83]).

the region

$$V(a) = \{x \in \mathbb{R}^d : d(x,a) \leq d(x,b), for\ a \neq b\ and \forall\ a,b \in S\} \tag{2.27}$$

is called the Voronoi cell associated with site a and then the set

$$V(S) = \{V(a) : \forall\ a \in S\} \tag{2.28}$$

the Voronoi diagram generated by the site set S. Dirichlet developed the diagram in two and three dimensions, whereas Voronoi treated it in high dimensions. As a result of the early work, the diagram is called Dirichlet tessellation or Voronoi diagram.

The dual diagram of Voronoi diagram was proposed by Delaunay (or Delone) in an article in memory of Voronoi in 1934 [Del34]. From then on, the dual of Voronoi diagram has been called the Delaunay diagram. Since every d-dimensional cell in a d-dimensional Delaunay diagram is a d-simplex (e.g., it is a triangle in 2D and a tetrahedron in 3D) and since given a Delaunay diagram of N sites, its dual, the Voronoi diagram can be constructed in $O(N)$ time, Delaunay diagram is often used to represent both diagrams.

Lee and Drysdale [Lee81] studied the Voronoi diagram in different metrics (from L_1 to L_∞). Imai, Iri and Murota [Ima85] stated that the Laguerre distance is a possible alternative of the Euclidean distance with special applications. In 1987, Aurenhammer

presented properties, algorithms and some possible applications of the diagram [Aur87]. In his terminology, the Laguerre diagram in $\mathbb{R}^d$ can be defined as follows. Given a weighted site set S' of N sites, where each site $a' = (a, a_{d+1})$ and $a \in \mathbb{R}^d$ and $a_{d+1} \in \mathbb{R}^+$ is the weight of the site, the power of an arbitrary point $x \in \mathbb{R}^d$ with respect to weighted site $a' \in S'$ is defined as

$$p(x, a') = d^2(x, a) - a_{d+1} \tag{2.29}$$

where $d(x, a)$ is defined as Equation 2.26. Given a weighted site set S' as above, the region

$$L(a') = \{x \in \mathbb{R}^d : p(x, a') \leq p(x, b'), \text{ for } a' \neq b' \text{ and } \forall\, a', b' \in S'\} \tag{2.30}$$

is called the Laguerre cell associated with a' and then the set

$$L(S') = \{L(a') : \forall a' \in S'\} \tag{2.31}$$

the Laguerre diagram generated by weighted site set S'. Let S' be the set of $N \geq 3$ weighted sites in $\mathbb{R}^2$, then $L(S')$ consists of at most N cells, $3N - 6$ edges and $2N - 5$ vertices. In $\mathbb{R}^3$, $L(S')$ consists of at most N cells, $O(N^2)$ facets, edges and vertices. All the components are flat, i.e., each edge is a straight line segment; each facet is a planar region bounded by edges and vertices; each cell is a convex polyhedron bounded by facets, edges and vertices. Such a tessellation is said to be a simple convex cell complex. Actually, it has been shown [Dav59, Aur87, Lie92]:

Theorem 2.1 *In $\mathbb{R}^d$ any simple convex cell complex is a Laguerre diagram, provided $d \geq 3$.*

To construct the Laguerre diagram of weighted site set S' in $\mathbb{R}^d$, Aurenhammer proposed an algorithm with

$$\text{time complexity} = \begin{cases} O(N \log N), \text{ for } d = 2 \\ O(N \log N + N^{\lceil (d+1)/2 \rceil}), \text{ for } d > 2 \end{cases}$$

As it is based on the construction of convex hull[3] of S', this algorithm is time-optimal for $d = 2$ and every odd d [Aur87].

A problem of recent interest has been that of allowing the site set S or S' to vary continuously over time. As the sites move, the diagram changes continuously, but at certain instants, topological events occur that cause a change in the topological structure of the diagram. The dynamic Laguerre diagram in $\mathbb{T}^2$ has been studied by Telley [Tel89a] who proposed a procedure to maintain the diagram over time. In 1992, Telley has proved that the number of topological events was bounded, thereby the procedure was indeed an algorithm, in case site position is fixed and site weight is linearly changed [Tel92b]. Righetti has generalized the algorithm to $\mathbb{T}^3$. Roos [Roo91] has studied the dynamic Voronoi diagram in $\mathbb{R}^2$ and independently proposed the same algorithm. Albers and Roos

[3]Sugihara recently proposed a robust algorithm for construction of 3D convex hull by facet-flips [Sug94].

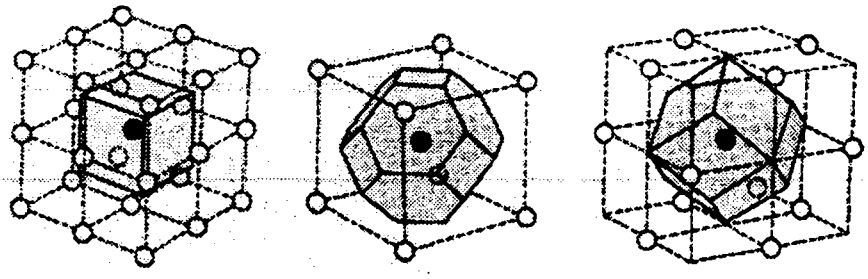

Figure 2.8: Some 3D lattices and their associated Laguerre cells (from [Ver75]).

pursued their research in high dimensional Euclidean space [Alb92]. Very recently, Albers, Mitchell, Guibas and Roos [Alb95] have proved the algorithm can maintain a dynamic Voronoi diagram in d-dimensional Euclidean space, $d \geq 2$ and provided a linear-factor improvement over the $O(N^{d+2})$ upper bound on the number of topological events.

2.3.2 Applications of Laguerre diagram in materials science

The Laguerre diagram is not a novelty of mathematicians, it has been used to approximate the materials' microstructure since the 1920s. In Figures 2.8, the Laguerre-like diagrams are used to represent the crystalline structure of metal, in which, each site is given before the construction of diagram and each site remains fixed throughout the construction. Considering in the system, a set of sites are occupied by atoms which are represented as equal-sized spheres and the sites are regularly arranged in $\mathbb{R}^3$, forming a spatial lattice. This structure is called crystal and each Laguerre-like region represents a domain of action[4]. In Figure 2.8, from left to right, they are simple cubic, body centered cubic and face centered cubic lattice. The corresponding Laguerre cell are cube, truncated octahedron (14 facets) and rhombic dodecahedron (12 facets).

From the 1930s, the diagram has been used to simulate the recrystallization in metallurgical systems [Avr39, Joh39]. In such systems, the site is inserted in the diagram one by one at a different time and once a site is inserted, its position remains fixed throughout the evolution process. Each cell's radius increases at the same rate. The evolution ceases whenever the sphere growing from its center comes into contact with the sphere growing from its neighbors. Figure 2.9 shows a series of stages in the evolution process in 2D.

Another application of the diagram is to verify the property of space-filling. It has been shown a polyhedron may possess as many as several hundred facets. However, in polycrystalline materials, only a number of polyhedra with 38 facets have been identified so far [Abo92].

To our knowledge, simulating the grain growth process with a dynamic Laguerre-like

[4]In this case, as equal-sized spheres are considered, the diagram is a Voronoi diagram instead of a Laguerre one.

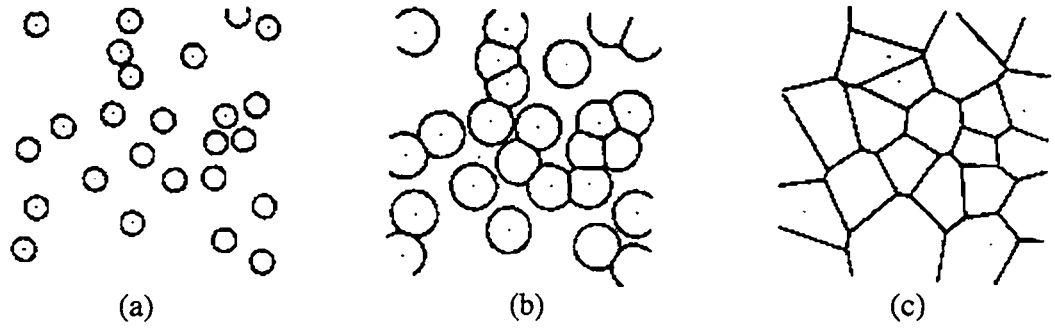

Figure 2.9: Different stages of recrystallization (from [Avr39]).

diagram[5] was first proposed by Fullman in 1952 [Ful52]. In the diagram, the initial site set is given and once an initial diagram is constructed, the position of vertices may be changed in different rate and direction. This method had been further developed by Fortes and Ferro [For85], Kawasaki, Nagai and Nakashima [Kaw89], and Telley, Mocellin and Liebling [Tel89b]. Because at that time the dynamic maintenance problem of the diagram had not been solved, in all these models the topological events were approximately treated.

To precisely simulate the normal grain growth occurring in polycrystalline materials, especially to precisely detect and treat the topological events, in 1989 Telley established the Laguerre diagram in another space, the two-dimensional unit flat torus, noted as $\mathbb{T}^2$, and proposed an edge-flip algorithm, to construct the diagram with the time-complexity of $O((m+N)\log N)$ under certain conditions, where m is the number of topological events induced by the motion of weighted site set. Moreover, he has proved that the diagram in $\mathbb{R}^2$ can be dynamically maintained, as long as the position and weight of a site are linear functions of time [Tel90]. Righetti has developed the corresponding programs to simulate recrystallization in $\mathbb{T}^3$. The result is a Laguerre diagram generated by a set S' of N weighted site in $\mathbb{T}^3$ [Rig92]. In this study, the dynamic Laguerre diagram in $\mathbb{T}^3$ will be established in order to simulate normal grain growth in three dimensions.

2.4 Summary

From the experimental observation and theoretical analysis of normal grain growth, the following basic conclusions can be drawn:

(i) the kinetic behavior of grain growth can be approximated by a parabolic function (Equation 2.2) which is often referred to the (grain growth) power law;

(ii) the driving force in the process is from minimizing the total grain boundary energy;

(iii) the surface tension equilibrium conditions at grain edge and corner are statistically obeyed in the process.

[5] A Laguerre-like diagram is a network with rectilinear edges.

These will serve as the principal hypotheses in our further study.

As the statistical models could not provide enough information about the microstructure of the simulated material and the pseudo-atomic Potts model could not simulate large scale system with today's hardware, the simulation at the level of grain and grain boundary is a reasonable compromise between the goals to detail the microstructure and to understand growth kinetic behavior.

One of shortcomings of the vertex model is that the topological events could not be detected and treated exactly, while 2D simulation has shown that the Laguerre model [Tel89a] can perfectly overcome this shortcoming. This is why this study dedicates to the generalization of the model.

To model normal grain growth as a dynamic Laguerre diagram in the 3D unit flat torus, one should first solve the dynamic maintenance problem of the diagram. This will be the main task of the next chapter.

Chapter 3

Dynamic Delaunay Diagram in 3D Unit Flat Torus

As mentioned in Chapter 2, the dual of Laguerre diagram is the weighted Delaunay diagram (or the weighted Delaunay triangulation) which is composed of tetrahedra in three dimensions and given a weighted Delaunay diagram, its corresponding Laguerre diagram can be constructed in $O(N^2)$ time [Rig92]. Triangulations and particularly Delaunay triangulations have received much attention in the field of computational geometry [Ede87]. Their construction and properties in Euclidean space $\mathbb{R}^d$ have been well documented for $d = 2$, but not yet when $d > 2$.

Recently, Joe [Joe89, Joe91, Joe93] has provided an incremental algorithm to construct a Delaunay diagram in $\mathbb{R}^3$. Albers, Mitchell, Guibas and Roos have proved very recently that in $\mathbb{R}^d$, $d \geq 2$, the dynamic Voronoi diagram can be maintained in finite time [Alb95].

The main topics of this chapter are the construction and maintenance of dynamic weighed Delaunay diagram in the three-dimensional unit flat torus $\mathbb{T}^3$. The convergence of the maintenance algorithm is firstly studied. As applications of the algorithm, the construction of unweighted and weighted Delaunay diagrams, as well as the maintenance of the diagram in linearly normal motion are presented.

3.1 Delaunay diagram

In this section, the three-dimensional unit flat torus, the triangulations and the Delaunay diagram in the space are defined sequentially.

3.1.1 Three-dimensional unit flat torus

To model the long-term regime behavior of physical or biological systems resulting from local interactions between their innermost entities (e.g., atoms in physical system, grains in material systems and cells in biological systems), one may be interested in the interplay of the entities but not in the entities on the system borders. Therefore, it is convenient

to characterize the system in some periodic space, e.g., in a unit flat torus [Tel90, Oka92]. Three-dimensional unit flat torus is such a space obtained by periodically repeating a unit cube in $\mathbb{R}^3$.

Two points a and b in $\mathbb{R}^3$ are said to be equivalent and noted as $a \sim b$, if $b - a \in \mathbb{Z}^3$, where $\mathbb{Z}^3$ denotes the set of integer numbers. In fact, any point $a \in \mathbb{R}^3$ generates the *equivalence class* $\bar{a}$ *of all points of* $\mathbb{R}^3$ *equivalent to* a. A point of $\mathbb{R}^3$ which generates a given point $\bar{a}$ of the torus is called a representative of $\bar{a}$ in $\mathbb{R}^3$. The representatives of $\bar{a}$ are of the form $a + z$, $z \in \mathbb{Z}^3$.

Generally, two subsets A, B in $\mathbb{R}^3$ are said to be equivalent and noted as $A \sim B$ if $B = A + z$ for $z \in \mathbb{Z}^3$. Any subset $A \in \mathbb{R}^3$ generates the equivalence class $\bar{A}$ of all subsets of $\mathbb{R}^3$ equivalent to A. A subset of $\mathbb{R}^3$ which generates a given subset $\bar{A}$ of the torus is called a representative of $\bar{A}$ in $\mathbb{R}^3$. The representatives of $\bar{A}$ are of the form $A + z$, $z \in \mathbb{Z}^3$.

Finally, every point a of the torus is in fact the equivalence class of an infinite collection of the objects of $\mathbb{R}^3$. There is exactly one representative of a in every unit cube. In other words, such a cube contains exactly one period of the torus. Among these cubes, the canonical cube $[0,1[^3$ is distinguished. The representative of a in $[0,1[^3$ is called the canonical representative of a.

Three-dimensional unit flat torus $\mathbb{T}^3$ is then defined as the quotient of $\mathbb{R}^3$ by the equivalence relation $\sim$, namely,

$$\mathbb{T}^3 = \mathbb{R}^3 / \sim \tag{3.1}$$

The space is visualized in Figure 3.1. The unit cube in Figure 3.1(a) is the canonical form of $\mathbb{T}^3$ and *face* A *coincides with face* B, C *with* D *and* E *with* F. "Developing" this cube, one gets Figure 3.1(b) which is composed of 27 unit cubes. In the space the distance between two points $a = (a_1, a_2, a_3)$ and $b = (b_1, b_2, b_3)$ is measured by

$$d_{\mathbb{T}}(a,b) = \min_{\alpha,\beta,\rho \in \mathbb{Z}} \{\sqrt{(a_1 - b_1 + \alpha)^2 + (a_2 - b_2 + \beta)^2 + (a_3 - b_3 + \rho)^2}\} \tag{3.2}$$

Notice that the distance is bounded in $0 \leq d_{\mathbb{T}}(a,b) \leq \sqrt{3}/2$. From now on, the distance in $\mathbb{T}^3$ is measured by the unit flat torus distance. The convexity of a subset A of the torus can be globally and locally stated as follows:

(i) The only convex subset of the torus is the torus itself.

(ii) A subset A of $\mathbb{T}^3$ is said to be locally convex if its representatives in $\mathbb{R}^3$ are convex.

The local convexity of a subset is the base to derive the local properties of triangulations.

3.1.2 Triangulations

Given two subsets A and B in $\mathbb{T}^3$, their pseudo-intersection is defined as the relative interior of the intersection of their closures and noted as $A \cap' B$.

Definition 3.1 *A triangulation* $\mathcal{T}$ *of* $\mathbb{T}^3$ *is a collection of simplexes in* $\mathbb{T}^3$ *(including the empty set) with*

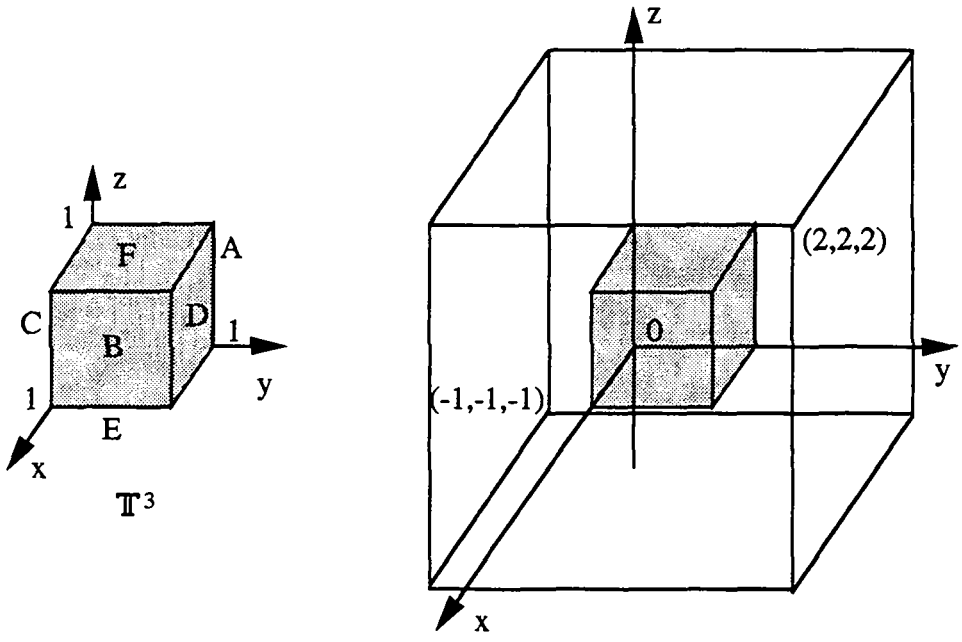

Figure 3.1: Three-dimensional unit flat torus.

(i) $\mathcal{T}$ *is a partition of* $\mathbb{T}^3$, *i.e.,* $\bigcup_{\bar{T}\in\mathcal{T}} = \mathbb{T}^3$ *and* $T_1 \bigcap T_2 = \emptyset$ *for any representative* T_1 *of* $\bar{T}_1 \in \mathcal{T}$ *and* T_2 *of* $\bar{T}_2 \in \mathcal{T}$, $T_1 \neq T_2$;

(ii) $\overline{T_1 \bigcap' T_2} \in \mathcal{T}$, *for any representative* T_1 *of* $\bar{T}_1 \in \mathcal{T}$ *and* T_2 *of* $\bar{T}_2 \in \mathcal{T}$.

Depending on their dimension (0, 1, 2 or 3), the elements of $\mathcal{T}$ are called vertices, edges, facets and cells, respectively. Given a set $\bar{S}$ of sites in $\mathbb{T}^3$, a triangulation whose set of vertices is exactly set $\bar{S}$ is called a triangulation of $\mathbb{T}^3$ with respect to $\bar{S}$.

Suppose $\mathcal{T}$ is a triangulation as in Definition 3.1, then each element of $\mathcal{T}$ is a simplex, i.e., a 0-dimensional simplex is a vertex, a 1-dimensional one is a line segment (edge), a 2-dimensional one is a triangle (facet) and a 3-dimensional one is a tetrahedron (cell). The number of simplexes of $\mathcal{T}$ in $\mathbb{T}^3$ is different from that in $\mathbb{R}^3$, for there is no external simplex in $\mathbb{T}^3$. It has been proved [Tel90] that the triangulation of given site set in $\mathbb{T}^2$ is identical with that in $]-1,2]^2$ by repeating the site set in these 9 unit squares, as long as triangles in the triangulation are sufficiently small. Actually this is the so-called "cut-and-glue" method which can construct a triangulation of the site set in $\mathbb{T}^2$ [Tel90, Oka92]. This assertion holds in $\mathbb{T}^3$. Therefore, McMullen's upper bound theorem [Mcm70] can still be applied to determine the upper bound of the number of simplexes.

Theorem 3.1 *Let* $\mathcal{T}$ *be a triangulation of a set* $\bar{S}$ *of* N *sites in* $\mathbb{T}^3$, *then in the triangulation there are exactly* N *0-simplexes and* $O(N^2)$ *1-, 2- and 3-simplexes.*

Among all possible triangulations, the Delaunay triangulation is much more interesting for its special local character which will be studied in next subsection.

3.1.3 Definition of Delaunay diagram

Given a set $\bar{S}$ of N sites in $\mathbb{T}^3$ in which each site, say site a is represented by a point $a = (a_1, a_2, a_3)$ in the space, the Delaunay diagram of $\bar{S}$ in $\mathbb{T}^3$ can be defined as follows.

Definition 3.2 *Let $\mathcal{T}$ be a triangulation of site set $\bar{S}$ in $\mathbb{T}^3$ and $\bar{T}$ one of its i-simplexes, $0 \leq i \leq 3$. The open ball $\bar{P}$ is an isolating sphere for $\bar{T}$ with respect to $\bar{S}$ if*

(i) its boundary $\partial\bar{P}$ contains the vertices of $\bar{T}$;

(ii) $\bar{P}$ contains no site of $\bar{S}$: $\bar{P} \bigcap \bar{S} = \emptyset$.

The unique candidate for being the isolating sphere of a 3-simplex (i.e., a tetrahedron) $\overline{abcd}$ of $\mathcal{T}$ in $\mathbb{T}^3$ is its circumsphere $\gamma(\overline{abcd})$. The candidates for being isolating spheres of a 2-simplex (i.e., a triangle) $\overline{abc}$ of $\mathcal{T}$ are called chordal spheres of $\overline{abc}$ as they contain $\bar{a}$, $\bar{b}$ and $\bar{c}$ in their boundary. Their center is on a line which is perpendicular to the triangle. The candidates for being the isolating spheres of a 1-simplex (i.e., an edge) $\overline{ab}$ of $\mathcal{T}$ are called chordal spheres of $\overline{ab}$ as they contain $\bar{a}$ and $\bar{b}$ in their boundary. Their center is on the perpendicular bisector of $\overline{ab}$. A vertex $\bar{a}$ of $\mathcal{T}$ always possesses an isolating sphere, that is, the sphere of center $\bar{a}$ and radius 0.

Definition 3.3 *A triangulation $\mathcal{T}$ of site set $\bar{S}$ in $\mathbb{T}^3$ is called a Delaunay diagram of $\bar{S}$ if every element of $\mathcal{T}$ possesses an isolating sphere.*

This Definition is called the sphere criterion of Delaunay diagram. The criterion can be further localized as follows.

Definition 3.4 *Let $\overline{bcd}$ be a facet of triangulation $\mathcal{T}$ in $\mathbb{T}^3$. Also let $\overline{abcd}$ and $\overline{bcde}$ be the two tetrahedra of $\mathcal{T}$ which share $\overline{bcd}$ in their boundary. Facet $\overline{bcd}$ is said to be legal with respect to $\mathcal{T}$, if $\overline{bcd}$ possesses an isolating sphere with respect to $\{\bar{a}, \bar{b}, \bar{c}, \bar{d}, \bar{e}\}$.*

This Definition is called the local criterion of Delaunay diagram. More precisely, one has:

Theorem 3.2 *A triangulation $\mathcal{T}$ of site set $\bar{S}$ in $\mathbb{T}^3$ is a Delaunay diagram of $\bar{S}$ in $\mathbb{T}^3$ if and only if every 2-simplex of $\mathcal{T}$ is legal with respect to $\mathcal{T}$.*

As the heart of the proof is exactly the same as that in $\mathbb{R}^3$ [Joe89, Rig92], it is not given here[1]. The idea is to show that if an i-simplex violates the sphere criterion for being a Delaunay diagram, then there is (at least) a facet violating the local criterion at the same location.

3.2 Weighted Delaunay diagram

After studying the Delaunay diagram in $\mathbb{T}^3$, this section is devoted to its simplest generalization, the weighted Delaunay diagram. Now that each site is with a weight, it is convenient to investigate the diagram in four-dimensional space. In this section, the properties of the diagram are probed after introducing that space.

[1] A proof in more general case is given in next section.

3.2.1 Definition of weighted Delaunay diagram

The site set of a weighted Delaunay diagram is noted as $\bar{S}'$. Each site, say, site $\bar{a}' = (\bar{a}, a_4) \in \bar{S}'$, where $\bar{a} = (a_1, a_2, a_3)$ are the coordinates of the site in $\mathbb{T}^3$ and $a_4 \in \mathbb{R}^+$ its weight.

Definition 3.5 *A four-dimensional space $\mathbb{H}$ is defined as $\mathbb{T}^3 \times \mathbb{R}$ in which the first three coordinates (x_1, x_2, x_3) are $\mathbb{Z}$-periodic and the fourth one (x_4) is non periodic. As the development of $\mathbb{T}^3$ is $\mathbb{R}^3$, the development of $\mathbb{H}$ noted as $\mathbb{H}'$ is $\mathbb{R}^4$.*

Definition 3.6 *A lifted representative of weighted site $\bar{a}' \in \bar{S}'$ noted as $\hat{a}$ is defined in $\mathbb{H}'$ such that*

$$\hat{a} = (\bar{a} + z,\ a_4), z \in \mathbb{Z}^3 \tag{3.3}$$

The lifted representatives of weighted site set $\bar{S}'$ in $\mathbb{H}'$ are noted as $\hat{S}$,

$$\hat{S} = \{(\bar{a} + z,\ a_4) : \forall \bar{a}' \in \bar{S}' \text{ and } \forall z \in \mathbb{Z}^3\} \tag{3.4}$$

Definition 3.7 *The power paraboloid containing $\hat{a}$, $\hat{b}$, $\hat{c}$ and $\hat{d}$ is a paraboloid of revolution in $\mathbb{H}'$ and defined as*

$$\psi(\widehat{abcd}) = \{x \in \mathbb{H}' :\ x_4 - x_{40} = (x_1 - x_{10})^2 + (x_2 - x_{20})^2 + (x_3 - x_{30})^2\} \tag{3.5}$$

where $x = (x_1,\ x_2,\ x_3,\ x_4)$ is an arbitrary point in $\mathbb{H}'$ and $(x_{10}, x_{20}, x_{30}, x_{40})$ the apex of the paraboloid which is determined by $\hat{a}$, $\hat{b}$, $\hat{c}$ and $\hat{d}$.

The superior and inferior portion of $\mathbb{H}'$ with respect to power paraboloid $\psi(\widehat{abcd})$ are noted as $\psi_+(\widehat{abcd})$ and $\psi_-(\widehat{abcd})$, respectively.

Definition 3.8 *Given point $x = (x_1,\ x_2,\ x_3,\ x_4) \in \mathbb{H}'$, h is a mapping defined by $h : \mathbb{H}' \to \mathbb{H}'$ such that*

$$h(x) = (x_1,\ x_2,\ x_3,\ x_4 - x_1^2 - x_2^2 - x_3^2) \tag{3.6}$$

The h-mapped point x is noted as $\tilde{x}$, i.e., $\tilde{x} = h(x)$. If the point is a lifted representative of site $\bar{a}' \in \bar{S}'$, then the lifted representative can be h-mapped as

$$\tilde{a} = h(\hat{a}) = (a_1 + z_1,\ a_2 + z_2,\ a_3 + z_3,\ a_4 - (a_1 + z_1)^2 - (a_2 + z_2)^2 - (a_3 + z_3)^2) \tag{3.7}$$

where, $[z_1\ z_2\ z_3]^t = z \in \mathbb{Z}^3$. The h-mapped (lifted) representatives of $\bar{S}'$ are written as

$$\tilde{S} = \{h(\hat{a}) : \forall \bar{a}' \in \bar{S}' \text{ and } \forall z \in \mathbb{Z}^3\} \tag{3.8}$$

In $\mathbb{H}'$ space, the hyperplane containing $\tilde{a}$, $\tilde{b}$, $\tilde{c}$ and $\tilde{d}$ is noted as $\pi(\widetilde{abcd})$. The superior and inferior half-space of $\mathbb{H}'$ with respect to hyperplane $\pi(\widetilde{abcd})$ are noted as $\pi_+(\widetilde{abcd})$ and $\pi_-(\widetilde{abcd})$, respectively.

Lemma 3.1 *Let h and ψ be defined as above, then $h(\psi(\widehat{abcd}))$ is a non-vertical hyperplane with respect to the x_4-axis in $\mathbb{H}'$ space.*

Proof: As h is a one-to-one mapping,

$$h^{-1}(x) = (x_1,\ x_2,\ x_3,\ x_4 + x_1^2 + x_2^2 + x_3^2) \tag{3.9}$$

and

$$h(\psi) = \{x \in \mathbb{H}' :\ h^{-1}(x) \in \psi\} \tag{3.10}$$

Assuming ψ has apex $(x_{10}, x_{20}, x_{30}, x_{40})$, replacing x by $h^{-1}(x)$ in Equation 3.5 and then simplifying the equation, $h(\psi)$ comes to

$$x_4 - x_{40} = -x_{10}(2x_1 - x_{10}) - x_{20}(2x_2 - x_{20}) - x_{30}(2x_3 - x_{30}) \tag{3.11}$$

From analytical geometry, this is a non-vertical hyperplane in $\mathbb{H}'$. □

Lemma 3.2 *Let $\psi(\widehat{abcd})$ and $h(\psi(\widehat{abcd}))$ be as above, then*

$$\begin{cases} h(\psi_+) = [h(\psi)]_+ \\ h(\psi_-) = [h(\psi)]_- \end{cases} \tag{3.12}$$

Proof: For the first equality, suppose power paraboloid $\psi(\widehat{abcd})$ with apex $(x_{10}, x_{20}, x_{30}, x_{40})$ is given, then

$$\psi_+ = \{x \in \mathbb{H} :\ x_4 - x_{40} > (x_1 - x_{10})^2 + (x_2 - x_{20})^2 + (x_3 - x_{30})^2\}$$

From Equations 3.5, 3.9 and 3.10, one has

$$x_4 - x_{40} > -x_{10}(2x_1 - x_{10}) - x_{20}(2x_2 - x_{20}) - x_{30}(2x_3 - x_{30})$$

Thus, $h(\psi_+) = [h(\psi)]_+$. The second equality can be verified in the same way. □

Lemma 3.3 *For each non-empty tetrahedron in $\mathbb{T}^3$, there is a family of power paraboloids containing its lifted representatives in $\mathbb{H}'$.*

Proof: As described in §3.1.1, each non-empty tetrahedron in $\mathbb{T}^3$, say tetrahedron $\overline{a'b'c'd'}$, has a family of representatives in the development of $\mathbb{T}^3$ and each of the representatives is a tetrahedron with its own vertices. Meanwhile, each of the vertices is a representative of site $\bar{a}'$, $\bar{b}'$, $\bar{c}'$ or $\bar{d}'$.

Without loss of generality, let $\hat{a}$, $\hat{b}$, $\hat{c}$ and $\hat{d}$ be the lifted vertices of a representative of $\overline{a'b'c'd'}$. Also let $\tilde{a}$, $\tilde{b}$, $\tilde{c}$ and $\tilde{d}$ be the h-mapped vertices. Then a non-vertical hyperplane $\pi(\widetilde{abcd})$ contains $\tilde{a}$, $\tilde{b}$, $\tilde{c}$ and $\tilde{d}$. As $\pi(\widetilde{abcd})$ is a one-to-one mapping of $\psi(\widehat{abcd})$, $\psi(\widehat{abcd}) = h^{-1}(\pi(\widetilde{abcd}))$ is the power paraboloid containing $\hat{a}$, $\hat{b}$, $\hat{c}$ and $\hat{d}$. □

Figure 3.2 illustrates this lemma in one dimension (i.e., $\mathbb{H}'$ is $\mathbb{R}^2$). Lemmas 3.1, 3.2 and 3.3 have been proved in $\mathbb{R}^3$ by Telley [Tel90]. Here these lemmas are described in $\mathbb{H}'$ space and thereby more general than before. The general position assumption of weighted site set $\bar{S}'$ in $\mathbb{T}^3$ can be described as follows.

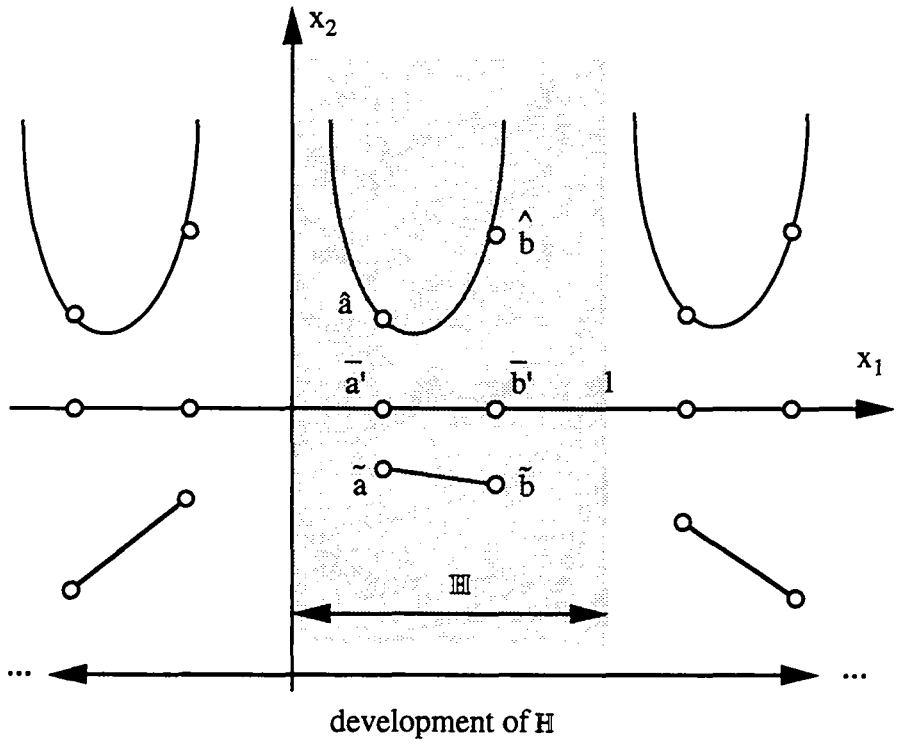

Figure 3.2: $\mathbb{H}$ space and its development $\mathbb{H}'$.

Assumption 1 *The weighted site set $\bar{S}'$ in $\mathbb{T}^3$ is in general position, namely in $\mathbb{H}'$ space there are exactly four lifted representatives of $\hat{S}$ on the same power paraboloid.*

Definition 3.9 *Let $\bar{S}'$ be a set of weighted sites in $\mathbb{T}^3$ and $\hat{S}$ be the lifted representatives of $\bar{S}'$ in $\mathbb{H}'$ satisfying Assumption 1. Then weighted Delaunay diagram of $\bar{S}'$ in $\mathbb{T}^3$, noted as $D_T(\bar{S}')$ is a triangulation of $\bar{S}'$ such that each tetrahedron in the triangulation, say $\overline{a'b'c'd'}$ possesses a family of power paraboloids in $\mathbb{H}'$ space and each of the power paraboloids, say $\psi(\widehat{abcd})$ satisfies*

$$\psi_+(\widehat{abcd}) \bigcap \hat{S} = \emptyset$$

In other words, $\psi_+(\widehat{abcd})$ is empty.

The requirement that each tetrahedron in $D_T(\bar{S}')$ has a family of empty power paraboloids in $\mathbb{H}'$ space is the generalization of the empty sphere criterion in the unweighted case (Definition 3.3).

It is of interest to note that the elements in Laguerre and weighted Delaunay diagram are $3-k$ dual , $0 \leq k \leq 3$ [Aur87]. Following two properties concerning the duality of Laguerre facet and Delaunay edge will be frequently used in the next chapter.

Property 3.1 *For each Delaunay edge in the development of $\mathbb{T}^3$, say ab, its dual (Laguerre) facet is perpendicular to the edge and passing point p_{ab} which is the median of the*

edge and is given by

$$\begin{cases} p_{ab} = b + \lambda |a-b| u_{ba} \\ \lambda = \frac{1}{2}(1 - \frac{a_4 - b_4}{|a-b|^2}) \end{cases} \tag{3.13}$$

where u_{ab} is a unit vector $u_{ab} = (a-b)/|a-b|$.

Corresponding to a Delaunay cell (i.e., the six Delaunay edges), there exist six Laguerre facets. The intersection point of the six facets is called the Laguerre vertex corresponding to the Delaunay cell.

Property 3.2 *If a Delaunay edge is incident to n Delaunay cells, then the Laguerre facet corresponding to the edge is a n-sided facet, i.e., bounded by n Laguerre vertices and n Laguerre edges.*

The proof of these properties can be found in [Rig92]. The global projection property of the weighted Delaunay diagram in $\mathbb{T}^3$ space is as follows.

Theorem 3.3 *Let $\bar{S}'$, $\tilde{S}$, $\hat{S}$ be as above, then the weighted Delaunay diagram $D_{\mathbf{T}}(\bar{S}')$ is the quotient of vertical projection of the superior part of the convex hull of $\tilde{S}$ on the hyperplane with equation $x_4 = 0$.*

Proof: Each non-empty tetrahedron in $\mathbb{T}^3$ is represented by a family of power paraboloids in $\mathbb{H}'$ (Lemma 3.3), each paraboloid corresponds to a non-vertical hyperplane in the same space (Definition 3.9 and Lemma 3.1) and the superior half space of each hyperplane is empty (Lemma 3.2), thus all the hyperplanes form the convex hull of $\tilde{S}$. As each of the hyperplanes in $\mathbb{H}'$ corresponds to a non-empty tetrahedron in the development of $\mathbb{T}^3$, the vertical projection of the superior part of the convex hull on the hyperplane with $x_4 = 0$ is a weighted Delaunay diagram noted as $D_{\mathbf{R}}$. As $\mathbb{T}^3$ is the quotient of $\mathbb{R}^3$ (Equation 3.1), $D_{\mathbf{T}}(\bar{S}')$ *is the quotient of* diagram $D_{\mathbf{R}}$. □

As mentioned in §3.1.2, to construct a weighted Delaunay diagram in $\mathbb{T}^3$, it is sufficient to consider the representatives of $\bar{S}'$ in $]-1,2]^3$.

3.2.2 Local characterization of weighted Delaunay diagram

From the viewpoint of construction of weighted Delaunay diagram, the local characterization may be more important than general definition. In this subsection, the basic structural elements of the diagram, i.e., site, facet, tetrahedron and hexahedron are investigated.

Definition 3.10 *Let $\bar{S}'$, $\hat{S}$, $\tilde{S}$ be as above and $\mathcal{T}$ be a triangulation of $\bar{S}'$ in $\mathbb{T}^3$. Also let $C_+(\tilde{S})$ be the superior part of convex hull of $\tilde{S}$. Then site $\bar{a}'$ is visible in $\mathcal{T}$ if the h-mapped representatives of $\bar{a}'$ are on $C_+(\tilde{S})$. Otherwise, the site is legally invisible in $\mathcal{T}$.*

As a matter of fact, in a weighted Delaunay diagram a site is not necessarily visible. The visible sites connect to each other through facets and the legally invisible site is not incident to any facet. The local character of legally invisible site can be stated as follows.

Lemma 3.4 *A site $\bar{e}' \in \bar{S}'$ is legally invisible in triangulation $\mathcal{T}$ of $\bar{S}'$ in $\mathbb{T}^3$ if*

(i) in $\mathbb{T}^3$, $\bar{e}'$ lies in tetrahedron $\overline{a'b'c'd'}$;

(ii) in $\mathbb{H}'$, $\tilde{e} \in \pi_-(\widetilde{abcd})$.

Proof: From Lemma 3.3, if site $\bar{e}'$ lies in tetrahedron $\overline{a'b'c'd'}$, meanwhile in $\mathbb{H}'$ space $\hat{e}$, a lifted representative of $\bar{e}'$, is lower than power paraboloid $\psi(\widetilde{abcd})$, where $\widetilde{abcd}$ are the lifted vertices of a representative tetrahedron of $\overline{a'b'c'd'}$, then $\hat{e}$ could not be contained by any power paraboloid.

From Lemma 3.2, if $\hat{e} \in \psi_-(\widetilde{abcd})$, then $\tilde{e} \in \pi_-(\widetilde{abcd})$. So, $\tilde{e}$ is lower than any hyperplane which contains four h-mapped representatives. This means that $\tilde{e}$ is not an extreme vertex of the convex hull of $\tilde{S}$. From Theorem 3.3, site $\bar{e}'$ could not appear in triangulation $\mathcal{T}$ for which is from the vertical projection of $C_+(\tilde{S})$ on hyperplane $x_4 = 0$. This completes the proof. □

Definition 3.11 *Let $\bar{S}'$, $\hat{S}$, $\tilde{S}$, $\mathcal{T}$ and $C_+(\tilde{S})$ be as above. Also let $\overline{a'b'c'd'}$ be a non-empty tetrahedron in $\mathcal{T}$. Then facet $\overline{b'c'd'}$ is legal in $\mathcal{T}$ if the hyperplanes corresponding to $\overline{a'b'c'd'}$ are on $C_+(\tilde{S})$. Otherwise, the facet is illegal in $\mathcal{T}$.*

The local character of legal facet can be stated as follows.

Lemma 3.5 *Let $\overline{a'b'c'd'}$ be the sites of a tetrahedron in $\mathbb{T}^3$, then facet $\overline{b'c'd'}$ is legal in triangulation $\mathcal{T}$ of $\bar{S}'$ in $\mathbb{T}^3$ if*

(i) in $\mathcal{T}$, $\overline{a'b'c'd'}$ is adjacent to tetrahedron $\overline{b'c'd'e'}$ by sharing facet $\overline{b'c'd'}$;

(ii) in $\mathbb{H}'$, $\tilde{e} \in \pi_-(\widetilde{abcd})$.

Proof: From Lemma 3.3, a representative of tetrahedron $\overline{a'b'c'd'}$ corresponds to a power paraboloid $\psi(\widetilde{abcd})$ in $\mathbb{H}'$ space and $\psi_+(\widetilde{abcd})$ is empty. From Lemma 3.2, the corresponding hyperplane is $\pi(\widetilde{abcd})$ and $\pi_+(\widetilde{abcd})$ is empty as well, thereby $\tilde{e}$ should be lower than the hyperplane. As $\pi(\widetilde{abcd})$ is above all the h-mapped representatives of $(\tilde{S} - \{\tilde{a}, \tilde{b}, \tilde{c}, \tilde{d}\})$, it is on the convex hull of $\tilde{S}$ and its vertical projection on hyperplane $x_4 = 0$ is a convex hull with four extreme vertices. Hence, $\overline{a'b'c'd'}$ is a tetrahedron in $\mathbb{T}^3$ and facet $\overline{b'c'd'}$ legally exists in $\mathcal{T}$. □

Combining Theorem 3.3 and these two local characters (Lemmas 3.4 and 3.5) of weighted Delaunay diagram, the main assertion of the diagram in $\mathbb{T}^3$ comes out.

Theorem 3.4 *Let $\bar{S}'$ be a weighted site set in $\mathbb{T}^3$ and $\mathcal{T}$ be a triangulation of $\bar{S}'$, then $\mathcal{T}$ is the weighted Delaunay diagram $D_T(\bar{S}')$ if and only if*

(i) every invisible site of $\bar{S}'$ in $\mathcal{T}$ is legally invisible;

(ii) every facet of $\mathcal{T}$ is legal.

Proof: The "only if" part is obvious by Lemmas 3.4 and 3.5. The "if" part can be shown by contradiction, namely, if $\mathcal{T} \neq D_{\mathrm{T}}(\bar{S}')$ then (i) or (ii) must be violated.

Let D_h be the superior part of convex hull of $\tilde{S}$ and $\mathcal{T}_h$ be another network in $\mathbb{H}'$ space by downwards pulling the development of $\mathcal{T}$ to the position of $\tilde{S}$. Also let $\mathcal{T}_h \neq D_h$ and $\bar{e}'$ be a site contained in tetrahedron $\overline{a'b'c'd'}$ in $\mathbb{T}^3$. If $\tilde{e}$ is above $\mathcal{T}_h$, then $\bar{e}'$ is not legally invisible in $\mathcal{T}_h$, thereby (i) is violated. If $\tilde{e}$ is not above $\mathcal{T}_h$, then it should not be above D_h either, for D_h is supposed to be the superior part of convex hull of $\tilde{S}$. Otherwise, some illegal facets must be incident to site $\bar{e}'$ in $\mathcal{T}_h$, thus (ii) is violated. From Theorem 3.3, once $\mathcal{T}_h \neq D_h$, the quotient of $\mathcal{T}_h$ on hyperplane $x_4 = 0$ could not be the weighted Delaunay diagram $D_{\mathrm{T}}(\bar{S}')$. □

Telley has proved that this theorem holds in $\mathbb{T}^2$ [Tel90].

For the purpose of programming, Theorem 3.4 can be written in determinant form [Rig92]. Let $\overline{a'b'c'd'}$ be a positive oriented tetrahedron (i.e., its signed volume is positive) and $\pi(\widehat{abcd})$ be one of its hyperplanes in $\mathbb{H}'$. Also let $\bar{e}' \in \bar{S}'$ be a weighted site. Then the determinant

$$\Delta_{\widehat{abcde}} = \begin{vmatrix} a_1 & a_2 & a_3 & a_4 - (a_1^2 + a_2^2 + a_3^2) & 1 \\ b_1 & b_2 & b_3 & b_4 - (b_1^2 + b_2^2 + b_3^2) & 1 \\ c_1 & c_2 & c_3 & c_4 - (c_1^2 + c_2^2 + c_3^2) & 1 \\ d_1 & d_2 & d_3 & d_4 - (d_1^2 + d_2^2 + d_3^2) & 1 \\ e_1 & e_2 & e_3 & e_4 - (e_1^2 + e_2^2 + e_3^2) & 1 \end{vmatrix} \tag{3.14}$$

denotes the signed volume of the convex hull of $\widehat{abcde}$ in $\mathbb{H}'$ space. If $\Delta_{\widehat{abcde}} \leq 0$, then facet $\overline{b'c'd'}$ is illegal. The local characters of weighted Delaunay digram in $\mathbb{T}^3$ are summarized as following theorem.

Theorem 3.5 *Let $\bar{a}'$, $\bar{b}'$, $\bar{c}'$, $\bar{d}'$ and $\bar{e}'$ be weighted sites in $\bar{S}'$ and $\overline{a'b'c'd'}$ be a positive oriented tetrahedron. Let $\hat{e}$ be a lifted representative of $\bar{e}'$. Also let one of power paraboloids of the tetrahedron be $\psi(\widehat{abcd})$ and the corresponding hyperplane of the power paraboloid be $\pi(\widehat{abcd})$. Then following equivalent relationships hold:*

$$\hat{e} \in \begin{cases} \psi_-(\widehat{abcd}) \\ \psi(\widehat{abcd}) \\ \psi_+(\widehat{abcd}) \end{cases} \Leftrightarrow \tilde{e} \in \begin{cases} \pi_-(\widehat{abcd}) \\ \pi(\widehat{abcd}) \\ \pi_+(\widehat{abcd}) \end{cases} \Leftrightarrow \Delta_{\widehat{abcde}} \begin{cases} > 0 \\ = 0 \\ < 0 \end{cases} \tag{3.15}$$

Proof: The first equivalence is the fact of Lemmas 3.1 and 3.2 and the second one is from [Rig92]. □

As mentioned at the beginning of this chapter, 2D unweighted and weighted Delaunay diagrams have been well documented, it is no surprise to find that Theorems 3.3, 3.4 and 3.5 provided in §3.1 and §3.2 have been proved in $\mathbb{T}^2$ [Tel90]. For the self containing of this thesis, these theorems are described in the four-dimensional $\mathbb{H}$ space which was proposed by Righetti [Rig92]. In $(d+1)$-dimensional $\mathbb{H}$ space defined as $\mathbb{T}^d \times \mathbb{R}$, one can discuss the d-dimensional unweighted or weighted Delaunay diagram in unit flat torus, where $d \geq 2$.

3.3 Dynamic weighted Delaunay diagram

In this section, the normal motion of dynamic weighed Delaunay diagram is defined. After introducing four types of elementary topological transformations, an algorithm which can maintain the diagram in normal motion is presented.

Given a real interval J representing a time interval, weighted site $\bar{a}'(t) \in \bar{S}'(t)$ is called the motion of the site in time interval J if

$$\bar{a}'(t) = (a_1(t),\ a_2(t),\ a_3(t),\ a_4(t)), t \in J \tag{3.16}$$

and $a_i(t)$, $i = 1, 2, 3, 4$, is a continuous function of time $t \in J$. Correspondingly,

$$\bar{S}'(t) = \{\bar{a}'(t) : t \in J,\ \forall\, \bar{a}' \in \bar{S}'\} \tag{3.17}$$

is called the motion of the weighted site set. In addition, $D_{\mathrm{T}}(\bar{S}'(J))$ is called the dynamic weighted Delaunay diagram due to the motion of $\bar{S}'$ in J. In any case, such a continuous motion is called a normal motion, if both the position and weight of a site are allowed to change in time interval J.

Assumption 2 *The weighted site set $\bar{S}' \in \mathbb{T}^3$ in which every site's coordinates and weight are defined as continuous functions of time t is in general motion, namely*

(i) at instant t_1 there exists exactly a subset of weighted sites noted as $\bar{E}' \subset \bar{S}'$ and $|\bar{E}'| = 5$ such that five lifted vertices of a representative of $\bar{E}'$ in $\mathbb{H}'$ space are contained on a power paraboloid (elementary degeneracy at t_1);

(ii) for every $t \in [t_1 - \epsilon,\ t_1[\bigcup]t_1,\ t_1 + \epsilon]$ $\hat{S}$ satisfies Assumption 1 (discrete degeneracy at t_1), where $\epsilon > 0$ and is sufficiently small.

Clearly, under this assumption, the motion of $D_{\mathrm{T}}(\bar{S}'(J))$ in $\mathbb{T}^3$ will face continuous geometric displacement and elementary and discrete topological transformations implied by the continuous motion of $\bar{S}'(J)$.

3.3.1 Elementary topological transformations

When weighted Delaunay diagram $D_{\mathrm{T}}(\bar{S}'(J))$ moves in $\mathbb{T}^3$, there exist facet permutations which are defined as the elementary topological transformations ETT_1 and ETT_2. Apart from these, in the diagram a site may change its status from invisible to visible or vice versa. The first possibility is characterized as the third type elementary topological transformation, namely ETT_3. For the "vice versa", the fourth type of elementary topological transformation is proposed and noted as ETT_4. In fact, it is just an inverse transformation of ETT_3. These four elementary topological transformations are summarized in Figure 3.3. Following the steps of Dobkin and Laszlo [Dob89], Joe [Joe89] and Righetti [Rig92], the elementary topological transformations in the diagram are elaborated as follows. By Lemma 3.5 and Theorem 3.5, if a moving facet is legal or not can be checked as follows.

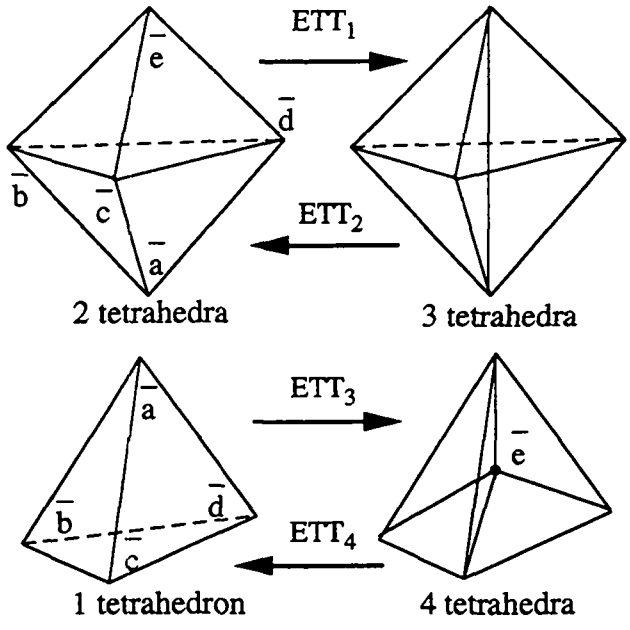

Figure 3.3: Elementary topological transformations.

Lemma 3.6 *Due to the motion of weighted site set $\bar{S}'(J)$, in $D_{\mathrm{T}}(\bar{S}'(J))$ facet $\overline{b'c'd'}$ would change its status from legal to illegal at the instant $\beta_\tau(\overline{b'c'd'})$ which is given by the smallest real solution of the equation*

$$\Delta_{\widetilde{abcde}}(t) = \begin{vmatrix} a_1(t) & a_2(t) & a_3(t) & a_4(t) - a_1(t)^2 - a_2(t)^2 - a_3(t)^2 & 1 \\ b_1(t) & b_2(t) & b_3(t) & b_4(t) - b_1(t)^2 - b_2(t)^2 - b_3(t)^2 & 1 \\ c_1(t) & c_2(t) & c_3(t) & c_4(t) - c_1(t)^2 - c_2(t)^2 - c_3(t)^2 & 1 \\ d_1(t) & d_2(t) & d_3(t) & d_4(t) - d_1(t)^2 - d_2(t)^2 - d_3(t)^2 & 1 \\ e_1(t) & e_2(t) & e_3(t) & e_4(t) - e_1(t)^2 - e_2(t)^2 - e_3(t)^2 & 1 \end{vmatrix} = 0 \qquad (3.18)$$

where tetrahedron $\overline{a'b'c'd'}$ is positive oriented and adjacent to tetrahedron $\overline{b'c'd'e'}$ by sharing facet $\overline{b'c'd'}$ in $D_{\mathrm{T}}(\bar{S}'(J))$.

By Lemma 3.4 and Theorem 3.5, if a moving site is legally invisible or not can be checked as follows.

Lemma 3.7 *A given site $\bar{e}' \in \bar{S}'$ lying in tetrahedron $\overline{a'b'c'd'}$ would change it status from visible to legally invisible at the instant $\beta_\tau(\bar{e}')$ which is given by the smallest real solution of the equation*

$$\Delta_{\widetilde{abcde}}(t) = 0 \qquad (3.19)$$

Notice that Equations 3.18 and 3.19 are the same, but the geometry corresponding to the determinant is different. Suppose each site linearly moves in space, i.e., the position and weight of each site are some linear function of time t, these two equations are degree 5 polynomials of time t. The smallest real root of the polynomial equations can be

determined by some proper numerical method. In our program, all the roots of the polynomial are solved by Sturm (sequence) method [Isa66, Tel90], thus it is easy to choose the smallest real root, if it exists[2]. If in a weighted Delaunay diagram some facets are no longer legal at instant t, the diagram degenerates to a triangulation noted $\mathcal{T}_t$ and a proper topological transformation is required to renovate it as a weighted Delaunay diagram.

Lemma 3.8 *A convex empty[3] hexahedron $\bar{H}$ with extreme vertices $\{\bar{a}', \bar{b}', \bar{c}', \bar{d}', \bar{e}'\}$ in triangulation $\mathcal{T}$ in $\mathbb{T}^3$ can be weighted-Delaunay triangulated as follows.*

(i) Let $\overline{b'c'd'}$ be a facet of $\mathcal{T}$. Also let $\overline{a'b'c'd'}$ and $\overline{b'c'd'e'}$ be two adjacent tetrahedra by sharing $\overline{b'c'd'}$ in $\mathcal{T}$. If facet $\overline{b'c'd'}$ is legal, then the three facets $\overline{a'b'e'}$, $\overline{a'c'e'}$ and $\overline{a'd'e'}$ are all illegal with respect to $\bar{H}$.

(ii) Let $\overline{a'b'c'e'}$, $\overline{a'c'd'e'}$ and $\overline{a'b'd'e'}$ be three tetrahedra of triangulation $\mathcal{T}$ in $\mathbb{T}^3$ sharing the edge $\overline{a'e'}$. If the three facets $\overline{a'b'e'}$, $\overline{a'c'e'}$ and $\overline{a'd'e'}$ are legal, then the facet $\overline{b'c'd'}$ is illegal with respect to $\bar{H}$.

Proof: This lemma is a corollary of Theorem 3.5. Let $\bar{a}'$, $\bar{b}'$, $\bar{c}'$, $\bar{d}'$ and $\bar{e}'$ be the vertices of a convex empty hexahedron $\bar{H}$ in $\mathbb{T}^3$ that can be triangulated by two sets of tetrahedra, i.e., either $\bar{D}_1 = \{\bar{T}_1, \bar{T}_2\} = \{\overline{a'b'c'd'}, \overline{b'c'd'e'}\}$ or $\bar{D}_2 = \{\bar{T}_3, \bar{T}_4, \bar{T}_5\} = \{\overline{a'b'c'e'}, \overline{a'c'd'e'}, \overline{a'b'd'e'}\}$ as in Figures 3.3. Suppose $\bar{D}_1$ is the weighted Delaunay triangulation of $\bar{H}$, then by the determinant of hexahedron, i.e., Equation 3.18 and Theorem 3.5, $\Delta_{\widetilde{abcde}} > 0$. The determinants corresponding to the tetrahedra in $\bar{D}_2$, i.e., $\Delta_{\widetilde{becad}}$, $\Delta_{\widetilde{cedab}}$ and $\Delta_{\widetilde{deacb}}$ can be obtained from $\Delta_{\widetilde{abcde}}$ by three row exchanges[4]. From linear algebra, these three determinants are negative.

Suppose $\bar{D}_2$ is the weighted Delaunay triangulation of $\bar{H}$, then $\Delta_{\widetilde{becad}} > 0$, $\Delta_{\widetilde{cedab}} > 0$ and $\Delta_{\widetilde{deacb}} > 0$, it is easy to show that $\Delta_{\widetilde{abcde}} < 0$. □

This lemma has been proved in unweighted case in $\mathbb{R}^3$ by Joe with the relationship of intersection of circumspheres [Joe89]. In weighted case his proof is no longer valid, while the proof provided here is applicable in 2 and 3D and in both of unweighted and weighted cases.

By Lemma 3.8, to eliminate the illegal facet(s) in a convex empty hexahedron, two types of elementary topological transformations can be defined as follows.

Definition 3.12 *Let $\overline{a'b'c'd'}$ and $\overline{b'c'd'e'}$ be two adjacent tetrahedra sharing facet $\overline{b'c'd'}$ in triangulation $\mathcal{T}$, the convex hull of $\bar{a}', \bar{b}', \bar{c}', \bar{d}', \bar{e}'$ be an empty convex hexahedron and facet $\overline{b'c'd'}$ becomes illegal at instant $\beta_\tau(\overline{b'c'd'})$. Then the facet should be removed from $\mathcal{T}$ and edge $\overline{a'e'}$ and facets $\overline{a'b'e'}$, $\overline{a'c'e'}$ and $\overline{a'd'e'}$ should be inserted into $\mathcal{T}$. Such manipulation in triangulation $\mathcal{T}$ is defined as the first type of elementary topological transformation and noted as ETT_1.*

[2]Here, it is supposed that the root always exists and can be obtained.

[3]The term *empty* means that there is no visible site in the interior of the hexahedron.

[4]Notice that the subscript of these five determinants is written in the way to satisfy the positive orientation requirement.

Definition 3.13 *Let $\overline{a'b'c'e'}$, $\overline{a'c'd'e'}$ and $\overline{a'b'd'e'}$ be three tetrahedra incident to edge $\overline{a'e'}$ in triangulation $\mathcal{T}$, the convex hull of $\bar{a}', \bar{b}', \bar{c}', \bar{d}', \bar{e}'$ be an empty convex hexahedron and the three facets become illegal at instant $\beta_\tau(\overline{a'b'e'}) = \beta_\tau(\overline{a'c'e'}) = \beta_\tau(\overline{a'd'e'})$. Then these three facets and edge $\overline{a'e'}$ should be removed from the triangulation and facet $\overline{b'c'd'}$ should be inserted. Such manipulation in triangulation $\mathcal{T}$ is defined as the second type of elementary topological transformation and noted as ETT_2.*

To activate a site, the third type of elementary topological transformation is defined as follows.

Definition 3.14 *Let site $\bar{e}'$ lie in tetrahedron $\overline{a'b'c'd'}$. Also let site $\bar{e}'$ become visible in $\mathcal{T}$ at instant $\beta_\tau(\bar{e}')$. To activate the site, four edges $\overline{a'e'}$, $\overline{b'e'}$, $\overline{c'e'}$ and $\overline{d'e'}$ and six facets $\overline{a'b'e'}$, $\overline{a'c'e'}$, $\overline{a'd'e'}$, $\overline{b'c'e'}$, $\overline{b'd'e'}$ and $\overline{c'd'e'}$ should be inserted into tetrahedron $\overline{a'b'c'd'}$. Such manipulation in a triangulation is defined as the third type of elementary topological transformation and noted as ETT_3.*

Lemma 3.9 *Let $\overline{a'b'c'e'}$, $\overline{a'c'd'e'}$, $\overline{a'b'd'e'}$ and $\overline{b'c'd'e'}$ be four adjacent tetrahedra by sharing site $\bar{e}'$ in triangulation $\mathcal{T}$. Then six facets $\overline{a'b'e'}$, $\overline{a'c'e'}$, $\overline{a'd'e'}$, $\overline{b'c'e'}$, $\overline{b'd'e'}$ and $\overline{c'd'e'}$ become illegal when site $\bar{e}'$ changes its status from visible to legally invisible.*

Proof: From Theorem 3.5, $\Delta_{\widetilde{abcde}} > 0$ if site $\bar{e}'$ is legally invisible. As the determinants corresponding to the six facets can be obtained from $\Delta_{\widetilde{abcde}}$ by three row exchanges, the six determinants are negative in case $\Delta_{\widetilde{abcde}} > 0$. □

Based on Lemma 3.9, to deactivate site $\bar{e}'$ in triangulation $\mathcal{T}$, another type of elementary topological transformations is defined.

Definition 3.15 *Let $\overline{a'b'c'e'}$, $\overline{a'c'd'e'}$, $\overline{a'b'd'e'}$ and $\overline{b'c'd'e'}$ be four adjacent tetrahedra by sharing site $\bar{e}'$ in triangulation $\mathcal{T}$. Also let site $\bar{e}'$ become legally invisible and its six incident facets become illegal at instant*

$$\beta_\tau(\bar{e}') = \beta_\tau(\overline{a'b'e'}) = \beta_\tau(\overline{a'c'e'}) = \beta_\tau(\overline{a'd'e'}) = \beta_\tau(\overline{b'c'e'}) = \beta_\tau(\overline{c'd'e'}) = \beta_\tau(\overline{b'd'e'})$$

To deactivate the site, facets $\overline{a'b'e'}$, $\overline{a'c'e'}$, $\overline{a'd'e'}$, $\overline{b'c'e'}$, $\overline{b'd'e'}$ and $\overline{c'd'e'}$ and edges $\overline{a'e'}$, $\overline{b'e'}$, $\overline{c'e'}$ and $\overline{d'e'}$ should be deleted from $\mathcal{T}$. Such manipulation in a triangulation is defined as the fourth type of elementary topological transformation and noted as ETT_4.

Are the elementary topological transformations sufficient to maintain a dynamic weighted Delaunay diagram? Concerning $\mathbb{T}^2$, the answer can be found in [Tel89a]. In $\mathbb{T}^3$, Righetti has provided an answer in the case of linear expansion of site weight [Rig92]. Here, his results are generalized to the normal motion of the diagram.

Denoting the time interval J as $[0, T]$ with $T > 0$ and $\mathcal{T}_0$ as the topological triangulation of $D_\mathcal{T}(\bar{S}'(0))$, the topological events induced by the normal motion are characterized by a sequence $\mathcal{T}_i$, $i \geq 0$ such that $f_i : \mathcal{T}_{i-1} \to \mathcal{T}_i$, $i \geq 1$ is the i-th elementary topological transformation occurring at instant t_i which is determined by Equations 3.18 and 3.19.

By Assumption 2, the degeneracy instants t_i satisfy $0 < t_1 < t_2 < ... < T$. The pair (f_i, t_i) is called the i-th topological event. The entire motion of $D_{\mathbf{T}}(\bar{S}'(J))$ is regarded as the sequence of $(\mathcal{T}_i, t_i)$, $i \geq 1$ and $\mathcal{T}_i = f_i \circ f_{i-1} \circ ... \circ f_1(\mathcal{T}_0)$. The main theorem of this subsection is follows.

Theorem 3.6 *Let a weighted site set $\bar{S}'(t)$, $t \in J$, be in normal motion and satisfy Assumptions 1 and 2. Also let $D_{\mathbf{T}}(\bar{S}'(t_i - \epsilon))$ and $D_{\mathbf{T}}(\bar{S}'(t_i + \epsilon))$ be nondegenerate weighted Delaunay diagrams. Then $D_{\mathbf{T}}(\bar{S}'(t_i + \epsilon))$ can be obtained from $D_{\mathbf{T}}(\bar{S}'(t_i - \epsilon))$ by an elementary topological transformation.*

Proof: Suppose at instant t_i, $0 < t_i < T$, $D_{\mathbf{T}}(\bar{S}'(t_i))$ is no longer a weighted Delaunay diagram instead a triangulation $\mathcal{T}_{t_i}$ with some illegal facet. From Assumption 2 and Theorem 3.4, at that instant there exists exactly a subset of weighted sites noted as $\bar{E}' \subset \bar{S}'$ and $|\bar{E}'| = 5$ such that five lifted vertices of a representative of $\bar{E}'$ in $\mathbb{H}'$ space are contained on a power paraboloid and all other power paraboloids contain four lifted representatives as usual. As the corresponding hyperplanes of $\bar{E}'$ were on the superior part of convex hull of $\tilde{S}$ when $t < t_i$ and $\mathcal{T}_{t_i}$ is still the quotient of vertical projection of the superior part of convex hull of $\tilde{S}$ on hyperplane $x_4 = 0$, the hyperplanes are on the superior part of convex hull of $\tilde{S}$ at $t = t_i$. This amounts to saying:

(i) The convex hull of $\bar{E}'$ in $\mathcal{T}_{t_i}$ is composed of legal facets, i.e., external facets of $\bar{E}'$ are legal in $\mathcal{T}_{t_i}$.

(ii) All tetrahedra in $\mathcal{T}_{t_i-\epsilon}$ not incident to the convex hull of $\bar{E}'$ are still legal in $\mathcal{T}_{t_i}$.

(iii) All legally invisible (visible) sites in $\mathcal{T}_{t_i-\epsilon}$ not in the convex hull of $\bar{E}'$ are still legally invisible (visible) in $\mathcal{T}_{t_i}$.

As $\bar{E}'$ possesses five sites, there exist $C_2^5 = 10$ possible edges and $C_3^5 = 10$ possible facets, respectively. All the possible triangulations of $\bar{E}'$ can enumerated to demonstrate that ETT_1, ETT_2, ETT_3 or ETT_4 are sufficient to maintain the convex hull of $\bar{E}'$ and hence triangulation $\mathcal{T}_{t_i}$.

(i) Suppose the convex hull of $\bar{E}'$ has four extreme vertices, then four external facets form a tetrahedron and other six facets are internal ones. In this case, $\bar{E}'$ has two possible configurations.

  (1) If the fifth site is visible, then the six internal facets belong to the triangulation of $\bar{E}'$.

  (2) If the fifth site is invisible, then the six internal facets do not belong to the triangulation of $\bar{E}'$.

(ii) Suppose the convex hull of $\bar{E}'$ has five extreme vertices, then six external facets form a hexahedron and other four facets are internal ones and there is a "free" internal edge which should either be parallel to three internal facets or intersect the fourth one. In this case, $\bar{E}'$ has other two possible configurations.

(3) If the edge exists in the hexahedron, then the first three internal facets belong to the triangulation of $\bar{E}'$.

(4) If the edge does not exist in the hexahedron, then the fourth internal facet belongs to the triangulation of $\bar{E}'$.

Because Configuration (1) will be illegal at t_i, to prevent the legality of triangulation of $\bar{E}'$ and clear up the interior of the convex hull, and thus to renovate triangulation $\mathcal{T}_{t_i}$ as a weighted Delaunay diagram, it suffices to delete the six internal facets in order to deactivate the fifth site. This is the manipulation of triangulation defined by ETT_4. In Configuration (2), for the same reason, six facets and four edges should be added and hence the fifth site is activated. This is an ETT_3 operation.

Since Configurations (3) will be illegal at t_i, for the same reason, the edge and the three internal facets should be replaced by the fourth internal facet which intersects the edge. Evidently, this is an ETT_2. Finally, Configuration (4) requires an inverse manipulation, namely an ETT_1.

In sum, after one ETT, $\mathcal{T}_{t_i}$ will be renovated as a weighted Delaunay diagram until next degeneracy arises. □

This theorem asserts that the dynamic weighted Delaunay diagram can be maintained by the elementary topological transformations, or facet-flips for short, provided the degeneracy induced by the normal motion is elementary and discrete (Assumption 2). Concerning the transformability of an illegal facet, one has following corollary.

Corollary 3.1 *If the normal motion of a given weighted site set $\bar{S}'(t)$ satisfies Assumption 2, then all illegal facets are transformable by the elementary topological transformations.*

Proof: If the degeneracy is elementary and discrete, then each degeneracy of triangulation $\mathcal{T}$ is an event at that instant there exactly exist one family of power paraboloids containing five lifted representatives in $\mathbb{H}'$ space. By Theorem 3.6, the number of illegal facets is one, three or six and the illegal facets exist in the convex hull of the five sites. Still by Theorem 3.6, the illegal facet(s) can be eliminated from triangulation $\mathcal{T}$ by a proper elementary topological transformation and hence the degeneracy can be removed.

On the other hand, any non-transformable illegal facet in triangulation $\mathcal{T}$ is due to a topological event not satisfying Assumption 2. For instance two adjacent facets become illegal at the same instant. Evidently, this event is neither discrete nor elementary and hence violates Assumption 2. Therefore the facets are non-transformable by the elementary topological transformations. This completes the proof. □

Joe [Joe91] has proved that every illegal facet in $\mathcal{T}$ in $\mathbb{R}^3$ is transformable when one constructs a Delaunay diagram by his incremental method. However, his proof can not be applied in normal motion case. To keep the transformability of illegal facet in this case, some new postulate should be made. Corollary 3.1 shows that the postulate is nothing else but Assumption 2.

It is well known that in $\mathbb{R}^3$ the degeneracy of a weighted Delaunay diagram is only caused by more than four lifted sites on a power paraboloid. However, in $\mathbb{T}^3$, besides that, a periodic facet would give rise to a new sort of degeneracy [Rig92]. A periodic facet is such a facet whose three apices are the representatives of the same site $\bar{a}' \in \bar{S}'$. Once periodic facet or illegal and non-transformable facet appear in a triangulation, the simplest solution is to destroy the current triangulation and reconstruct a new one. Hereafter, it is supposed that there is no periodic facet in $D_{\mathrm{T}}(\bar{S}'(J))$.

The implementation of an elementary topological transformation at instant t_i renovates the weighted Delaunay diagram at that instant. As the given weighted site set is in continue motion, some new degeneracy in the diagram would occur during $]t_i, T]$. One may ask whether the number of topological events is finite or not. This question will be answered in next subsection.

3.3.2 Motion algorithm

From Theorem 3.6, a procedure to maintain the dynamic Delaunay diagram can be deduced [Tel89a]. It has been shown that the procedure is an algorithm which can construct Delaunay diagram in $\mathbb{T}^2$ [Tel92b], for which the procedure is called the motion algorithm. Righetti has applied this algorithm in $\mathbb{T}^3$ to construct unweighted and weighted Delaunay diagrams. Very recently, Albers, Mitchell, Guibas and Roos [Alb95] have proved that this algorithm can maintain a dynamic Voronoi diagram in d-dimensional Euclidean space, $d \geq 2$. In this subsection, the algorithm is given in pseudo-code form. The convergence of the algorithm applied in construction and maintenance a dynamic weighted Delaunay diagram in $\mathbb{T}^3$ will be discussed.

To simplify the time complexity analysis of the algorithm, another assumption is proposed.

Assumption 3 *In $D_{\mathrm{T}}(\bar{S}'(t)), t \in J$, once a weighted site changes its status from visible to legally invisible in the diagram, it is not allowed to change back.*

The physical reason of the assumption is that in polycrystal grain growth, once a grain disappears it never reappears, for the matter contained in the grain has been transmitted to its neighboring grains. The algorithmic reason is that under this assumption, one only needs consider the visible sites in current site set $\bar{S}'(t)$. In other words, $\bar{S}'(t)$ is a weighted site set whose size monodecreases with respect to time t.

The *Motion* algorithm inputs time interval $[t, T]$, weighted site set $\bar{S}'(t)$ and weighted Delaunay diagram $D_{\mathrm{T}}(\bar{S}'(t))$ and outputs $\bar{S}'(T)$ and $D_{\mathrm{T}}(\bar{S}'(T))$. In the algorithm, Q is a time-priority queue in which all the potential topological events occuring in $]t, T]$ in current triangulation $\mathcal{T}_t$ are chronologically sorted. The variables $\bar{S}'$ and $D_{\mathrm{T}}(\bar{S}')$ of the algorithm contain $\bar{S}'(t)$ and $D_{\mathrm{T}}(\bar{S}'(t))$ at instant t and $\bar{S}'(T)$ and $D_{\mathrm{T}}(\bar{S}'(T))$ at instant T. By Assumption 3, the applicable elementary topological transformations are confined to ETT_1, ETT_2 and ETT_4. The algorithm can be written as follows.

algorithm *Motion* (t, T, Q, $\bar{S}'$, $D_{\mathrm{T}}(\bar{S}')$);
begin

	ETT_1	ETT_2	ETT_4
No. events deleted from Q	1	3	6
No. events tested in $\mathcal{T}_t$	6	6	4

Table 3.1: The number of topological events corresponds to an ETT (from [Rig92]).

while $Q \neq \emptyset$ **do**
Extract the first event from $Q = \{(\beta_\tau^1, \phi^1), (\beta_\tau^2, \phi^2), (\beta_\tau^3, \phi^3), ...\}$; $t := \beta_\tau^1$;
Perform an ETT in $\mathcal{T}_t$;
Delete the event(s) corresponding to the performed ETT from Q;
Insert events (within $t < \beta_\tau \leq T$ and not yet in Q) induced by the ETT into Q;
endwhile;
end.

As the size of the priority queue Q is proportional to the number of facets which is $O(N^2)$ by Theorem 3.1, the size of the queue is $O(N^2)$. However, after each ETT the queue should be updated. Otherwise said, the performed events should be deleted from Q and the potential events induced by the ETT should be tested and inserted into Q if necessary, as summarized in Table 3.1. To determine the finiteness of the number of topological events, another assumption is introduced.

Assumption 4 *In a given time interval $[t, T]$, every hexahedron in triangulation $\mathcal{T}$ generates $O(1)$ number of topological events.*

This Assumption is true when the given weighted site set $\tilde{S}'(t)$ linearly moves and in the given time interval each site leaves the canonic unit cube at most $O(1)$ number of times. In this case, by Equation 3.18 and Theorem 3.6, a hexahedron generates at most $O(1)$ number of topological events due to the degeneracy of these five sites.

Without loss of generality, let two tetrahedra $\overline{a'b'c'd'}$ and $\overline{b'c'd'e'}$ sharing facet $\overline{b'c'd'}$ be the hexahedron. Facet $\overline{b'c'd'}$ would be illegal if the five lifted vertices of a representative of $\overline{a'b'c'd'e'}$ are contained on a single power paraboloid. From Assumption 4, these instants can only appear at most $O(1)$ number of times. As the sites $\bar{a}'$ and $\bar{e}'$ can be arbitrarily chosen from $\tilde{S}' - \{\bar{b}', \bar{c}', \bar{d}'\}$, the number of the possible choices is bounded by $C_2^{N-3} \in O(N^2)$. The number of imaginable facets of $\tilde{S}'$ is bounded by $C_3^N \in O(N^3)$. Thereby, the upper bound of topological events is $O(N^5)$. This upper bound may be not tight in the case of weighted Delaunay diagram in normal motion in $\mathbb{T}^3$. Nevertheless, concerning the finiteness of the number of topological events, the following lemma is useful[5].

Lemma 3.10 *Given a weighted site set $\tilde{S}'(t)$ of N linearly normal motion satisfying Assumptions 2, 3 and 4, the upper bound of the number of topological events in triangulation $\mathcal{T}$ generated in time interval $[t, T]$ is $O(N^5)$.*

[5]Sophisticated analysis showed that the upper bound could be improved by a linear-factor function in $\mathbb{R}^d$ unweighted case and that the improved one was still not tight [Alb95].

As the analysis of the upper bound comes from the finiteness of the number of simplexes and the elementary topological transformations in a triangulation, by Theorems 3.1 and 3.6, this lemma is valid in $\mathbb{T}^3$ weighted case.

In particular, if in $\bar{S}'(t)$ only one site moves, the upper bound of topological events can be improved as follows. Without loss of generality, let the unique moving site be weighted site $\bar{e}'$. Since there are $O(N^2)$ facets in a triangulation of site set $\bar{S}' - \{\bar{e}'\}$ (Theorem 3.1) and since $\hat{e}$ can cross each power paraboloid of the triangulation at most $O(1)$ number of times (Assumption 4), the following lemma comes out.

Lemma 3.11 *Given a weighted site set $\bar{S}'(t)$ of $N-1$ fixed sites and of one moving site satisfying Assumptions 2, 3 and 4, the upper bound of topological events generated in time interval $[t,T]$ is $O(N^2)$.*

By Lemma 3.10, the convergence of *Motion* algorithm can be stated as follows.

Theorem 3.7 *Under Assumptions 2, 3 and 4, the algorithm Motion computes the normal motion of $D_{\mathbf{T}}(\bar{S}'(J))$ in $O(m \log N)$ time, where m is the number of topological events generated by the motion of $D_{\mathbf{T}}(\bar{S}'(J))$ in $J = [t,T]$.*

Proof: As the size of the priority queue Q is $O(N^2)$, to insert an event in Q at its proper place requires $O(\log N)$ time to complete. The other basic operations, such as the computation of the zeros of the determinants, the topological transformations including the determination of new potential events and the deletion of an element from Q, can be performed in constant time. Therefore, each while-loop of the algorithm requires $O(\log N)$ time to complete. Since there are m such loops, the overall cost of the algorithm is then $O(m \log N)$. The finiteness of m has been shown in Lemma 3.10. □

3.4 Applications of dynamic weighted Delaunay diagram

In this section, three applications of dynamic weighted Delaunay diagram, i.e., the construction of Delaunay diagram, the transformation of a unweighted Delaunay diagram to a weighted one and the simulation of grain growth are presented. In these applications, the *Motion* algorithm is used to manage the maintenance of the diagram. The convergence of the algorithm in each of the applications is discussed separately.

3.4.1 Construction of Delaunay diagram

Righetti has proved that under certain conditions, one can choose two sites from $\bar{S}$ and their representatives to construct a nondegenerate Delaunay diagram in $\mathbb{T}^3$ by an ad hoc method in $O(N)$ time [Rig92]. Suppose a weighted Delaunay diagram with $(i-1)$ sites has been constructed and these $(i-1)$ sites are with zero-weight. The insertion of the

i-th site into the diagram may be treated as a special motion of the diagram, i.e., the weight of the i-th site changes from -1 to 0 in time interval $[0,1]$. Denoting the site as $\bar{e}'$, its weight is thus a function of time, viz,

$$e_4(t) = e_4^0 + (e_4^1 - e_4^0)t = -1 + t,\ 0 \le t \le 1 \tag{3.20}$$

Suppose site $\bar{e}'$ lies in tetrahedron $\overline{a'b'c'd'}$, from Equation 3.18, the site becomes legally visible at instant t which is given by

$$\begin{vmatrix} a_1 & a_2 & a_3 & -a_1^2-a_2^2-a_3^2 & 1 \\ b_1 & b_2 & b_3 & -b_1^2-b_2^2-b_3^2 & 1 \\ c_1 & c_2 & c_3 & -c_1^2-c_2^2-c_3^2 & 1 \\ d_1 & d_2 & d_3 & -d_1^2-d_2^2-d_3^2 & 1 \\ e_1 & e_2 & e_3 & -1+t-e_1^2-e_2^2-e_3^2 & 1 \end{vmatrix} = t \begin{vmatrix} a_1 & a_2 & a_3 & 0 & 1 \\ b_1 & b_2 & b_3 & 0 & 1 \\ c_1 & c_2 & c_3 & 0 & 1 \\ d_1 & d_2 & d_3 & 0 & 1 \\ e_1 & e_2 & e_3 & 1 & 1 \end{vmatrix}$$

$$+ \begin{vmatrix} a_1 & a_2 & a_3 & -a_1^2-a_2^2-a_3^2 & 1 \\ b_1 & b_2 & b_3 & -b_1^2-b_2^2-b_3^2 & 1 \\ c_1 & c_2 & c_3 & -c_1^2-c_2^2-c_3^2 & 1 \\ d_1 & d_2 & d_3 & -d_1^2-d_2^2-d_3^2 & 1 \\ e_1 & e_2 & e_3 & -1-e_1^2-e_2^2-e_3^2 & 1 \end{vmatrix} = tD_a + D_b = 0$$

Finally, the instant comes to

$$t = -\frac{D_b}{D_a},\ t < 1 \tag{3.21}$$

This means that in triangulation $\mathcal{T}_{i-1}$ at instant t an ETT_3 should be performed to activate site $\bar{e}'$. The motion of $\bar{e}'$ is illustrated in Figure 3.4 in two dimensions, i.e., site $\bar{e}'$ lies in Delaunay cell $\overline{a'b'c'}$. After the facet-flip operation, the internal facets of tetrahedron $\overline{a'b'c'd'}$ are legal. However, the external facet of $\overline{a'b'c'd'}$ may no longer be legal after the operation and hence some potential topological events arise within $]t,1]$. Here, *Motion* algorithm is called to manage the treatment of these potential events.

In sum, given an initial Delaunay diagram that contains two sites of $\bar{S}$ in $\mathbb{T}^3$, one can construct a Delaunay diagram $D_T(\bar{S})$ of a set $\bar{S}$ of $N \ge 2$ sites in $\mathbb{T}^3$. The constructive algorithm is as follows. It inputs the site set $\bar{S}$ and outputs the Delaunay diagram $D_T(\bar{S})$.

algorithm *Delaunay* ($\bar{S}$, $D_T(\bar{S})$);
begin
Set triangulation $\mathcal{T}_0 := \emptyset$; Initialize Q to empty queue;
Construct an ad hoc initial Delaunay diagram $\mathcal{T}_2$ with two sites, say $\bar{v}_1$ and $\bar{v}_2$ of $\bar{S}$;
for $i := 3$ **to** N **do**
Find the tetrahedron in $\mathcal{T}_{i-1}$, say $\overline{a'b'c'd'}$, that contains site $\bar{v}_i'$ in its interior;
Calculate the instant $t = \beta_\tau(\bar{v}_i')$;
Replace $\overline{a'b'c'd'}$ by four tetrahedra $\overline{a'b'c'v_i'}$, $\overline{a'b'd'v_i'}$, $\overline{a'c'd'v_i'}$ and $\overline{b'c'd'v_i'}$, thus $\mathcal{T}_i$;
Add four facets $\overline{a'b'c'}$, $\overline{a'b'd'}$, $\overline{a'c'd'}$ and $\overline{b'c'd'}$ into stack Q if they become illegal in]t,1];
if Q is not empty **then** *Motion*(t, 1, Q, $\{\bar{v}_1', ..., \bar{v}_i'\}$, $\mathcal{T}_i$);
endfor;

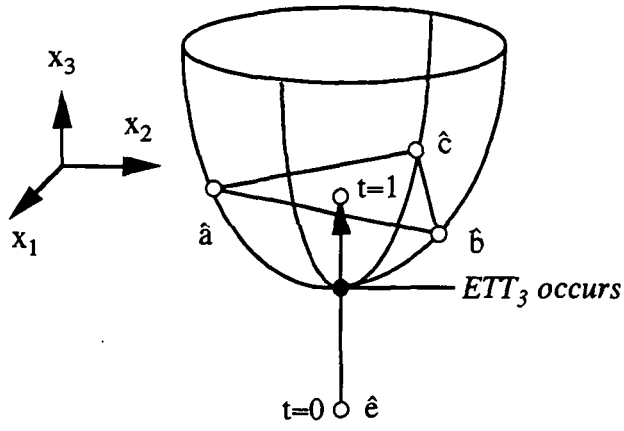

Figure 3.4: Weighted site $\bar{e}'$ is activated at instant t.

$D_{\mathbb{T}}(\bar{S}) := \mathcal{T}_N$;
end.

Theorem 3.8 *Under Assumption 2, the algorithm Delaunay produces the desired output in $O(N^3 \log N)$ time.*

Proof: The initial Delaunay diagram can be constructed in $O(N)$ time [Rig92]. The remaining sites are inserted into the diagram one by one. It remains to show that the Delaunay diagram can be maintained with a finite number of facet-flip steps after each insertion. Precisely, one should show

(i) Let $\mathcal{T}_{i-1}$ be a Delaunay diagram of the first $i-1$ sites of $\bar{S}$ in $\mathbb{T}^3$ and the i-th site become legally visible at instant t in the diagram. Then an ETT_3 in the triangulation produces a new triangulation $\mathcal{T}_i^0$ which is a Delaunay diagram. With the continuous motion of site $\bar{v}_i'$, the diagram would be degenerate at an instant in $]t, 1]$. In this case, another facet-flip is required to generate triangulation $\mathcal{T}_i^1$. Suppose after m facet-flip steps, in $\mathcal{T}_i^m$ there is no illegal facet.

(ii) m is finite;

(iii) $\mathcal{T}_i^m$ is a Delaunay diagram of the first i sites of $\bar{S}$ in $\mathbb{T}^3$.

The proof of (i) amounts to showing that every illegal facet is transformable which has been shown in Corollary 3.1. Therefore, from $\mathcal{T}_i^0$ one can get $\mathcal{T}_i^1$,..., just to $\mathcal{T}_i^m$ by ETT_1 and ETT_2. By Lemma 3.11, (ii) is true, i.e., $m = O(N^2)$. While (iii) is equivalent to showing that the facet-flip sequence does not stop on a triangulation $\mathcal{T}_i^j, 0 \leq j < m$. From Theorem 3.4, if every illegal facet has been replaced by the legal one, then the triangulation is a weighted Delaunay diagram. As $v_{i4}(1) = 0$ and $\bar{v}_i'(t)$ is the unique moving site in $\mathcal{T}_i$, $\mathcal{T}_i^m$ is a Delaunay diagram of the first i sites.

The time complexity of the algorithm can be analyzed as follows. In for-loop, to find the embedding tetrahedron of site $\bar{v}_i'$ needs $O(N^2)$ time, for the number of tetrahedra is $O(N^2)$ by Theorem 3.1. The basic operations, such as separating a tetrahedron into four, searching a neighboring tetrahedron from a known facet, checking facet legality and constructing initial Q, can be done in constant time. By Lemma 3.11 and Theorem 3.7, the maintenance of $\mathcal{T}_i$ needs $O(N^2 \log N)$ time to complete. The for-loop is exactly done $N-2$ times. Therefore, the overall cost of algorithm *Delaunay* is $O(N^3 \log N)$. □

In this subsection, it has been shown that the constructive algorithm proposed by Righetti [Rig92] can compute a desired Delaunay diagram of site set $\bar{S}$ in $\mathbb{T}^3$ in a finite number of facet-flip steps. Since in the three-dimensional unit flat torus $\mathbb{T}^3$ all facets are interior ones of a triangulation $\mathcal{T}$ and all illegal facets are transformable under Assumption 2, the proof of the convergence of algorithm *Delaunay* is simpler than that in $\mathbb{R}^3$ (see [Joe89, Joe91]). From the viewpoint of the flip procedure, a principal difference between $\mathbb{T}^2$ and $\mathbb{T}^3$ is that in $\mathbb{T}^2$, the edge-flip procedure does not change the number of cells in a triangulation, while in $\mathbb{T}^3$, after each facet-flip the number changes. In the weighed case the sequence of circumspherical radius [Joe91] is meaningless in the sense of measuring a triangulation. Otherwise said, a suitable measure of a triangulation which monodecreases with facet-flips in 3D weighted case has not yet found. However, by Lemma 3.11, this difficulty has been avoided.

3.4.2 Construction of weighted Delaunay diagram

As the weighted Delaunay diagram is a generalization of unweighted one by associating a specific weight with each site, the Delaunay diagram can be considered as a special case of the weighted Delaunay diagram in which all site weights equal to zero. Then, the construction of weighted one can be treated as a process in which the sites change their weights from zero to specific values, while their positions are fixed. Because the result, i.e., a weighted Delaunay diagram is much more interesting than the process itself, the motion used for simulating the weight expansion can be freely defined. Suppose the weight is a continuously linear function of time $t \in [0,1]$ and all weights increase such that for $t = 1$ all weights reach their final values, viz

$$\bar{a}'(t) = (a_1, a_2, a_3, a_4(t)),\ \forall\, \bar{a}'(t) \in \bar{S}'(t) \tag{3.22}$$

and

$$a_4(t) = a_4^0 + (a_4^1 - a_4^0)t,\ 0 \le t \le 1 \tag{3.23}$$

where a_4^0 and a_4^1 are the weight of site $\bar{a}'$ at $t = 0$ and $t = 1$, respectively. Considering in time interval $J = [0,1]$, every linear expansion of weight is a motion with $a_4(0) = a_4^0$ and $a_4(1) = a_4^1$, $\forall \bar{a}' \in \bar{S}'$, meanwhile the positions of the sites are fixed, then $\bar{S}'(J)$ is the collection of all these motions with $\bar{S}'(0) = \bar{S}$.

In this simplified case of normal motion, the polynomial determined when a facet becomes illegal is a first-order equation. Suppose $a_4^0 = 0$, $\forall \bar{a}' \in \bar{S}'$, from Equation 3.18, a

facet, say $\overline{b'c'd'}$ shared by tetrahedra $\overline{a'b'c'd'}$ and $\overline{b'c'd'e'}$ becomes illegal at instant t which is given by

$$\begin{vmatrix} a_1 & a_2 & a_3 & a_4^1 t - a_1^2 - a_2^2 - a_3^2 & 1 \\ b_1 & b_2 & b_3 & b_4^1 t - b_1^2 - b_2^2 - b_3^2 & 1 \\ c_1 & c_2 & c_3 & c_4^1 t - c_1^2 - c_2^2 - c_3^2 & 1 \\ d_1 & d_2 & d_3 & d_4^1 t - d_1^2 - d_2^2 - d_3^2 & 1 \\ e_1 & e_2 & e_3 & e_4^1 t - e_1^2 - e_2^2 - e_3^2 & 1 \end{vmatrix} = t \begin{vmatrix} a_1 & a_2 & a_3 & a_4^1 & 1 \\ b_1 & b_2 & b_3 & b_4^1 & 1 \\ c_1 & c_2 & c_3 & c_4^1 & 1 \\ d_1 & d_2 & d_3 & d_4^1 & 1 \\ e_1 & e_2 & e_3 & e_4^1 & 1 \end{vmatrix}$$

$$+ \begin{vmatrix} a_1 & a_2 & a_3 & -a_1^2 - a_2^2 - a_3^2 & 1 \\ b_1 & b_2 & b_3 & -b_1^2 - b_2^2 - b_3^2 & 1 \\ c_1 & c_2 & c_3 & -c_1^2 - c_2^2 - c_3^2 & 1 \\ d_1 & d_2 & d_3 & -d_1^2 - d_2^2 - d_3^2 & 1 \\ e_1 & e_2 & e_3 & -e_1^2 - e_2^2 - e_3^2 & 1 \end{vmatrix} = D'_a t + D_b = 0$$

Finally, the instant comes to

$$t = -\frac{D_b}{D'_a}, \text{ if } D'_a > 0 \tag{3.24}$$

Lemma 3.12 *Let $\bar{S}'(0) \to \bar{S}'(1)$ be a linear expansion of weight and satisfy Assumptions 1 and 2, then the motion automatically satisfies Assumption 3.*

Proof: By Assumption 1, at $t_1 - \epsilon$ each power paraboloid in $\mathbb{H}'$ exactly contains four lifted representatives of $\hat{S}(t_1 - \epsilon)$. Assuming site $\bar{e}'$ changes its status from visible to invisible at t_1. From Theorem 3.6, at t_1 lifted representative $\hat{e}$ is on power paraboloid $\psi(\widehat{abcd})$. By Equation 3.24, t_1 is the unique moment when $\bar{e}'$ could change from visible to invisible. From the continuity of motion, once the representative is lower than the power paraboloid, it could not move on or above the power paraboloid again. □

This Lemma means that to transform an unweighted Delaunay diagram to a weighted one, elementary topological transformations ETT_1, ETT_2 and ETT_4 are sufficient, as long as the weighted site set satisfies Assumptions 1 and 2. Hence the transformation algorithm can be written in pseudo-code form as follows.

algorithm *Weighting* ($\bar{S}'$, $D_{\mathrm{T}}(\bar{S}')$);
begin
  Set triangulation $\mathcal{T} := D_{\mathrm{T}}(\bar{S})$; Initialize Q to empty queue;
  for all facets in $\mathcal{T}$ **do**
    if a facet becomes illegal at instant $0 < t \leq 1$ **then** put the potential event into Q;
  endfor
  if Q is not empty **then** *Motion*(0, 1, Q, $\bar{S}'$, $\mathcal{T}$);
  endfor;
  $D_{\mathrm{T}}(\bar{S}') := \mathcal{T}$;
end.

Theorem 3.9 *Under Assumption 2, algorithm Weighting computes desired output in* $O((m + N^2)\log N)$ *time, where* m *is the number of topological events induced by the linear expansion of site weight.*

Proof: Since the initial construction of Q requires $O(N^2 \log N)$ to complete and the time complexity of *Motion* algorithm is $O(m \log N)$, the overall cost of the algorithm is then $O((m + N^2)\log N)$. By Lemma 3.10, the number of topological transformations occuring in the motion, m is finite. This completes the proof. □

The algorithms *Delauany* and *Weighting* which are both based on the *Motion* algorithm are not optimal, as in $\mathbb{R}^3$ the algorithms for computing unweighted and weighted Delaunay diagram with time complexity of $O(N^2 \log N)$ have been shown [Joe91, Aur87]. However, what we concern is to provide an efficient and safe tool to construct as well as maintain a dynamic Delaunay diagram. While the *Motion* algorithm has a big advantage, i.e., a triangulation is maintained all along the computation.

3.4.3 Simulation of grain growth

It is well known that the microstructure of polycrystalline materials at the level of grain and grain boundary can be idealized as a convex cell complex, i.e., a Voronoi-like diagram[6]. To precisely represent the size of cells, the Laguerre diagram is employed. Moreover, by Theorem 2.1, the Laguerre diagram is a very suitable mathematical model because the continuous geometrical movement and discrete topological transformation can be precisely emulated in three dimensions. This is why in this study, the Laguerre diagram is chosen as a tool to simulate normal grain growth in polycrystalline materials. The process is simulated in the unit flat torus $\mathbb{T}^3$, essentially because this space allows to deal with an infinite-like medium without the additional difficulties that borders will pose.

The knowledge of the normal grain growth summarized in Chapter 2 concerns the principles of movement of grain boundary and grain boundary junction. To simulate the grain growth by a dynamic Laguerre diagram or a dynamic weighted Delaunay diagram, first of all, the site motion equation should be derived based on the principles. This will be one of the main topics in next chapter. It will be shown that the motion of $\bar{S}'(t)$ which emulates the motion of grains can be written as a system of differential equations whose variables are exactly the weighted sites. Due to the complexity of the motion equation and the necessity of topological transformations, it is not possible to solve the equations continuously. A practical solution for the problem is then to discretize the time into sufficiently small intervals for which approximate solutions of the motion equation are suitable. Actually, a linear approximation is used in our simulations. Normal motion of weighted site set $\bar{S}'(t)$ is used for simulating normal grain growth. In other words, the positions and weights of sites are some functions of the diagram itself and time t. It is

[6] Actually, several available models use a 3D Voronoi diagram as the initial state of their simulation, e.g., in [Kur93] and [Fuc95].

natural to ask whether the physical process can be simulated by the mathematical model. This question has been partly answered by the following algorithm.

The algorithm inputs the simulation time upper bound T, the lower bound of number of visible sites in $\bar{S}'(T)$, noted as N_T, $N_T \leq N$ and a set $\bar{S}'$ of N weighted sites. The weighted site set is generated such that the distribution of Laguerre cell size and shape in $L_T(\bar{S}')$ is consistent with the statistics from real polycrystalline materials [Joh39, Rig92]. The output of the algorithm is the weighted Delaunay diagram $D_T(\bar{S}'(t))$.

algorithm *Growth* ($\bar{S}'$, $D_T(\bar{S}')$, T, N_T)
begin
  $t := 0$; $n_t :=$ the number of visible sites in $D_T(\bar{S}')$;
  while $t < T$ and $n_t > N_T$ **do**
    Calculate the current simulation step length δ;
    Calculate the velocity of sites in $D_T(\bar{S}'(t))$;
    Calculate the potential event queue Q;
    if Q is not empty **then** *Motion*(t, $t+\delta$, Q, $\bar{S}'(t)$, $D_T(\bar{S}'(t))$);
    $t := t + \delta$; $n_t :=$the number of visible sites in $D_T(\bar{S}'(t))$;
  endwhile;
end.

To calculate the velocity of sites, Laguerre diagram $L_T(\bar{S}'(t))$ is constructed by the duality of weighted Delaunay diagram $D_T(\bar{S}'(t))$ in $O(N^2)$ time. The velocity of Laguerre vertex is computed according to the mechanism of grain boundary migration. Transforming the velocity to its supporting weighted site, the site velocity is then determined.

Theorem 3.10 *Under Assumptions 2, 3 and 4, the general step of algorithm Growth can be completed in $O((m+N^2)\log N)$ time, where m is the number of topological events induced by the normal motion of the site set $\bar{S}'(t)$ in time interval $[t, t+\delta]$.*

Proof: In while-loop of the algorithm (i.e., the general step) a Laguerre diagram is constructed in $O(N^2)$ time. It will be shown[7] that the calculation of the velocity of $\bar{S}'$ requires $O(N^2)$ to complete. The construction of initial potential topological events queue needs $O(N^2 \log N)$ time. By Theorem 3.7, the maintenance of $D_T(\bar{S}'(t))$ in $[t, t+\delta]$ can be completed in $O(m \log N)$ time, where m is the number of topological events induced by the normal motion of $\bar{S}'(t)$ in the step. Totally, the general step needs $O((N^2+m)\log N)$ time to complete. □

In practice, the simulation time interval $[0, T]$ is divided into a huge number of simulation steps. Suppose the simulation step length is uniform, then the global time-complexity of *Growth* algorithm is $O(\frac{T}{\delta}(m+N^2)\log N))$, where m is the maximum of the number of topological events induced by the normal motion of $\bar{S}'(t)$ in a step.

[7] In §4.1.3, it is shown that the calculation of the velocity of $\bar{S}'$ needs $O(N^2)$ time to complete by *Gradient* algorithm.

3.5 Summary

In this chapter, a special three-dimensional space, so-called unit flat torus is introduced. Triangulation, Delaunay diagram and then weighted Delaunay diagram in the space are defined. Moreover, the maintenance of dynamic Delaunay diagram in the space is studied. Here the dynamic Delaunay diagram means the sites of the diagram are in normal motion and satisfy general position and general motion condition (Assumptions 1 and 2). Corresponding algorithms are presented. The outcome of this chapter can be summarized as follows.

(i) Given a set $\bar{S}$ of N sites in $\mathbb{T}^3$, its Delaunay diagram can be constructed by *Delaunay* algorithm in $O(N^3 \log N)$ time.

(ii) Suppose each site weight linearly increases from zero to a specific value, a Delaunay diagram of the site set can be transformed to the weighted one by *Weighting* algorithm in $O((m+N^2)\log N)$ time, where m is the number of topological events due to the site set motion.

(iii) Let site set $\bar{S}'(t)$, $t \in [0,T]$ be in linearly normal motion and satisfy the assumption that once a site changes its status from visible to invisible, it never change back (Assumption 3). Also let $D_{\mathrm{T}}(\bar{S}'(0))$ be a weighted Delaunay diagram. Then the algorithm *Growth* turns out weighted Delaunay diagram $D_{\mathrm{T}}(\bar{S}'(T))$ in $O(\frac{T}{\delta}(m+N^2)\log N)$ time, where δ is the simulation step length and m the maximum of the number of topological events occuring in a single step.

Notice that all the time-complexity analysis is based on Assumption 4, i.e., a hexahedron in triangulation $\mathcal{T}$ generates at most $O(1)$ number of topological events. This assumption is true, as long as the weighted site set $\bar{S}'(t)$ is in linearly normal motion and in a given time interval each site leaves the canonic unit cube at most $O(1)$ number of times.

The data structure representing a weighted Delaunay diagram in $\mathbb{T}^3$ has been studied by Righetti [Rig92]. The weighted Delaunay diagram is represented by $O(N^2)$ facet-edge data elements which refer to the site set $\bar{S}'$. Whereas the Laguerre diagram is constructed in time $O(N^2)$ if needed.

It is worth to mention here that each site in the weighted site set could move out the canonical unit cube, for $\bar{S}'$ is in normal motion. Theoretically, it does not pose any problem to *Growth* algorithm. Since $\bar{S}'$ is just the class of representatives of sites in the canonical unit cube, wherever a representative moves to, its class is still in the canonical cube. For instance, when a site leaves the cube from $x_1 = 1$ plane, it reenters the cube through $x_1 = 0$ plane. With the continuously normal motion, some site weights would become negative and hence violate the definition of weighted site set in $\mathbb{T}^3$. From the definition of Laguerre diagram, the diagram is unchanged upon adding the same constant to all the site weights. So, all the weights can be kept positive by adding an appropriate constant once some weight is less or equal to zero.

Now that normal grain growth process in polycrystalline materials automatically satisfies Assumption 3, each grain corresponds to a cell in the dynamic Laguerre diagram and each cell possesses a weighted site, *Growth* algorithm can be used to simulate the process, provided the site motion equation realistically characterizes the physical motion of grains in a grain system. With the expectation that by available knowledge of the dynamic Laguerre diagram and of grain boundary migration one can derive such a motion equation, this chapter is finished.

Chapter 4

Three-Dimensional Laguerre Model

Suppose an aggregate of polycrystalline grains has been idealized as a Laguerre diagram, or a Laguerre cell complex in the three-dimensional unit flat torus, a motion equation of the weighted site of the diagram can be derived. Concerning the interfacial energy in the diagram, the decrease of the energy brings about the driving forces exerted on Laguerre vertices. By properly transforming the forces to weighted sites and considering the Laguerre diagram as a pure dissipative system, the motion equation characterizing the velocity of weighted sites can be obtained. The only free variables in the equation are the sites (coordinates and weight). A tetrahedron-based algorithm is proposed for computing the velocity.

After isotropic growth simulation, the anisotropic growth simulation is explored under the assumption that the specific grain boundary energy is determined by the misorientation of adjacent grains and the grain boundary mobility is isotropic. In large scale simulation, the main attributes of grain growth process are observed in both of isotropic and anisotropic cases, i.e.,

(1) The average cell size increases obeying the grain growth power law [Bur52].

(2) The distribution of normalized cell size and shape is time-invariant in long-term regime.

(3) The distribution is well consistent with the experimental data from the specimens of aluminum oxide [Car87] and 3D pseudo-atomic Potts simulation [And89, Rig89].

To simplify notation, in this chapter, the weighted site set in the three-dimensional unit flat torus $\mathbb{T}^3$ is noted as S', the Laguerre diagram of S' as $L(S')$ and the weighted Delaunay diagram as $D(S')$. Moreover, the unit flat torus distance $d_{\mathbb{T}}(.,.)$ is noted as $d(.,.)$.

4.1 Motion equation

In this section, a motion equation is derived for the three-dimensional Laguerre diagram in which the weighted site set is in normal motion. The equation can be looked as the three-

dimensional generalization of the one used in 2D by Telley, Liebling, Mocellin and Righetti [Tel89a, Tel92a]. First the way to calculate the interfacial area of Laguerre diagram is discussed. Then the motion equation is derived based on Burke and Turnbull's grain boundary energy equation, namely Equation 2.4. Finally, a corresponding algorithm for computing the velocity of weighted sites is given.

In this section, each site of S' is noted as $a' = (a, r_a)$, where $a = (a_1, a_2, a_3)$ is the coordinate of the site in $\mathbb{T}^3$ and $r_a^2 = a_4$ is the square of the radius of the sphere.

4.1.1 Interfacial energy in Laguerre diagram

The basic properties of the Laguerre and weighted Delaunay diagrams have been discussed in Chapter 3. In a weighted Delaunay cell (a tetrahedron, for short), the point where a Delaunay edge and its corresponding Laguerre facet intersect is called an l_2 point (e.g., point p_{ab}) and the point where three Laguerre facets perpendicularly intersect a Delaunay facet an l_3 point (e.g., point p_{abc}) as shown in Figure 4.1.

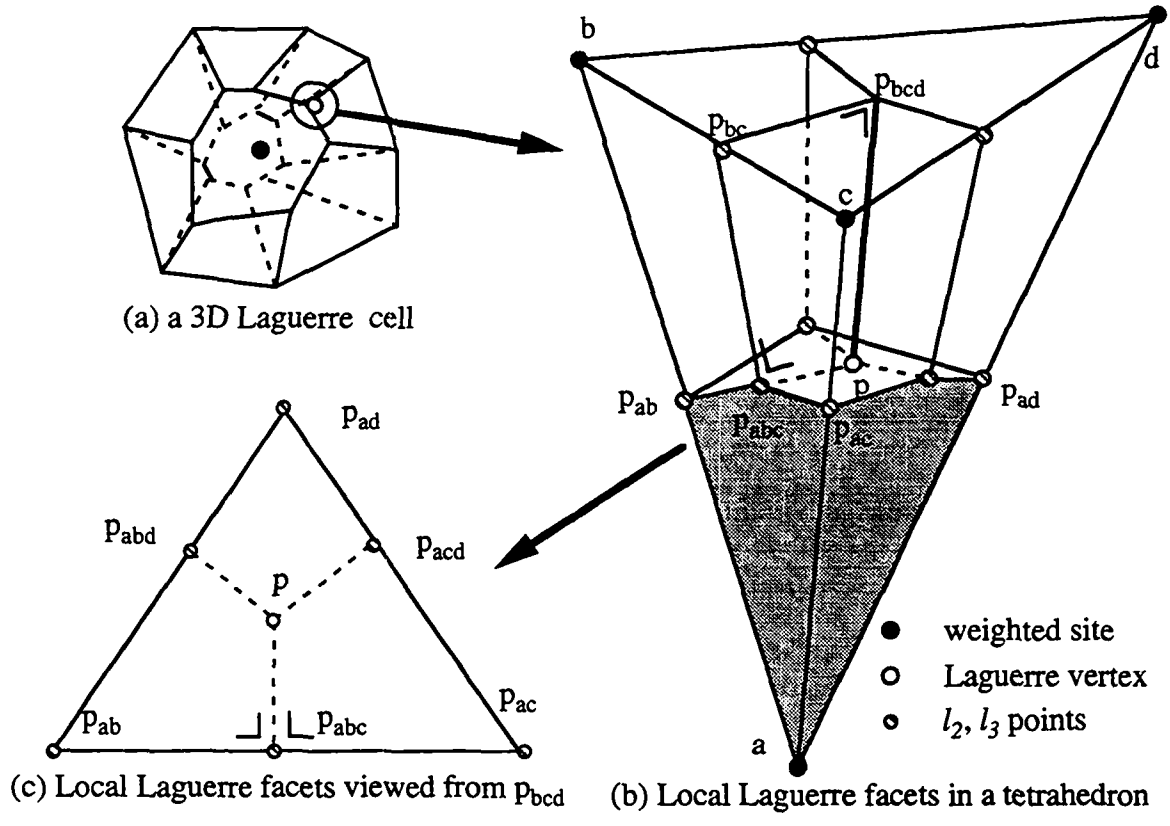

Figure 4.1: Laguerre facets present in a Delaunay cell.

The interfacial area of Laguerre diagram $L(S')$ equals

$$A = \frac{1}{2} \sum_i \sum_j A_{ij} \tag{4.1}$$

where A_{ij} is the area of facet j of cell i; $\sum_i$ and $\sum_j$ are over the cells in $L(S')$ and the facets of each cell, respectively. The fragments of Laguerre facets present in a Delaunay cell are referred to as the local Laguerre facets of the Delaunay cell. Figure 4.1 shows that the local facets are indeed six quadrilaterals. Therefore, the area of local Laguerre facets in a tetrahedron, say (a, b, c, d) is given by

$$A_p = \sum_{k=1}^{6} A_k(p) \tag{4.2}$$

where p is the Laguerre vertex corresponding to the tetrahedron and $A_k(p)$ the area of the quadrilateral k.

Having obtained Laguerre vertex p is in tetrahedron *abcd*, according to the perpendicularity among the facets and edges, local Laguerre facet area in tetrahedron *abcd* can be explicitly written as:

$$\begin{aligned} A_p \;=\; & \tfrac{1}{2}\{d(p,p_{abc})[d(p_{abc},p_{ab}) + d(p_{abc},p_{bc}) + d(p_{abc},p_{ac})] \\ & +d(p,p_{abd})[d(p_{abd},p_{ab}) + d(p_{abd},p_{bd}) + d(p_{abd},p_{ad})] \\ & +d(p,p_{acd})[d(p_{acd},p_{ac}) + d(p_{acd},p_{cd}) + d(p_{acd},p_{ad})] \\ & +d(p,p_{bcd})[d(p_{bcd},p_{bc}) + d(p_{bcd},p_{cd}) + d(p_{bcd},p_{bd})]\} \end{aligned} \tag{4.3}$$

In this equation, each quadrilateral is separated as two right-angled triangles, thus A_p is the sum of the area of theses twelve triangles. A unit normal system for the tetrahedron is established as follows.

Definition 4.1 *Each facet of a tetrahedron has a unit normal which is perpendicular to the facet and oriented to the interior of the tetrahedron and is written in single subscript, e.g.,*

$$u^{\perp}_{abc} = \frac{(b-a)\times(c-b)}{|(b-a)\times(c-b)|}$$

Definition 4.2 *Each edge has two unit normals which are perpendicular to the edge, on the incident facets and oriented to the interior of the facets, e.g.* $u^{\perp}_{ab,abc}$ $(u^{\perp}_{ab,abd})$ *is on facet abc (abd), perpendicular to edge ab and oriented to the internal of triangle abc (abd):*

$$u^{\perp}_{ab,abc} = \frac{u^{\perp}_{abc}\times(a-b)}{|u^{\perp}_{abc}\times(a-b)|}$$

and

$$u^{\perp}_{ab,abd} = \frac{u^{\perp}_{abd}\times(a-b)}{|u^{\perp}_{abd}\times(a-b)|}$$

By the unit normals, A_p can be written in scalar product form:

$$\begin{aligned} A_p \;=\; & \tfrac{1}{2}\{\langle p-p_{abc}, u^{\perp}_{abc}\rangle[\langle p-p_{ab}, u^{\perp}_{ab,abc}\rangle + \langle p-p_{bc}, u^{\perp}_{bc,abc}\rangle + \langle p-p_{ac}, u^{\perp}_{ac,abc}\rangle] \\ & \langle p-p_{abd}, u^{\perp}_{abd}\rangle[\langle p-p_{ab}, u^{\perp}_{ab,abd}\rangle + \langle p-p_{bd}, u^{\perp}_{bd,abd}\rangle + \langle p-p_{ad}, u^{\perp}_{ad,abd}\rangle] \\ & \langle p-p_{acd}, u^{\perp}_{acd}\rangle[\langle p-p_{ac}, u^{\perp}_{ac,acd}\rangle + \langle p-p_{cd}, u^{\perp}_{cd,acd}\rangle + \langle p-p_{ad}, u^{\perp}_{ad,acd}\rangle] \\ & \langle p-p_{bcd}, u^{\perp}_{bcd}\rangle[\langle p-p_{bc}, u^{\perp}_{bc,bcd}\rangle + \langle p-p_{cd}, u^{\perp}_{cd,bcd}\rangle + \langle p-p_{bd}, u^{\perp}_{bd,bcd}\rangle]\} \end{aligned} \tag{4.4}$$

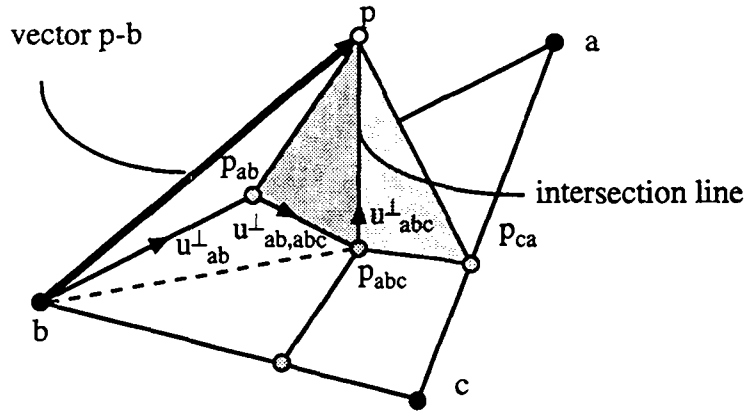

Figure 4.2: Vector $p - b$ and its projections.

As triangle $p_{ab}p_{abc}p$ is perpendicular to vector ab (see Figure 4.2), l_2 and l_3 points can be eliminated from Equation 4.4 as follows.

$$\begin{aligned}\langle p - p_{abc}, u^{\perp}_{abc}\rangle &= \langle p - (b + \langle p - b, \frac{p_{abc} - b}{|p_{abc} - b|}\rangle \frac{p_{abc} - b}{|p_{abc} - b|}), u^{\perp}_{abc}\rangle \\ &= \langle (p - b) - \langle p - b, \frac{p_{abc} - b}{|p_{abc} - b|}\rangle \frac{p_{abc} - b}{|p_{abc} - b|}, u^{\perp}_{abc}\rangle \\ &= \langle p - b, u^{\perp}_{abc}\rangle \end{aligned} \tag{4.5}$$

and

$$\langle p - p_{ab}, u^{\perp}_{ab,abc}\rangle = \langle p - (b + \langle p - b, u_{ab}\rangle u_{ab}), u^{\perp}_{ab,abc}\rangle = \langle p - b, u^{\perp}_{ab,abc}\rangle \tag{4.6}$$

Substituting Equations 4.5 and 4.6 into 4.4, p_{abc} and p_{ab} are thus replaced by b. Other l_2 and l_3 points can be replaced in the same way. Finally, the area of local Laguerre facets comes to

$$\begin{aligned} A_p = \frac{1}{2}\{&\langle p - b, u^{\perp}_{abc}\rangle[\langle p - b, u^{\perp}_{ab,abc}\rangle + \langle p - b, u^{\perp}_{bc,abc}\rangle + \langle p - c, u^{\perp}_{ac,abc}\rangle] \\ &\langle p - b, u^{\perp}_{abd}\rangle[\langle p - b, u^{\perp}_{ab,abd}\rangle + \langle p - b, u^{\perp}_{bd,abd}\rangle + \langle p - c, u^{\perp}_{ad,abd}\rangle] \\ &\langle p - c, u^{\perp}_{acd}\rangle[\langle p - c, u^{\perp}_{ac,acd}\rangle + \langle p - c, u^{\perp}_{cd,acd}\rangle + \langle p - d, u^{\perp}_{ad,acd}\rangle] \\ &\langle p - b, u^{\perp}_{bcd}\rangle[\langle p - b, u^{\perp}_{bc,bcd}\rangle + \langle p - c, u^{\perp}_{cd,bcd}\rangle + \langle p - d, u^{\perp}_{bd,bcd}\rangle]\} \end{aligned} \tag{4.7}$$

In [Tel89a], scalar product $\langle p - b, u^{\perp}_{abc}\rangle$ is called the algebraic distance from p to b with respect to the direction $u^{\perp}_{abc}$.

In Equation 4.7, the area of local Laguerre facet is presented by a series of scalar products which are signed areas. Some signed area would be negative if l_2, l_3 points or Laguerre vertex are out the tetrahedron. For instance, in Figure 4.3, as $\langle p - b, u^{\perp}_{abc}\rangle < 0$ and $\langle p - b, u^{\perp}_{bc,bcd}\rangle < 0$, the area of quadrilateral $p_{abc}p_{bc}p_{bcd}p$ is negative by Equation 4.7. Even in this case, Equation 4.7 can still correctly calculate the area of an entire Laguerre facet. In fact, the following corollary comes from Property 3.2.

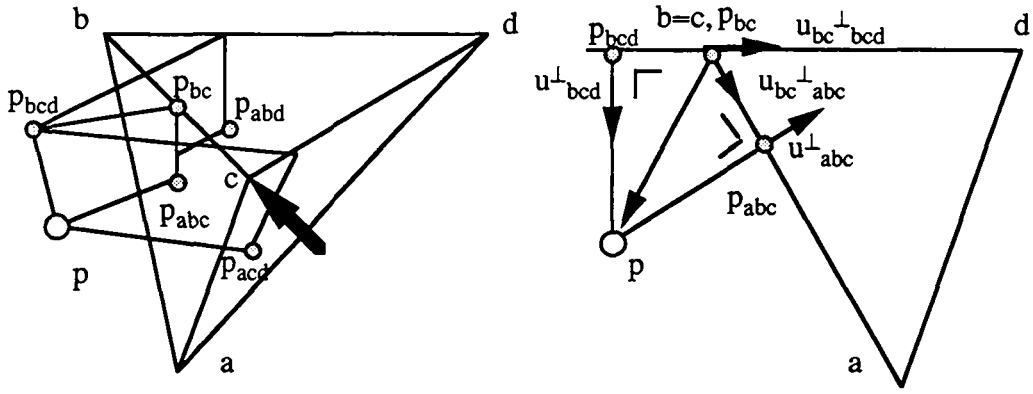

(a) p and p_{bcd} are out of the tetrahedron (b) some signed facet area are negative

Figure 4.3: Description of arbitrary position of p.

Corollary 4.1 *Let Laguerre facet ϖ_{ab} be the dual of Delaunay edge e_{ab}. Also let e_{ab} be incident to n Delaunay cells. Then the area of the Laguerre facet is distributed in the n Delaunay cells.*

Proof: From Property 3.2, "a Laguerre facet possesses n extreme points" is equivalent to say "the facet is incident to n Delaunay cells". The n Delaunay cells possess a common edge, i.e., edge e_{ab}. The Laguerre facet, noted as ϖ_{ab}, is perpendicular to the edge. While in each of the cells there exist other five Laguerre facets intersecting ϖ_{ab}. Considering all the n incident Delaunay cells, Laguerre facet ϖ_{ab} then intersects $3n$ Laguerre facets at its boundary. Thus the area of the facet is distributed in the n Delaunay cells. □

Equation 4.7 is demonstrated by an example as below. Without loss of generality, suppose a Laguerre facet has three extreme points, p_1, p_2 and p_3 which are Laguerre vertices of tetrahedra T_1, T_2 and T_3, respectively (Figure 4.4). As edge ab is shared by the three tetrahedra, the three Laguerre vertices are the apices of ϖ_{ab}. Since Laguerre facet ϖ_{ab} intersects Laguerre facets perpendicular to edges bc, bd, be, ac, ad, ae, cd, de and ce at its boundary, the projection point of p_2 (p_3) on plane π_{abc} (π_{abd}) coincides with that of p_1 on the same plane (see Figure 4.4(b)). The point-line-plane relation is illustrated in Figure 4.4(c), where $u^{\perp}_{ab\,abc,1}$ is a unit vector perpendicular to edge ab in triangle abc and belongs to tetrahedron T_1. Considering the orientation of normal vectors (Definitions 4.1 and 4.2), six triangles' areas can be calculated by Equation 4.7. The results are summarized in Table 4.1. Because all the portions of the facet have been included in the calculation and the negative portions have been offset by the positive ones, one eventually obtains the area of the facet composed of two triangles: H and I.

From this example, it is apparent that the local interfacial area of Laguerre diagram defined in Equation 4.2 is computable by applying Equation 4.7 to every Delaunay cell in $D(S')$. In turn, the interfacial area of Laguerre diagram $L(S')$ defined by Equation 4.1 is computable as well.

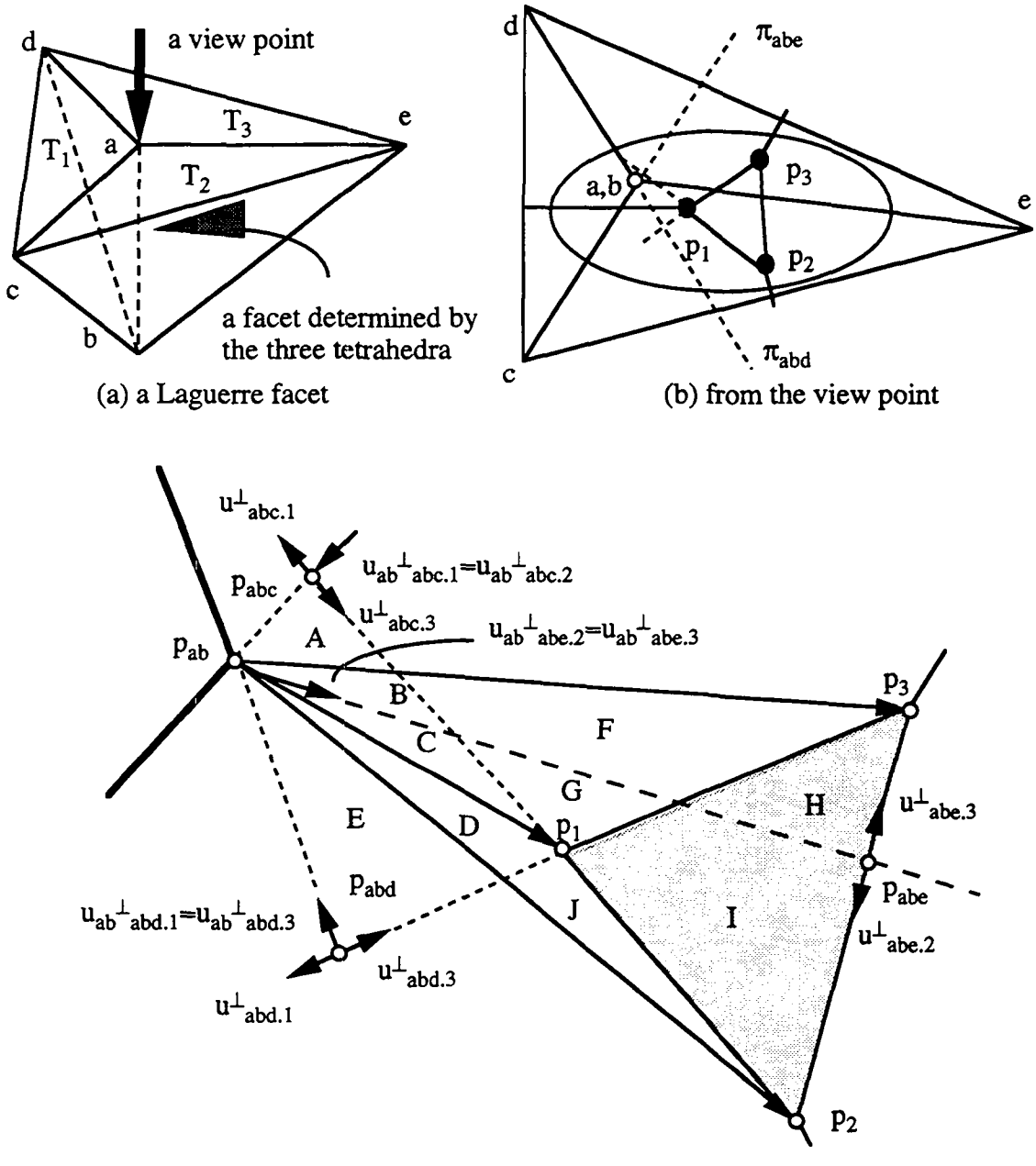

Figure 4.4: Laguerre vertex and l_3 points are out of tetrahedron T_1.

	A	B	C	D	E	F	G	H	I	J
$p_1p_{ab}p_{abc}$	+	+	+							
$p_1p_{ab}p_{abd}$				+	+					
$p_2p_{ab}p_{abe}$			+	+			+		+	+
$p_2p_{ab}p_{abc}$	−	−	−	−						−
$p_3p_{ab}p_{abe}$		+				+		+		
$p_3p_{ab}p_{abd}$		−	−	−	−	−	−			
Σ								+	+	

Table 4.1: Laguerre facet $p_1p_2p_3$ in Delaunay cells T_1, T_2 and T_3

From Equation 2.4, the total interfacial energy in a Laguerre diagram amounts to

$$E = \frac{1}{2}\sum_i \sum_j \gamma_{ij} A_{ij} \tag{4.8}$$

where γ_{ij} is the specific Laguerre facet energy. In the isotropic case, γ_{ij} is a constant for all i and j, while in the anisotropic case it depends on the crystallography and microstructure of the simulated material.

The local interfacial energy in a Delaunay tetrahedron, say (a, b, c, d) as shown in Figure 4.1 is given by

$$E_p = \sum_{k=1}^{6} \gamma_k A_k(p) \tag{4.9}$$

Equation 4.8 means that the interfacial energy of a Laguerre diagram is proportional to its total interfacial area. Moreover, the local interfacial energy in a Delaunay cell is proportional to the local interfacial area, as indicated in Equation 4.9. Substituting Equation 4.7 into 4.9, the local interfacial energy comes to

$$\begin{aligned} E_p &= \frac{1}{2}\{\langle p-b, u^{\perp}_{abc}\rangle[\gamma_{ab}\langle p-b, u^{\perp}_{ab,abc}\rangle + \gamma_{bc}\langle p-b, u^{\perp}_{bc,abc}\rangle + \gamma_{ac}\langle p-c, u^{\perp}_{ac,abc}\rangle] \\ &\quad \langle p-b, u^{\perp}_{abd}\rangle[\gamma_{ab}\langle p-b, u^{\perp}_{ab,abd}\rangle + \gamma_{bd}\langle p-b, u^{\perp}_{bd,abd}\rangle + \gamma_{ad}\langle p-d, u^{\perp}_{ad,abd}\rangle] \\ &\quad \langle p-c, u^{\perp}_{acd}\rangle[\gamma_{ac}\langle p-c, u^{\perp}_{ac,acd}\rangle + \gamma_{cd}\langle p-c, u^{\perp}_{cd,acd}\rangle + \gamma_{ad}\langle p-d, u^{\perp}_{ad,acd}\rangle] \\ &\quad \langle p-b, u^{\perp}_{bcd}\rangle[\gamma_{bc}\langle p-b, u^{\perp}_{bc,bcd}\rangle + \gamma_{cd}\langle p-c, u^{\perp}_{cd,bcd}\rangle + \gamma_{bd}\langle p-d, u^{\perp}_{bd,bcd}\rangle]\} \\ &= \frac{1}{2}\{\langle p-b, u^{\perp}_{abc}\rangle l_{abc} + \langle p-b, u^{\perp}_{abd}\rangle l_{abd} \\ &\quad + \langle p-c, u^{\perp}_{acd}\rangle l_{acd} + \langle p-b, u^{\perp}_{bcd}\rangle l_{bcd}\} \end{aligned} \tag{4.10}$$

with

$$\begin{cases} l_{abc} = \gamma_{ab}\langle p-b, u^{\perp}_{ab,abc}\rangle + \gamma_{bc}\langle p-b, u^{\perp}_{bc,abc}\rangle + \gamma_{ac}\langle p-c, u^{\perp}_{ac,abc}\rangle \\ l_{abd} = \gamma_{ab}\langle p-b, u^{\perp}_{ab,abd}\rangle + \gamma_{bd}\langle p-b, u^{\perp}_{bd,abd}\rangle + \gamma_{ad}\langle p-d, u^{\perp}_{ad,abd}\rangle \\ l_{acd} = \gamma_{ac}\langle p-c, u^{\perp}_{ac,acd}\rangle + \gamma_{cd}\langle p-c, u^{\perp}_{cd,acd}\rangle + \gamma_{ad}\langle p-d, u^{\perp}_{ad,acd}\rangle \\ l_{bcd} = \gamma_{bc}\langle p-b, u^{\perp}_{bc,bcd}\rangle + \gamma_{cd}\langle p-c, u^{\perp}_{cd,bcd}\rangle + \gamma_{bd}\langle p-d, u^{\perp}_{bd,bcd}\rangle \end{cases} \tag{4.11}$$

where γ_{ab} is the specific facet energy between cell a and b. The site motion equation will be derived from Equation 4.10 in next subsection.

4.1.2 Derivation of motion equation

As indicated in Chapter 2, normal grain growth is the process in which the interfacial energy continuously decreases. Suppose the energy is proportional to the interfacial area, then in the process in every Laguerre facet there will exist a surface tension which tends to decrease the area of the facet. On the other hand, each Laguerre vertex connects to six facets and the vertex will be forced to a place where the tensions are released and hence the interfacial energy is minimized. From the principle of virtual work, the driving force associated with Laguerre vertex p that tends to minimize the interfacial energy is opposed to the energy gradient and is given by

$$F_p = -\nabla_p E_p \tag{4.12}$$

For given position of the four apices a, b, c, d of the tetrahedron, from Equations 4.10 and 4.11, F_p can be written as

$$\begin{aligned} F_p \;=\; & -\frac{1}{2}\{\langle p-b, u^{\perp}_{abc}\rangle T_{abc} + \langle p-b, u^{\perp}_{abd}\rangle T_{abd} + \langle p-c, u^{\perp}_{acd}\rangle T_{acd} + \langle p-b, u^{\perp}_{bcd}\rangle T_{bcd} + \\ & l_{abc}u^{\perp}_{abc} + l_{abd}u^{\perp}_{abd} + l_{acd}u^{\perp}_{acd} + l_{bcd}u^{\perp}_{bcd}\} \end{aligned} \tag{4.13}$$

with

$$\begin{cases} T_{abc} = \gamma_{ab}u^{\perp}_{ab,abc} + \gamma_{bc}u^{\perp}_{bc,abc} + \gamma_{ac}u^{\perp}_{ac,abc} \\ T_{abd} = \gamma_{ab}u^{\perp}_{ab,abd} + \gamma_{bd}u^{\perp}_{bd,abd} + \gamma_{ad}u^{\perp}_{ad,abd} \\ T_{acd} = \gamma_{ac}u^{\perp}_{ac,acd} + \gamma_{cd}u^{\perp}_{cd,acd} + \gamma_{ad}u^{\perp}_{ad,acd} \\ T_{bcd} = \gamma_{bc}u^{\perp}_{bc,bcd} + \gamma_{cd}u^{\perp}_{cd,bcd} + \gamma_{bd}u^{\perp}_{bd,bcd} \end{cases} \tag{4.14}$$

Suppose point p is Laguerre vertex of Laguerre cell $L(a')$, still from the principle of virtual work, the driving force exerted on the site due to the reduction of interfacial energy at point p is given by

$$F_{a'(p)} = -\nabla_{a'} E_p \tag{4.15}$$

Considering p as a function of a', i.e., $p = [p_1(a')\ p_2(a')\ p_3(a')]^t$, the gradient of E_p comes to

$$\nabla_{a'}E_p = \begin{bmatrix} \frac{\partial E_p \partial p_1}{\partial p_1 \partial a_1} + \frac{\partial E_p \partial p_2}{\partial p_2 \partial a_1} + \frac{\partial E_p \partial p_3}{\partial p_3 \partial a_1} \\ \frac{\partial E_p \partial p_1}{\partial p_1 \partial a_2} + \frac{\partial E_p \partial p_2}{\partial p_2 \partial a_2} + \frac{\partial E_p \partial p_3}{\partial p_3 \partial a_2} \\ \frac{\partial E_p \partial p_1}{\partial p_1 \partial a_3} + \frac{\partial E_p \partial p_2}{\partial p_2 \partial a_3} + \frac{\partial E_p \partial p_3}{\partial p_3 \partial a_3} \\ \frac{\partial E_p \partial p_1}{\partial p_1 \partial r_a} + \frac{\partial E_p \partial p_2}{\partial p_2 \partial r_a} + \frac{\partial E_p \partial p_3}{\partial p_3 \partial r_a} \end{bmatrix} = \begin{bmatrix} \langle \nabla_p E_p, \frac{\partial p}{\partial a_1} \rangle \\ \langle \nabla_p E_p, \frac{\partial p}{\partial a_2} \rangle \\ \langle \nabla_p E_p, \frac{\partial p}{\partial a_3} \rangle \\ \langle \nabla_p E_p, \frac{\partial p}{\partial r_a} \rangle \end{bmatrix}$$

To simplify formulation, the following coordinate system is employed (see Figure 4.5)

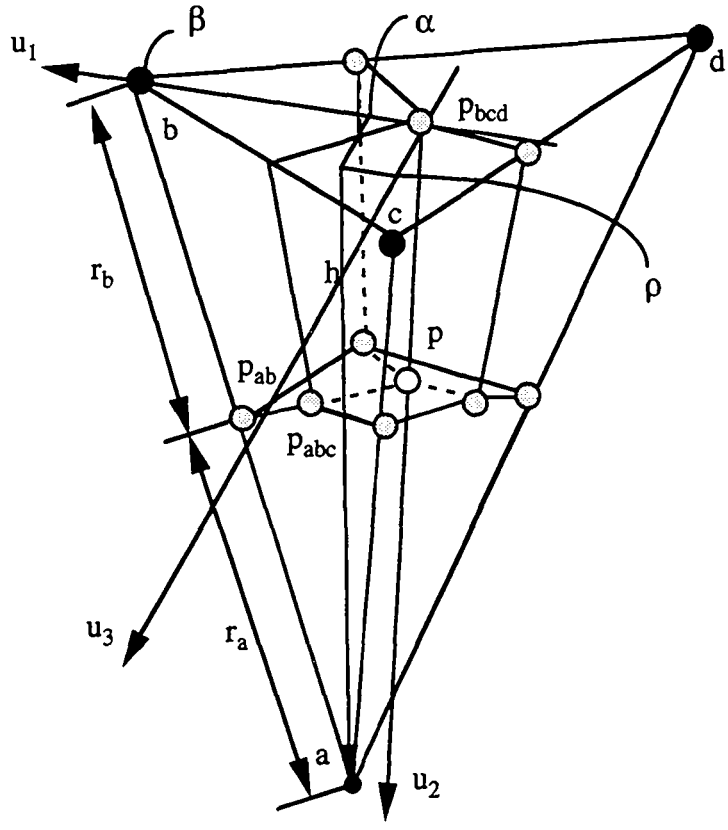

Figure 4.5: Driving force exerted on a weighted site.

$$(p_{bcd}, \frac{b - p_{bcd}}{|b - p_{bcd}|}, u^{\perp}_{bcd}, \frac{b - p_{bcd}}{|b - p_{bcd}|} \times u^{\perp}_{bcd}) = (0, u_1, u_2, u_3)$$

for representing the geometry of a Delaunay cell in 3D and $(0, u_1, u_2, u_3, u_4)$ for the weighted one. Points b', c' and d' are supposed to be fixed. Evidently, in the system $p_1 = p_2 = 0$. So,

$$\nabla_{a'} E_p = \begin{bmatrix} \frac{\partial E_p \partial p_3}{\partial p_3 \partial a_1} \\ \frac{\partial E_p \partial p_3}{\partial p_3 \partial a_2} \\ \frac{\partial E_p \partial p_3}{\partial p_3 \partial a_3} \\ \frac{\partial E_p \partial p_3}{\partial p_3 \partial r_a} \end{bmatrix} = \begin{bmatrix} \langle \nabla_p E_p, u^{\perp}_{bcd} \rangle \frac{\partial p}{\partial a_1} \\ \langle \nabla_p E_p, u^{\perp}_{bcd} \rangle \frac{\partial p}{\partial a_2} \\ \langle \nabla_p E_p, u^{\perp}_{bcd} \rangle \frac{\partial p}{\partial a_3} \\ \langle \nabla_p E_p, u^{\perp}_{bcd} \rangle \frac{\partial p}{\partial r_a} \end{bmatrix} = \langle \nabla_p E_p, u^{\perp}_{bcd} \rangle \begin{bmatrix} \frac{\partial p}{\partial a_1} \\ \frac{\partial p}{\partial a_2} \\ \frac{\partial p}{\partial a_3} \\ \frac{\partial p}{\partial r_a} \end{bmatrix} \tag{4.16}$$

Substituting Equations 4.12 and 4.16 into 4.15, one has

$$F_{a'(p)} = \langle F_p, u^{\perp}_{bcd} \rangle \nabla_{a'} p \tag{4.17}$$

Suppose m is the distance from reference point p_{bcd} to point p and h is the height of the tetrahedron (in direction of $u_{bcd}^{\perp}$), that is

$$h = \langle a - b, u_{bcd}^{\perp} \rangle \tag{4.18}$$

Since

$$p = p_{bcd} + m u_{bcd}^{\perp} = p_{ab} + (p - p_{ab}) \frac{p - p_{ab}}{|p - p_{ab}|}. \tag{4.19}$$

Projecting the expression on u_{ab}:

$$\langle p, u_{ab} \rangle = \langle p_{bcd}, u_{ab} \rangle + m \langle u_{bcd}^{\perp}, u_{ab} \rangle = \langle p_{ab}, u_{ab} \rangle + \langle (p - p_{ab}) \frac{p - p_{ab}}{|p - p_{ab}|}, u_{ab} \rangle = \langle p_{ab}, u_{ab} \rangle$$

From this expression m comes to

$$m = \frac{\langle p_{ab}, u_{ab} \rangle - \langle p_{bcd}, u_{ab} \rangle}{\langle u_{bcd}^{\perp}, u_{ab} \rangle} = \frac{\langle p_{ab} - p_{bcd}, a - b \rangle}{\langle u_{bcd}^{\perp}, a - b \rangle} = \frac{1}{h} \langle p_{ab} - p_{bcd}, a - b \rangle \tag{4.20}$$

As point p_{ab} is the median of Delaunay edge $a'b'$ and satisfies Equation 3.13, in the system

$$\begin{cases} p_{bcd} = (0, 0, 0) \\ b = (\beta, 0, 0) \\ a = (\alpha, h, \rho) \\ p_{ab} = (\beta + \lambda(\alpha - \beta), \lambda h, \lambda \rho) \end{cases}$$

Suppose $d = |a - b|$, that is $d^2 = (\alpha - \beta)^2 + h^2 + \rho^2$, substituting these expressions for p_{ab}, p_{bcd}, a and b in Equation 4.20, m is given by

$$m = \frac{1}{h} \langle \begin{bmatrix} \beta + \lambda(\alpha - \beta) \\ \lambda h \\ \lambda \rho \end{bmatrix}, \begin{bmatrix} \alpha - \beta \\ h \\ \rho \end{bmatrix} \rangle = \frac{1}{h} (\alpha\beta - \beta^2 + \lambda d^2) = \frac{\alpha^2 - \beta^2 + h^2 + \rho^2 - r_a^2 + r_b^2}{2h} \tag{4.21}$$

From Equations 4.19 and 4.21,

$$\nabla_{a'} p = \nabla_{a'} m = \frac{1}{h} \begin{bmatrix} \alpha & h - m & \rho & -r_a \end{bmatrix}^t \tag{4.22}$$

Considering in the system

$$a - p = \begin{bmatrix} \alpha & h - m & \rho \end{bmatrix}^t$$

Finally, the driving force exerted on Laguerre vertex p is transformed to its supporting site a' as

$$F_{a'(p)} = \frac{1}{h} \langle F_p, u_{bcd}^{\perp} \rangle \begin{bmatrix} a - p \\ -r_a \end{bmatrix} \tag{4.23}$$

The driving force $F_{a'}$ associated with site a' is the vector sum of its Laguerre vertices' contributions.

Under driving force $F_{a'}$, site a' will move. To obtain a concise site motion equation, the following assumption is made.

Assumption 5 *In order to simulate the grain growth process in polycrystals, the motion of the Laguerre diagram $L(S')$ is such that*

(i) The Laguerre diagram is a pure dissipative system, i.e.,

$$\ddot{a}' = 0, \forall a' \in S'. \tag{4.24}$$

(ii) The friction is isotropic in the system.

(iii) Each Laguerre cell moves as a whole.

(iv) The velocity of cell a' noted as $\dot{a}' = (\dot{a}, \dot{r}_a)$ is parallel to the driving force $F_{a'} = (F_a, F_{r_a})$.

From classical mechanics [Gol69] and Assumption 5(i) and (ii), driving force F_a will be balanced by frictional force

$$F_a^f = \rho \mathcal{A}_a \dot{a} \tag{4.25}$$

in the displacement direction and F_{r_a} will be balanced by frictional force

$$F_{r_a}^f = \rho \mathcal{A}_{r_a} \dot{r}_a \tag{4.26}$$

in the radial direction, where ρ is the frictional coefficient. From Assumption 5(iii) and (iv), frictional area $\mathcal{A}_a$ is the projection area of Laguerre cell $L(a')$ on the direction of F_a^f, i.e.,

$$\mathcal{A}_a = \frac{1}{2} \sum_j |\langle A_j, \frac{F_a}{|F_a|} \rangle| \tag{4.27}$$

where A_j is the area of a Laguerre facet and $\sum_j$ over the facets of cell $L(a')$. While $\mathcal{A}_{r_a}$ is the surface area of an equivalent sphere with the same volume as cell $L(a')$. We call $\mathcal{A}_{a'} = (\mathcal{A}_a, \mathcal{A}_{r_a})$ the Plateau area of the cell in its motion direction. Finally the velocity of site a' comes to

$$\begin{cases} \dot{a} = \dfrac{\sum_p \frac{1}{h} \langle F_p, u_{bcd}^{\perp} \rangle (a - p)}{\rho \mathcal{A}_a} \\ \dot{r}_a = -\dfrac{\sum_p \frac{r_a}{h} \langle F_p, u_{bcd}^{\perp} \rangle}{\rho \mathcal{A}_{r_a}} \end{cases} \tag{4.28}$$

where $\sum_p$ is over Laguerre vertices of the cell. Assumption 5 is an enormous simplifying hypothesis. Its rationality will be further investigated by simulation.

Since the cell mobility M may be written as $1/\rho$ and the pressure exerted on the cell, noted as $P_{a'} = (P_a, P_{r_a})$ amounts to $P_a = F_a/\mathcal{A}_a$ and $P_{r_a} = F_{r_a}/\mathcal{A}_{r_a}$, Equation 4.28 can be written as

$$\begin{cases} \dot{a} = M P_a \\ \dot{r}_a = M P_{r_a} \end{cases} \tag{4.29}$$

Now it is clear that the motion equation of Laguerre diagram, i.e., Equation 4.28 is nothing else but Burke and Turnbull's grain boundary migration equation (Equation 2.5) applied in Laguerre diagram.

We have derived the motion equation of weighted site of Laguerre diagram which is supposed in normal motion. The diagram will be used to simulate normal grain growth process in polycrystalline materials. As Laguerre vertex p can be determined by weighted sites as described in Equation 3.13, the only free variables in the motion equation are weighted sites. By the equation, the velocity of weighted site set S' can be analytically determined, for which it is called the motion equation of Laguerre diagram. A corresponding algorithm will be given in next subsection.

4.1.3 Algorithm for the velocity of site

Since each Delaunay cell is incident to four weighted sites and corresponds to a Laguerre vertex, once the driving force exerted on a Laguerre vertex is known, its contribution to the four sites can be obtained by appropriate changes of indices and projection direction in Equation 4.28. Based on this idea, we propose an algorithm, called *Gradient* which goes through all Delaunay cells, calculates F_p for each cell and projects F_p to the four sites. So, this algorithm is tetrahedron-based. The input of the algorithm is the Laguerre and weighted Delaunay diagrams. i.e., $L(S')$ and $D(S')$ and the output is the velocity of S' noted as $\dot{S}'$.

algorithm *Gradient* ($L(S')$, $D(S')$, $\dot{S}'$);
begin
  Initialize $\dot{S}'$ to zero;
  for each Delaunay cell, say $(abcd)$ with Laguerre vertex p **do**
    Calculate F_p;
    Calculate the contribution to the four sites:
    $\dot{a}' := \dot{a}' + \langle F_p, u^{\perp}_{bcd} \rangle \frac{1}{h_{bcd}} \begin{bmatrix} a-p \\ -r_a \end{bmatrix}$;
    ($\dot{b}'$, $\dot{c}'$ and $\dot{d}'$ can be updated by appropriate projections)
  endfor;
  for each site, say a' **do**
    Calculate the Plateau area $\mathcal{A}'_a = (\mathcal{A}_a, \mathcal{A}_{r_a})$;
    $\dot{a} := \frac{\dot{a}}{\rho \mathcal{A}_a}$; $\dot{r}_a := \frac{\dot{r}_a}{\rho \mathcal{A}_{r_a}}$;
  endfor;
end.

It is clear to calculate the velocity of sites, both of Laguerre and weighted Delaunay diagrams are needed. As the two for-loops in the algorithm need $O(N^2)$ time to complete, algorithm *Gradient* requires $O(N^2)$ time to compute $\dot{S}'$.

4.2 Simulation protocol

Based on the dynamic Laguerre diagram presented in Chapter 3 and the weighted site motion equation derived in previous section, the normal grain growth simulation is first carried out in the isotropic case, i.e., in the Laguerre diagram all facets have the same specific energy ($\gamma = 1$) and mobility ($\rho = 1$) and then in the anisotropic case, i.e., the specific facet energy is determined by the misorientation of adjacent cells and the cell mobility is isotropic ($\rho = 1$). In this section we discuss the simulation protocol which is composed of four parts: the simulation scheme that is an application of *Growth* algorithm proposed in Chapter 3, the calculation of misorientation in the anisotropic case, the statistical measurements that will be carried out in simulations and the initial Laguerre diagram produced by a recrystallization algorithm [Rig92].

4.2.1 Simulation scheme

The Laguerre simulation of normal grain growth starts from an initial Laguerre diagram. More precisely, it starts from a set S'^0 of N_3^0 weighted sites in $\mathbb{T}^3$, whose Laguerre diagram $L(S'^0)$ is first constructed. Notice that in S' each weighted site, say $a' = (a_1, a_2, a_3, a_4)$ and $a_4 = r_a^2$, the velocity of the site weight then amounts to

$$\dot{a}_4 = 2r_a\dot{r}_a \tag{4.30}$$

Thereafter in each simulation step, that is $S'^k \rightarrow S'^{k+1}$ we do:

(1) Compute the velocity $\dot{a}' = (\dot{a}, \dot{r}_a)$, $\forall a' \in S'^k$ by *Gradient*.

(2) Deduce the linear motion of $a'(\tau)$ for each site of S'^k as a linear approximated solution of the motion equation,

$$a'(\tau) = \begin{bmatrix} a \\ a_4 \end{bmatrix} + \tau\delta_k \begin{bmatrix} \mu\dot{a} \\ (1-\mu)\dot{a}_4 \end{bmatrix} \tag{4.31}$$

(3) Perform every linear motion $a'(\tau)$, $0 \leq \tau \leq 1$, simultaneously by *Motion* algorithm that delivers a new weighted set S'^{k+1} and its Laguerre diagram $L(S'^{k+1})$.

In the procedure, δ_k stands for the time interval of this simulation step,

$$\delta_k = \Delta / N_3^k \tag{4.32}$$

where Δ is a constant, called precision parameter. As N_3^k is the number of cells in current cell complex, by Equation 4.32, δ_k is proportional to the average cell size. Using this formula is an improvement over using a fixed step length, as accuracy is enhanced on the average over the simulation. At the end of the k-step ($\tau = 1$), the simulation time has been accumulated to

$$t = \sum_k \delta_k \tag{4.33}$$

In the simulation procedure, μ is a constant, $0 \leq \mu \leq 1$. If $\mu = 0$, the position of the site is fixed. If $\mu = 1$, then the site weight is fixed. While for $0 < \mu < 1$, normal motion is allowed. In the isotropic simulation, parameter μ is to emulate the cell's directional growth, which was proposed by Telley [Tel89a]. In the anisotropic case, $\mu \equiv 0.5$, for highlighting the effect of anisotropic grain boundary energy.

Precision parameter Δ should be chosen sufficiently small for discretization precision of motion equation and meanwhile sufficiently large for computational cost, while μ should be well chosen to reproduce a grain growth process as realistic as possible. In our simulation, Δ is chosen as large as possible provided the mean cell area in a cross-section plane linearly increases with time thereby satisfies the grain growth power law. The influence of μ ranging from 0.25 to 0.75 has been studied through simulations. All simulations were stopped when 10% initial cells remained. As the initial Laguerre diagrams are with several thousand cells and final ones still contain several hundred cells, one can therefore be quite confident with the simulation results. The distribution of cell size and shape in two-dimensional cross-section plane is observed in a cross-section plane along the x_3-axis.

4.2.2 Consideration of anisotropy

The anisotropic grain growth is a quite complicated problem, as many factors could lead to anisotropy [Cot76]. To date, the phenomenon has been simulated in 2D by Anderson, Srolovitz, Grest and Sahni [And84] and by Kunaver and Kolar [Kun93] with the pseudo-atomic Potts model and by Kawasaki, Nagai, Okuzono and Fuchizaki with the vertex model [Kaw93] under different simplifying assumptions. In our anisotropic growth simulation, Gottstein and Schwarzer's assumption is adapted [Got92], i.e., the specific grain boundary energy is determined by the misorientation of adjacent grains and the grain boundary mobility is supposed to be isotropic. To compute the velocities of sites by the procedure presented in previous subsection, the unsolved problem is how to determine the specific Laguerre facet energy γ_{ij}. In this subsection an approximation approach is proposed.

Suppose the simulated material is a simple cubic system, the orientation of grain i is represented by a 3×3 orientation matrix

$$\sigma(i) = [\sigma_1(i)\, \sigma_2(i)\, \sigma_3(i)] \tag{4.34}$$

which specifies the grain crystal axes 100, 010 and 001 by the direction cosines with respect to the specimen (reference) axes. The misorientation of two adjacent grains, say i and j, is then defined by the three angles θ_{ij}^k, $k = 1, 2, 3$, between their respective orientation vectors $\sigma_k(i)$ and $\sigma_k(j)$. Owing to the symmetry of the cubic system, $0 \leq \theta_{ij}^k \leq \pi/2$, for $k = 1, 2, 3$ (See Figure 4.6).

The crystallography of a planar grain boundary between adjacent grain i and j in the simple cubic system can be specified by the misorientation of the grains (three parameters: θ_{ij}^k, $k = 1, 2, 3$) and the inclination of the grain boundary plane (two parameters: ϕ and ψ are the inclination angles with respect to the crystal axes of grain i). The specific grain

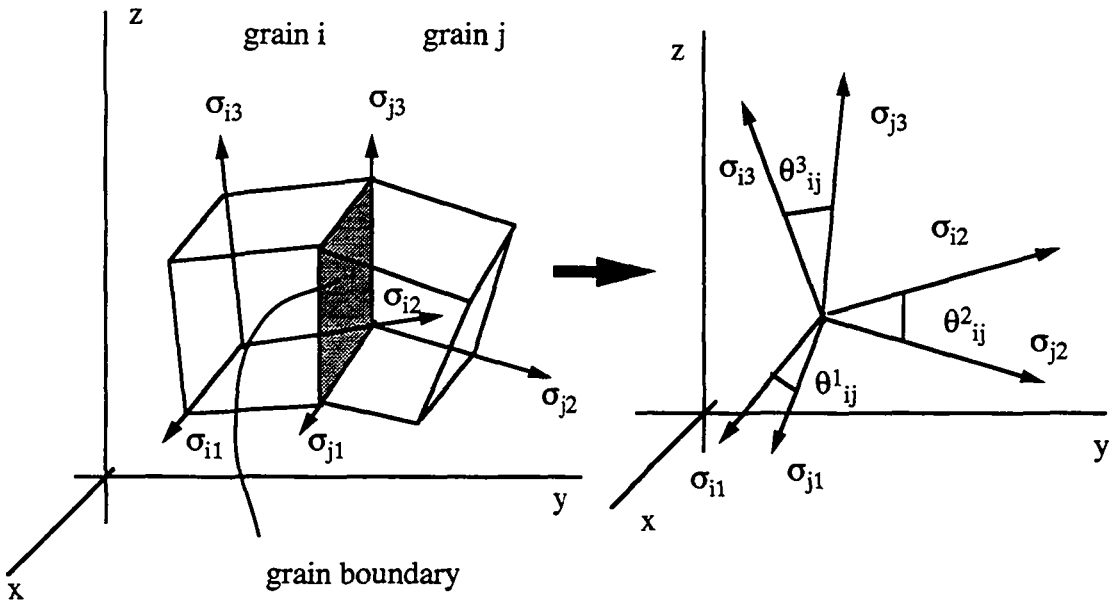

Figure 4.6: Crystal axes in cubic system and grain boundary misorientation.

boundary energy is given by a function

$$\gamma_{ij} = \gamma(\theta^1_{ij}, \theta^2_{ij}, \theta^3_{ij}, \phi, \psi, p_i, p_e) \tag{4.35}$$

where, p_i is the internal variable of the simulated material like composition and defects and so on, and p_e is the external variable like temperature and pressure. Suppose p_i and p_e are constant in our simulation, then

$$\gamma_{ij} = \gamma(\theta^1_{ij}, \theta^2_{ij}, \theta^3_{ij}, \phi, \psi) \tag{4.36}$$

If the inclination of boundary plane is neglected, the specific grain boundary energy is then determined by the misorientation, viz

$$\gamma_{ij} = \gamma(\theta^1_{ij}, \theta^2_{ij}, \theta^3_{ij}) \tag{4.37}$$

As a further approximation, we suppose that

$$\gamma_{ij} = \max\{\gamma(\theta^k_{ij}) : k = 1, 2, 3\} \tag{4.38}$$

and corresponding angle is noted as θ_{ij}. Therefore, in our model, the grain boundary misorientation is characterized by a single parameter θ_{ij} which is assumed to represent the corresponding grain boundary energy.

Thus it becomes easy to determine the specific grain boundary energy, provided the misorientation degrees and the dependence of grain boundary energy on misorientation degree are known. To date, the knowledge about the dependence of grain boundary energy, γ on misorientation degree, θ is still very limited. In our simulation, a typical

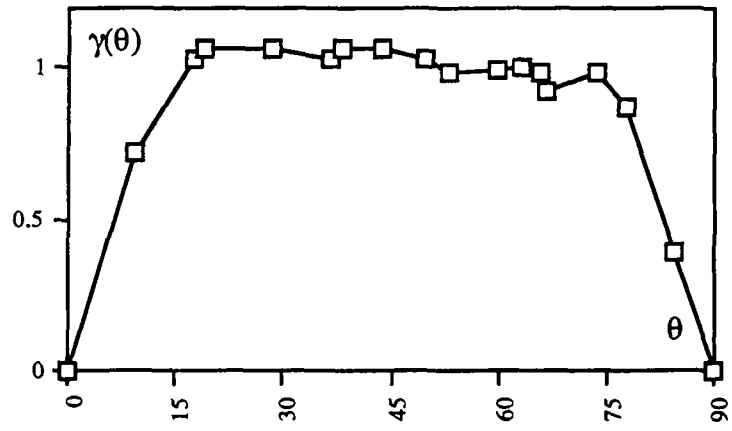

Figure 4.7: A typical $\gamma(\theta)$ plot for cubic system (from [Has71]).

$\gamma(\theta)$ plot [Has71] as shown in Figure 4.7 is applied. Even though $\gamma(\theta)$ values are only available for certain materials, it is reasonable to assume that small angle grain boundary has low grain boundary energy and large angle one has high grain boundary energy as observed. On the other hand, the misorientation degree of adjacent cells, say cell i and j has been defined as a single parameter θ_{ij} and $\theta_{ij} \in [0, \pi/2]$, as an approximation, θ is replaced by θ_{ij} in the $\gamma(\theta)$ plot. Hence, the specific facet energy γ_{ij} can be obtained from the plot, provided θ_{ij} is known.

In the anisotropic simulation, apart from the coordinate and weight, each site is tagged with a random orientation. For instance, site $a' \in S'$ is tagged with an orientation matrix $[\sigma_1(a), \sigma_2(a), \sigma_3(a)]$, where unit vectors $\sigma_1(a)$, $\sigma_2(a)$and $\sigma_3(a)$ are mutually orthogonal and fixed during the cell lifetime.

Now that the specific Laguerre facet energy γ_{ij} can be obtained as above, each weighted site's velocity can be analytically determined by the motion equation of Laguerre diagram.

4.2.3 Definition of measurements

In each simulation step, the following nine tests are carried out. Based on these tests, the cell growth kinetics and the cell size and shape distribution of the dynamic Laguerre diagram are analyzed.

(1) t – simulation time as defined in Equation 4.33.

(2) N_2^t – the number of cells which appear in a given cross-section plane at time t.

(3) $A_i(t)$ – the area of cell i which appears in a given cross-section plane at time t.

(4) $n_i(t)$ – the number of sides (or corners, edges) of cell i which appears in a given cross-section plane at time t.

(5) $e_i(t)$ – the eccentricity of cell i which appears in a given cross-section plane at time t. Suppose α_i and β_i are the length of the major and minor axes of its fitting ellipse, the eccentricity of the cell is defined as[1]

$$e_i = \sqrt{1 - \beta_i^2/\alpha_i^2} \tag{4.39}$$

(6) N_3^t – the number of cells in current Laguerre diagram.

(7) $v_i(t)$ – the volume of cell i in current Laguerre diagram.

(8) $m_i(t)$ – the number of facets of cell i in current Laguerre diagram.

(9) $\theta_{ij}(t)$ – the misorientation degree between cell i and j in current Laguerre diagram.

From the data of N_2^t, the cell growth rate in 2D can be verified as follows. Notice that a cross-section plane of $\mathbb{T}^3$ along x_3-axis is a 2D torus, thus at any time

$$\sum_i A_i = 1 \tag{4.40}$$

The mean cell area in the cross-section plane is given by

$$A^t = 1/N_2^t \tag{4.41}$$

Denoting the mean cell area in the cross-section plane in the initial Laguerre diagram as A^0, the growth rate of normalized mean cell area in 2D amounts to

$$g_a(t) = A^t/A^0 \tag{4.42}$$

From the data of N_3^t, the cell growth rate in 3D may be verified as follows. Since the Laguerre diagram is in $\mathbb{T}^3$, thus at any time

$$\sum_i v_i = 1 \tag{4.43}$$

The mean cell volume is written as

$$V^t = 1/N_3^t \tag{4.44}$$

Denoting the mean cell volume in the initial Laguerre diagram as V^0, the growth rate of normalized mean cell volume can be written as

$$g_v(t) = V^t/V^0 \tag{4.45}$$

[1]Clearly, $0 \leq e_i \leq 1$. A cell with eccentricity $e_i = 0$ is best fitted by a circle, while a cell with $e_i = 1$ is a line segment.

The radii of cell i in 2D and 3D are the radii of equivalent spheres having the same area and volume as the cell in the cross-section plane and in $\mathbb{T}^3$ and are given by

$$r_{2i}^t = \sqrt{A_i^t/\pi} \tag{4.46}$$

$$r_{3i}^t = \sqrt[3]{3v_i^t/4\pi} \tag{4.47}$$

The mean radii of cells in cross-section plane and in 3D directly come from the mean cell area and volume as follows.

$$R_2^t = \sqrt{A^t/\pi} \tag{4.48}$$

$$R_3^t = \sqrt[3]{3V^t/4\pi} \tag{4.49}$$

Based on these measurements, following seven distribution functions are investigated in simulation.

(1) the distributions of normalized cell radius $f(r_2^t/R_2^t)$ in cross-section plane.

(2) the distributions of normalized cell radius $f(r_3^t/R_3^t)$ in 3D.

(3) the distributions of cell eccentricity $f(e)$ in cross-section plane.

(4) the distributions of normalized cell volume $f(v_i^t/V^t)$.

(5) the distributions of cell side number $f(n)$ in cross-section plane.

(6) the distributions of cell facet number $f(m)$.

(7) the distributions of misorientation degree of cell interface $f(\theta)$. This distribution is only checked in the anisotropic case.

Our simulation results have been compared to the 2D experimental data of the specimens of Al_2O_3 which come from 17 analyzed cross-section images totally having about 4,000 grains [Car87, Tel93][2] and have been further compared to the 3D pseudo-atomic Potts model simulation results reported by Anderson and Grest [And89] and by Righetti, Liebling and Mocellin [Rig89][3].

4.2.4 Initial Laguerre diagram

The initial Laguerre diagram in our simulation comes from a recrystallization algorithm [Rig92]. It is well-known that Johnson-Mehl model [Joh39] of recrystallization can produce a geometric structure which is known as Voronoi diagram of spheres. The structure is very similar to Laguerre diagram, since both of them are generated by a set of spheres. The only difference is their discriminating functions. It is the Euclidean distance $d(x,a) - r_a$

[2] In forthcoming discussions, these data will be referred to as Al_2O_3.

[3] From now on, these simulation results will be referred to as *Exxon* and *Righetti*, respectively.

to the sphere of center a and radius r_a for a Voronoi diagram of spheres, while it is the power $d^2(x,a) - r_a^2$ for a Laguerre diagram.

The following is a brief explanation how the Laguerre recrystallization model works. The detail algorithm can be found in [Rig92]. At the beginning ($t = 0$), the space under consideration is totally uncrystallized. Following a Poisson process for both coordinate and time, the k-th crystal, $k \geq 1$, tries to appear in position q_k at time t_k, with $t_k > t_{k-1}$. If q_k is a still uncrystallized point in the space at time t_k, then a new crystal c_i really begins to grow isotropically at constant rate from its germ q_k. In other words, a sphere $a'(t)$ of center q_k and radius $r_k(t)$ with $r_k(t) = t - t_k$ grows and crystallizes every point in the sphere before it reaches another growing sphere.

Three Laguerre diagrams were used as initial structures in our simulation: C_1, C_3 and C_6 are with 1027, 3043 and 6097 cells obtained by the Laguerre recrystallization process. Before analyzing the simulations themselves, the initial structures of C_3 and C_6 are firstly compared to the experimental data of Al_2O_3 in 2D and Potts model simulation results in 3D. The comparison is made on the six distributions as shown in Figures 4.8 to 4.13.

Briefly looking at the figures, one can find that the initial eccentricity and side distributions are very close to those of Al_2O_3. The distribution of 2D cell radius clearly departs from that of Al_2O_3. For 3D distributions, i.e., $f(r_3/R_3)$, $f(v_i/V^0)$ and $f(m)$, for lack of available experiment data to make such comparisons, the pseudo-atomic Potts 3D simulation results [And89, Rig89] are used to show that the initial 3D cell radius, volume and facet number distributions are rather far from their long-term behavior.

4.3 Simulation results

Computer simulation of both isotropic and anisotropic grain growth has been executed by using the method described as above. We examine the evolution of Laguerre diagrams C_1, C_3 and C_6 in the isotropic case and C_1 in the anisotropic case. In each case, the simulation is repeated several runs. It was found the microstructure and growth kinetics reached scaling behavior for values of Δ below 0.001 in the isotropic case and Δ below 0.0005 in the anisotropic case. The microstructure and growth kinetics from Laguerre diagram C_3 using $\Delta = 0.001$ are selected for analysis of cell distribution in the isotropic case and those of C_1 using $\Delta = 0.0005$ are selected in the anisotropic case.

The scaling behavior of grain growth in our simulation is observed in two aspects. The first is the growth kinetics of mean cell size. The second is the distributions of cell size and shape. While the distribution of misorientation of cells is only observed in the anisotropic case.

4.3.1 Kinetics of cell growth

The grain growth power law states that the mean grain radius should grow as $R(t) \propto t^{1/2}$ in any case and hence in 2D the mean grain area should grow as $A^t \propto t$ and in 3D the

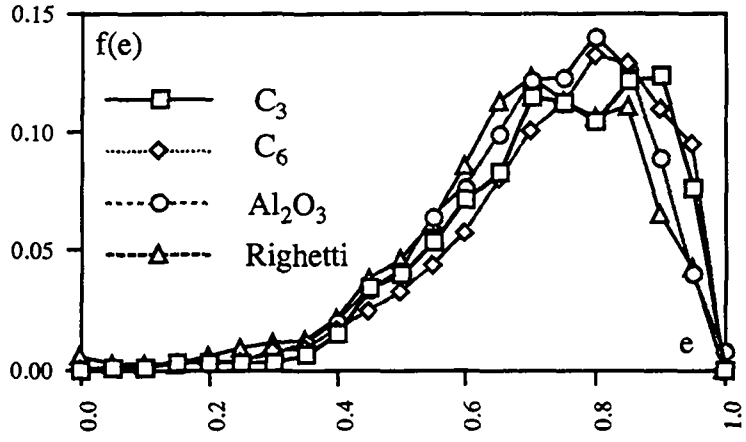

Figure 4.8: 2D cell eccentricity distribution in initial Laguerre diagrams.

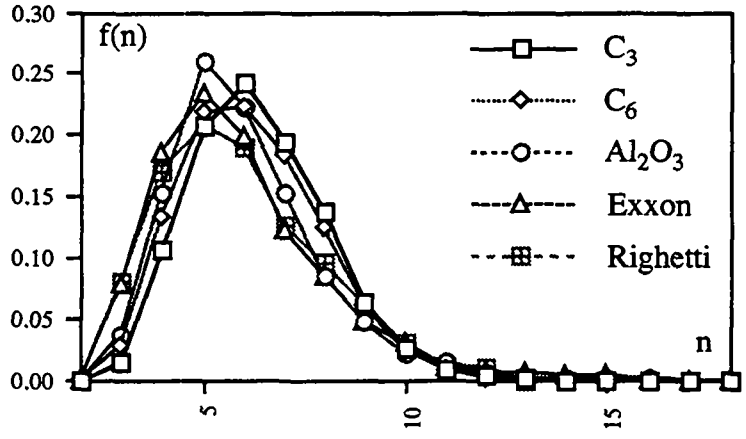

Figure 4.9: 2D cell side number distribution in initial Laguerre diagrams.

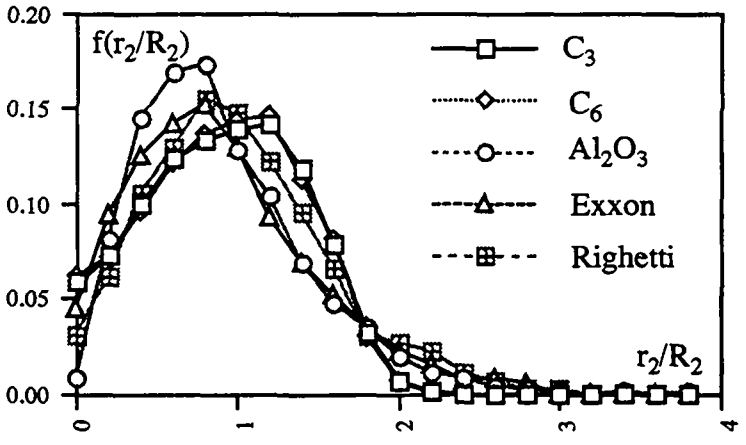

Figure 4.10: 2D cell radius distribution in initial Laguerre diagrams.

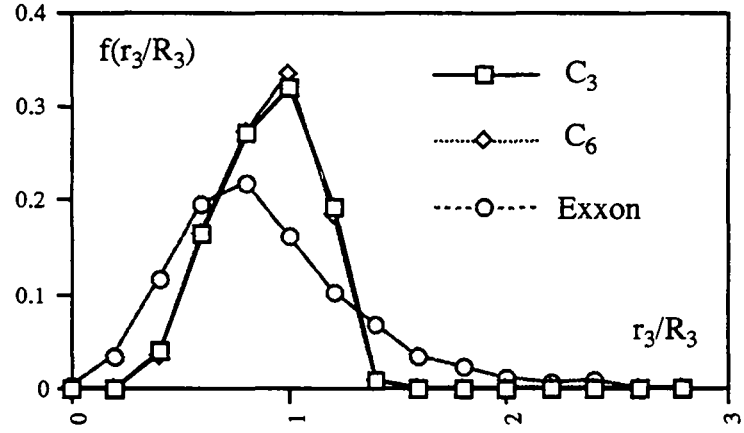

Figure 4.11: 3D cell radius distribution in initial Laguerre diagrams.

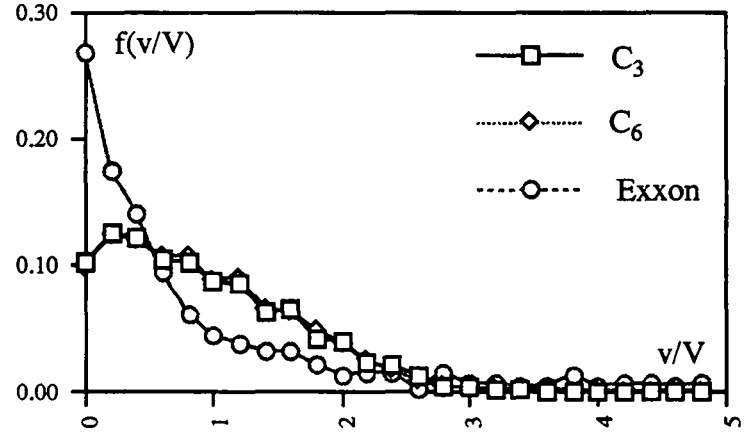

Figure 4.12: Cell volume distribution in initial Laguerre diagrams.

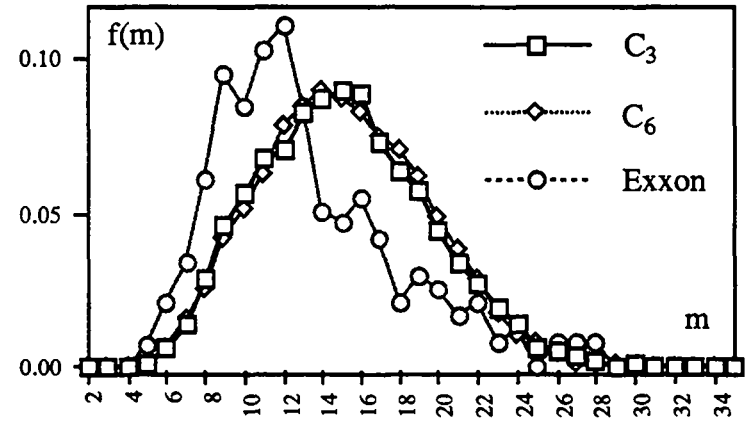

Figure 4.13: Cell facet number distribution in initial Laguerre diagrams.

mean grain volume as $V^t \propto t^{3/2}$, if the evolution of the grain system is statistically self-similar [Mul89]. Our main task here is to find out some suitable simulation parameters (in the isotropic case, they are μ and Δ and in the anisotropic case only Δ) such that the mean cell area in cross-section, A^t linearly increases with simulation time t and the mean cell volume, V^t increases against t with an exponent 3/2. If such two functions can be observed in long-term regime, then it is said that the simulation reproduces a certain grain growth process because the simulation obeys the grain growth power law.

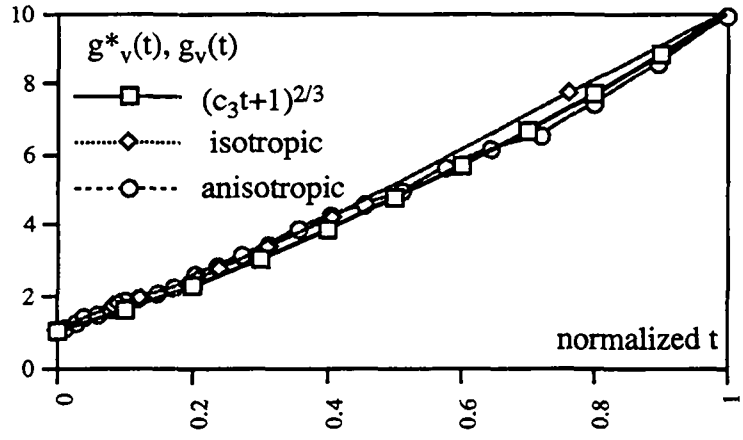

Figure 4.14: The mean cell volume growth curve in Laguerre diagram C_3.

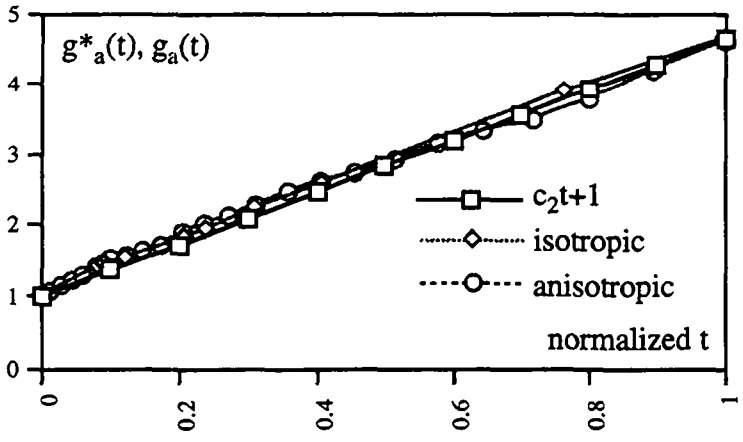

Figure 4.15: The mean cell area growth curve in 2D cross-section of C_3.

In Figures 4.14 and 4.15 the simulation time is normalized by its maximum for comparing the different simulations in the same time scale. As in the normalized time ranging from 0 to 1, the normalized mean cell volume grows from 1 to 10, from Equation 2.2, the ideal mean cell volume growth curve can be written as

$$g_v^*(t) = (c_3 t + 1)^{3/2} \tag{4.50}$$

where $c_3 = 10^{2/3} - 1$. Correspondingly, in 2D the ideal mean cell area growth curve is given by

$$g_a^*(t) = c_2 t + 1 \tag{4.51}$$

In the normalized time ranging from 0 to 1, the normalized mean cell volume grows from 1 to 10 and meanwhile the normalized mean cell area grows from 1 to $10^{2/3}$, thus constant c_2 comes to $10^{2/3} - 1$. The curves of $g_v^*(t)$ and $g_a^*(t)$ are illustrated by dense lines in Figures 4.14 and 4.15, respectively.

Obviously, the curves of the normalized mean cell area in 2d and the normalized mean cell volume (in 3D) against normalized simulation time for isotropic and anisotropic Laguerre simulation are both very close to the grain growth power law. This is an indication that the Laguerre simulation can be statistically self-similar. As a matter of fact, in both cases, it has been found that after roughly half the initial cells vanished, the cell complex enters another regime in which the geometrical and topological distributions of cells are relatively time-invariant, compared to the transient regime. Such phenomenon is very similar to the long term behavior of normal grain growth process in polycrystalline materials.

Figures 4.16 and 4.17 are a set of snapshots of the evolution of Laguerre diagram C_3 in the isotropic case ($\mu = 0.5$). The 3D images are viewed from point $(0.5, 0.5, 1.5)$ and the 2D images come from the cross-section plane with $x_3 = 0$. Thereby, the cross-section pictures one-to-one correspond to the three-dimensional ones.

4.3.2 Distribution of cell size and shape

The distributions of cell size measured by normalized cell radius, i.e., $f(r_3^t/R_3^t)$ and $f(r_2^t/R_2^t)$ are presented in Figures 4.18 and 4.19, respectively. Figure 4.19 shows that in a cross-section plane of Laguerre diagram there are many more small cells than in 3D. This is due to the so-called stereological transformation [And89]. Denoting the probability distribution function that a truncated octahedron of radius r_{max} provides a cross-section having radius r when it is intersected by a section plane as $f(r/r_{max})$, the probability

$$P\{r/r_{max} \in [0, 0.8]\} = \int_0^{0.8} f(r/r_{max})dr \doteq 0.7$$

Thereby, in a cross-section plane more small cells were observed.

To measure cell morphology, the distribution of cell eccentricity in cross-section plane is used. The evolution of cell eccentricity is presented in Figures 4.20. Up to now we have not found any other group's report on the eccentricity distribution. But in the domain of mathematical morphology, the eccentricity and its distribution are often used to approximately represent an image [Dou93]. The distribution of normalized cell volume is shown in Figure 4.21 with pseudo-atomic Potts model simulation results [And89].

Figures 4.22 and 4.23 show the distribution of side and facet numbers for individual cells observed in cross-section plane and in 3D Laguerre diagram, respectively. These figures (Figures 4.18-4.23) make it clear that after roughly half the initial cells vanished, namely $t > 0.41$, the process enters the scaling regime, viz, the distribution of the cell size

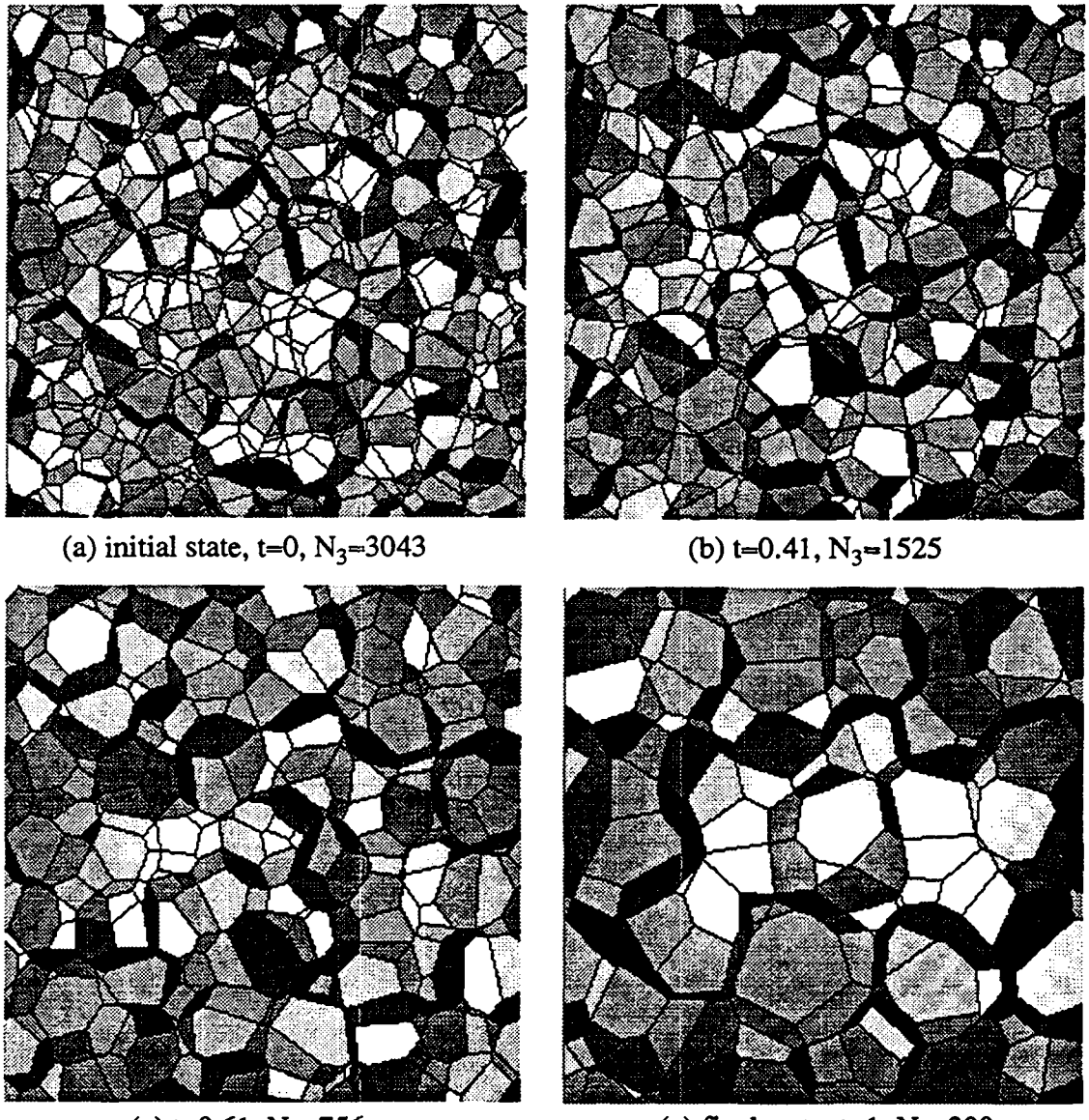

(a) initial state, t=0, N_3=3043

(b) t=0.41, N_3=1525

(c) t=0.61, N_3=756

(c) final state, t=1, N_3=300

Figure 4.16: The evolution of Laguerre diagram of C_3.

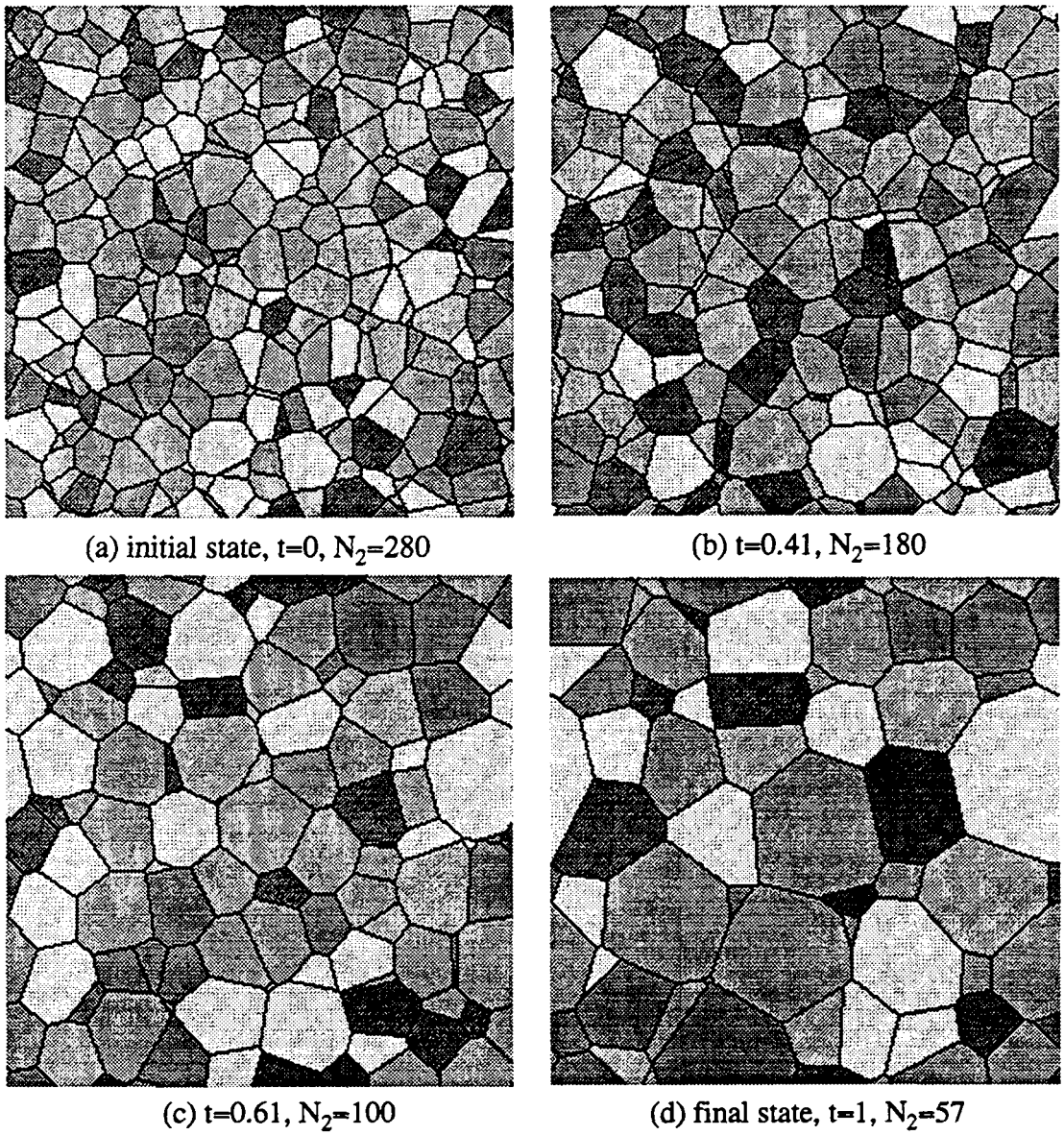

(a) initial state, t=0, N_2=280

(b) t=0.41, N_2=180

(c) t=0.61, N_2=100

(d) final state, t=1, N_2=57

Figure 4.17: The evolution of C_3 in cross section plane $x_3 = 0$.

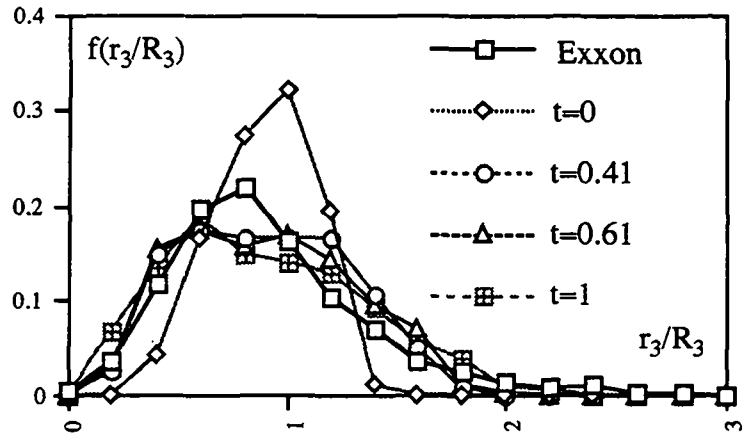

Figure 4.18: 3D cell radius distributions at different stage.

	Mean	Min	Max	Most frequent	Reference
30 β-brass	14.5	-	-	-	[And89]
100 Al-Sn alloy	12.48	6	23	10	[Wil52]
Potts model	12.85	4	27	11	[And89]
Vertex model	14.13	4	34	11	[Fuc95]
Laguerre diagram	15.16	4	35	15	[Rig92]
Laguerre model	13.72	4	36	11	-

Table 4.2: Characteristics of the distribution of facet number per cell.

and shape is nearly time-invariant. Thereby the second main attribute of normal grain growth process is reproduced by the simulation.

The number of facets per cell is an important parameter in the sense of the topology of a cell complex. The experimental data and varieties of computational results are summarized in Tables 4.2. During the evolution of Laguerre diagram, the range of cell size is enlarged compared to in its initial state, therefore after sufficient "annealing", in the final diagram the topological characteristic is approaching much more the real polycrystalline materials.

The influence of directional growth parameter μ in the isotropic case is investigated through three simulations with the same Δ but different μ (= 0.25, 0.5, 0.75) for C_3 and $\mu = 0.6$ for C_6. In Figures 4.24-4.26 three 2D distributions in final state are compared. It is apparent from the figures that all the distributions tend to close to each other and μ between 0.5 to 0.75 are the values that yield the closest (not very good) approximation to the experimental data of Al_2O_3.

However, the parameter μ could not touch the kernel of anisotropic grain growth, it is demanded to directly simulate the process in anisotropic case. The preliminary results reported here is from the simulation of Laguerre diagram C_1. To compare to the isotropic

case, the final results of both isotropic ($\mu = 0.5$) and anisotropic simulations are illustrated in Figures 4.27-4.30. Notice that in Figure 4.30, the distribution of side number in cross-section plane is normalized by the probability of the most frequent class, thus it is noted as $f^*(n)$. In this verified example, there is no significant difference between the isotropic simulation and the anisotropic one in the sense of approaching the experimental data of Al_2O_3. This may be due to that the anisotropic parameter we used, i.e., the plot of $\gamma(\theta)$ is weakly anisotropic one. Nevertheless, it is of interest to note that by this anisotropic model, the evolution of distribution of misorientation can be emulated, which will be discussed in next subsection.

4.3.3 Distribution of misorientation

As in the Laguerre model, the anisotropy of grain growth results from the anisotropic grain boundary energy determined by the misorientation of the grain boundary, the distribution of misorientation plays an important role in the process. Such computer simulations has not been reported so far.

Figure 4.31 shows the misorientation distributions in the initial and final Laguerre diagrams. In both cases, more than 90% facets are the large angle thus high energy ones. On the other hand, the mean misorientation degree in the final state is significantly larger than in the initial state. This can be explained as due to that in the grain growth process low energy grain boundaries are replaced by high energy ones, which is well consistent with the experimental results in some polycrystalline materials [Wat92]. Obviously, only in the anisotropic case is the discussion of misorientation distribution meaningful.

4.4 Summary

In this study, the three-dimensional Laguerre model is established and then it is generalized to the anisotropic case. In the later case, the distribution of grain boundary misorientation and its evolution can be simulated. Preliminary simulation results show that the grain growth kinetics and the distribution of misorientation are well consistent with those from the statistical grain growth theory [Mul89] and experiments [Wat92]. Inasmuch as the main attributes of normal grain growth process, i.e., the growth kinetics, the distribution of grain size and shape and the scaling behavior of the distribution are reproduced, it is reasonable to say that both of isotropic and anisotropic Laguerre models can simulate the normal grain growth process in certain polycrystalline materials.

In the current model, the anisotropic grain growth only results from the anisotropy of grain boundary energy whereas the grain boundary mobility is supposed to be isotropic, which seems rather restrictive. It is well known, the migration of grain boundary results from the grain boundary energy and mobility as well. Experiments have shown that for certain polycrystalline materials, the anisotropy of grain boundary mobility is so evident that it can not be totally neglected [Got92]. Unfortunately, our current model is unable to account for the anisotropic grain boundary mobility.

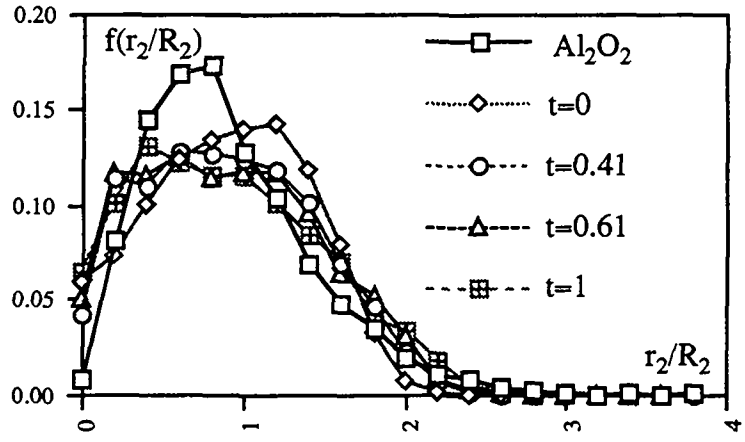

Figure 4.19: Cell radius distributions in 2D cross-section at different stage.

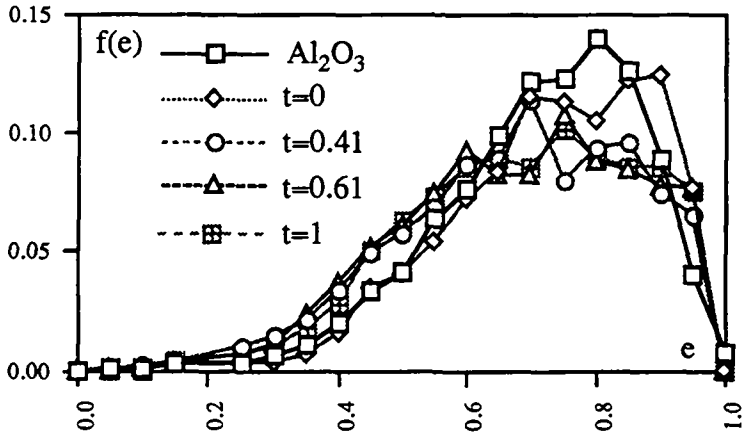

Figure 4.20: Cell eccentricity distributions in 2D cross-section at different stage.

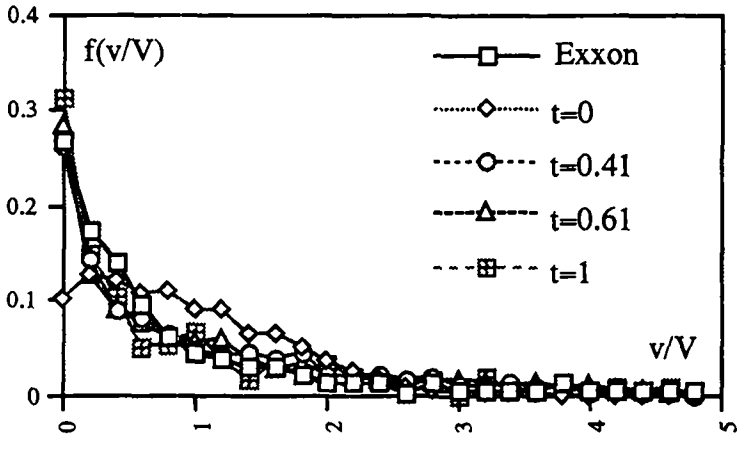

Figure 4.21: Cell volume distributions at different stage.

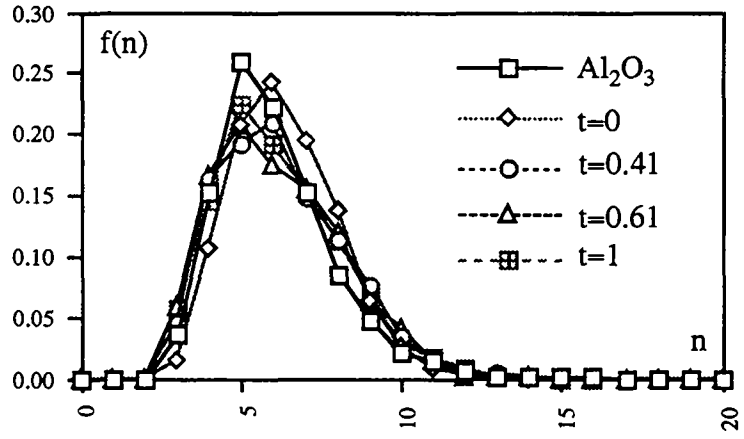

Figure 4.22: Cell side number distributions in 2D cross-section at different stage.

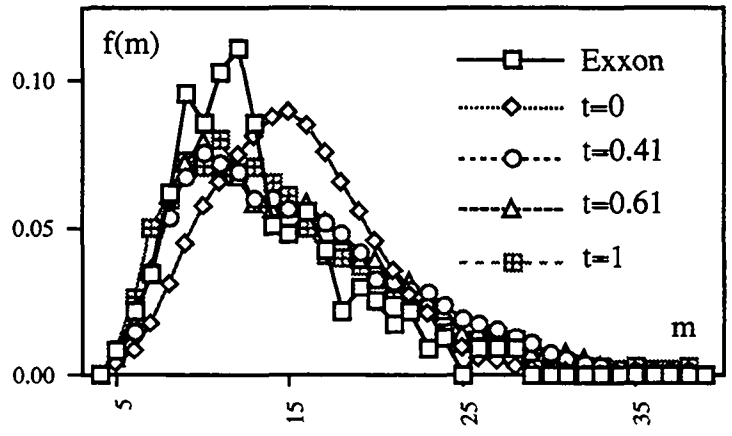

Figure 4.23: Cell facet number distributions at different stage.

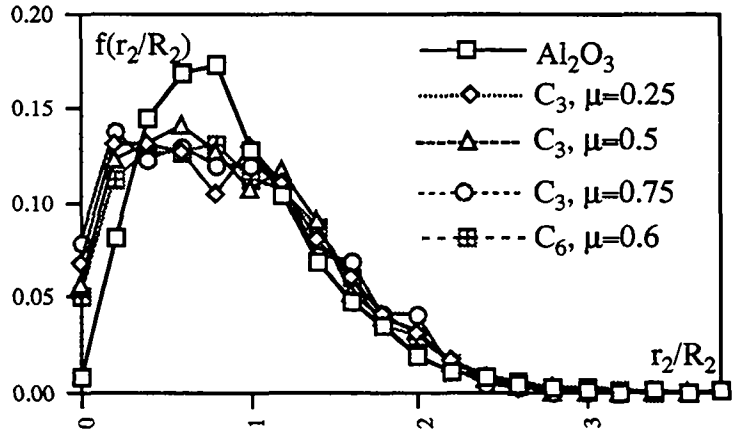

Figure 4.24: The influence of μ on cell radius in 2D cross-section.

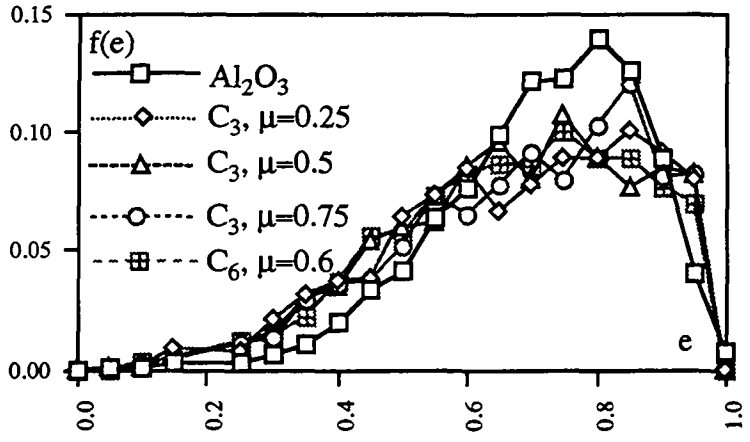

Figure 4.25: The influence of μ on cell eccentricity in 2D cross-section.

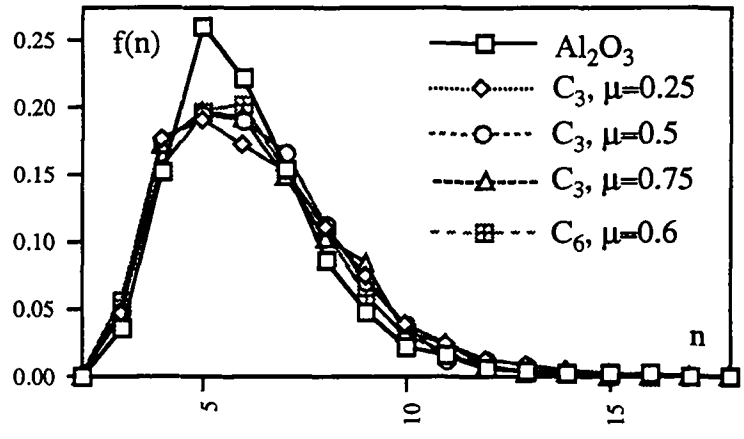

Figure 4.26: The influence of μ on cell side number in 2D cross-section.

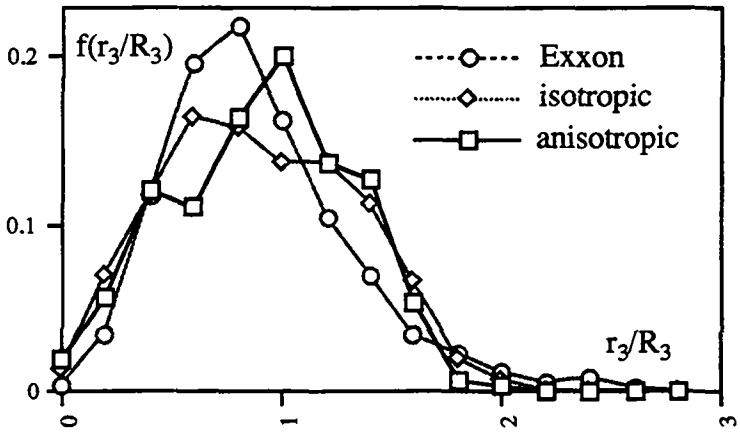

Figure 4.27: Final 3D cell radius distribution in isotropic and anisotropic case.

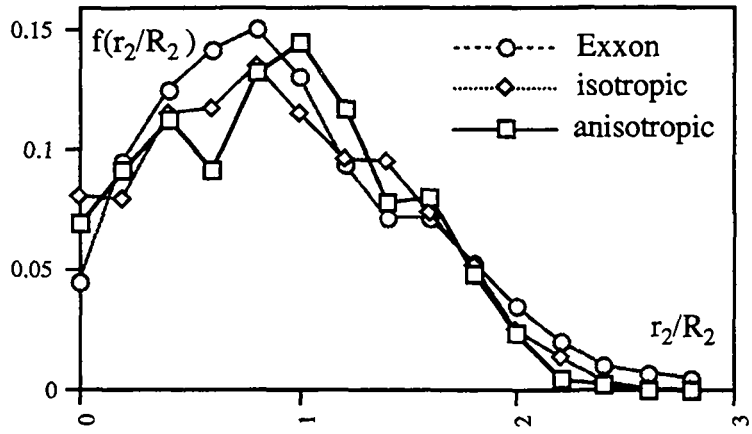

Figure 4.28: Final 2D cell radius distribution in isotropic and anisotropic case.

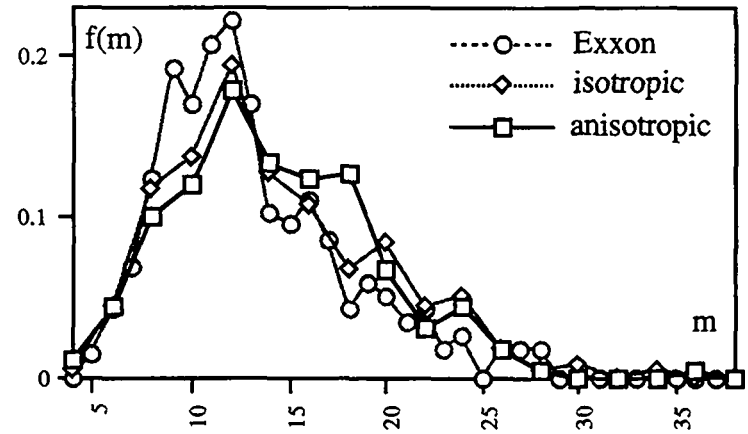

Figure 4.29: Final cell facet number distribution in isotropic and anisotropic case.

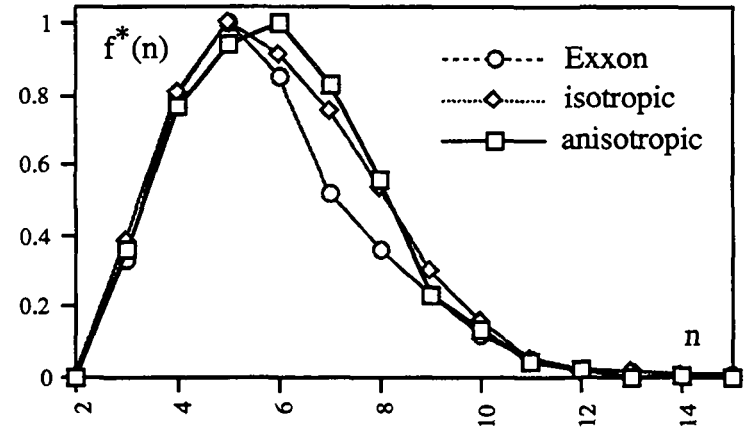

Figure 4.30: Final cell side number distribution in isotropic and anisotropic case.

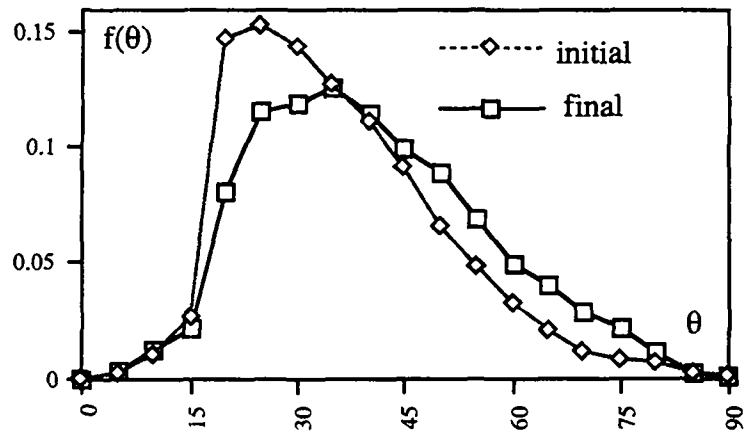

Figure 4.31: Misorientation distribution at the initial and final stage.

Finally we should point out that another interesting subject to study with anisotropic models is the effect of several specific texture components in texture developing grain growth, like for instance in Abbruzzese Lücke's two texture components model [Abb86]. We will continue to discuss this subject in next chapter.

Chapter 5

Laguerre Model for Heterogeneous Grain Growth in 2D

The specification of grain boundary energy is a very complicated multi-parameter problem, as shown in Equation 4.35. As a reliable and complete experimental database is not yet available for any material system, we suggest to proceed in steps and to simplify simulation, e.g. Equation 4.38 has been proposed to treat the energy as a univariable function of misorientation. As a further step, Abbruzzese and Lücke [Abb86] considered a heterogeneous system in which only a finite number of types of grains exist. The grain boundary energy in the system is supposed to be only determined by the type of grains which form the boundary. More precisely, we suppose the heterogeneous grain system is such that

(i) Several types of grains are presented in the system. Each grain can either consume or be consumed by the same or different type neighboring grains.

(ii) The type of a grain is time-invariant. Thereby, there is no new type grain generated in the evolution of the system.

(iii) Suppose $n_T \geq 2$ types of grains exist in the system and denote the specific energy of a boundary formed by a type i and a type j grain, $i, j \in \{1, ..., n_T\}$ as γ_{ij}, then the specific grain boundary energies of the system can be described by the following matrix

$$G = \begin{bmatrix} \gamma_{11} & \gamma_{12} & \cdots & \gamma_{1n_T} \\ \vdots & \vdots & \ddots & \vdots \\ \gamma_{n_T1} & \gamma_{n_T2} & \cdots & \gamma_{n_Tn_T} \end{bmatrix} \tag{5.1}$$

where $\gamma_{ij} = \gamma_{ji}, \forall\, i, j \in \{1, ..., n_T\}$. If $\gamma_{ii} = \gamma_{jj}, \forall\, i, j \in \{1, ..., n_T\}$, then matrix G is said to be fully symmetric. Otherwise, G is non-fully symmetric.

The heterogeneous grain growth under such enormously simplified assumptions is referred to as texture developing grain growth process, as crystallographic texture is likely to develop under such circumstances. Abbruzzese and Lücke [Abb86] proposed a statistical

theory to explain the effect of texture in the process and the corresponding numerical simulation which well reproduced the process in α-brass [Bri81]. Recently, it has been recognized that the texture plays an important role in grain growth in certain polycrystalline materials [Ran92]. The microstructural evolution in two-phase polycrystals has been simulated by Holm, Srolovitz and Cahn [Hol93] with 2D pseudo-atomic Potts model. Due to the limitations of statistical models, Abbruzzese-Lücke's model does not take into account the geometrical and topological restrictions at the junction of grain boundaries.

In this chapter, the 2D Laguerre model [Tel89a] for normal grain growth in a pure single phase system is extended to the heterogeneous case. By the model, the texture developing grain growth process is simulated in two types of grains present case. Computational results show that the kinetic behavior of the process has been reproduced and the microstructure of the simulated material has been displayed. For the first time, the possibility of long term oscillation of the process has been evidenced. Thus, the Laguerre model can be looked as a complement of Abbruzzese and Lücke's statistical model. Moreover, the Laguerre model provides a basic tool to investigate more complex heterogeneous systems.

5.1 Specification of Laguerre model

The two-dimensional Laguerre model for normal grain growth in pure single phase system has been proposed by Telley, Liebling, Mocellin and Righetti [Tel89a, Tel92a]. In this section, the master equation of the model, i.e., the motion equation of weighted site of Laguerre diagram is extended to the heterogeneous case, i.e., several types of grains present in a system. The range of possible specific grain boundary energy and further the admissibility of matrix G are discussed.

5.1.1 The motion equation in heterogeneous case

The derivation of 2D Laguerre diagram motion equation is almost the same as in 3D. For the sake of self containing of this Chapter, here we briefly discuss the derivation.

Given a set S' of N weighted sites in two-dimensional unit flat torus $\mathbb{T}^2$ where each site, say $a' = (a, a_3)$ is represented by its coordinate $a = (a_1, a_2) \in \mathbb{T}^2$ and its weight $a_3 \in \mathbb{R}^+$. The Laguerre diagram in $\mathbb{T}^2$ is a 3-connected network in which each Laguerre vertex $p = (p_1, p_2)$ is exactly incident to three edges and each edge is a straight line segment and terminates at two vertices. Laguerre cell $L(a')$ generated by site $a' \in S'$ is a polygon. The vertices of the polygon, denoted as $p(a')$, are determined by site a' and its nearest neighboring sites, denoted as $s(a')$. In two-dimensional normal grain growth simulation, Laguerre cells stand for grains and Laguerre edges stand for grain boundaries.

From Burke and Turnbull's grain boundary energy equation (Equation 2.4), the interfacial energy of 2D Laguerre diagram $L(S')$ is the sum of Laguerre edge energy , i.e.,

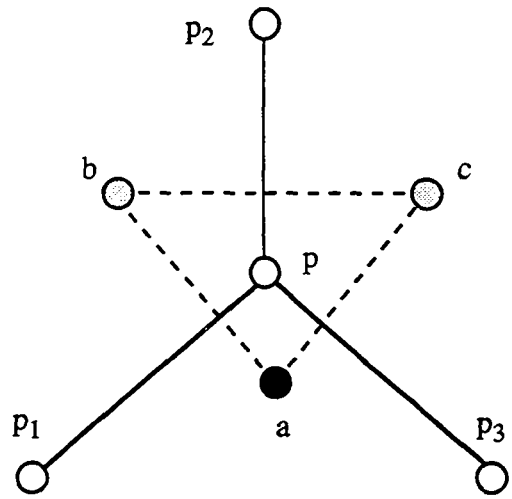

Figure 5.1: Three Laguerre edges are incident to a Laguerre vertex p.

(see Figure 5.1)

$$E = \sum_{\forall p} E_p = \frac{1}{2} \sum_{\forall p} \sum_{i=1}^{3} \gamma_{pp_i} |p - p_i| \tag{5.2}$$

where γ_{pp_i} is the specific energy of edge pp_i and is determined by the material crystallography and the misorientation of neighboring cells which share the edge. In our model the normal grain growth process is simulated in such a way that every Laguerre edge tends to shrink. Therefore the system's energy decreases, meanwhile space $\mathbb{T}^2$ is always filled by the cell complex. In the process, small cells tend to vanish and big ones to expand, whereas the distribution of cell size normalized by the mean cell size is stable in long-term regime. To obtain meaningful statistics, the simulation should be stopped when several hundred cells still remain in the diagram. The driving force exerted on Laguerre vertex p works to minimize the local interfacial energy E_p and is opposite to the derivative of system energy with respect to p, i.e.,

$$F_p = -\frac{\partial E}{\partial p} = -\frac{\partial E_p}{\partial p} = -\frac{1}{2}\frac{\partial}{\partial p}\left(\gamma_{ab}|p - p_1| + \gamma_{bc}|p - p_2| + \gamma_{ac}|p - p_3|\right) \tag{5.3}$$

Suppose p_1, p_2 and p_3 are fixed and p is the unique variable in Equation 5.3, the driving force is given by

$$F_p = -\frac{1}{2}\left(\gamma_{ab}\frac{p - p_1}{|p - p_1|} + \gamma_{bc}\frac{p - p_2}{|p - p_2|} + \gamma_{ac}\frac{p - p_3}{|p - p_3|}\right) \tag{5.4}$$

As a Laguerre edge is always perpendicular to its corresponding weighted Delaunay edge in 2D, Equation 5.4 can be written in a more concise manner

$$F_p = -\frac{1}{2}\left(\gamma_{ab}u_{ab}^{\perp} + \gamma_{bc}u_{bc}^{\perp} + \gamma_{ac}u_{ac}^{\perp}\right) \tag{5.5}$$

where $u_{ab}^{\perp}$ is the unit normal of weighted Delaunay edge ab oriented to the interior of weighted Delaunay cell abc. Properly transforming this force to its supporting weighted site and supposing the Laguerre diagram satisfies Assumption 5, the velocity of site a' comes to

$$\begin{cases} \dot{a} = \dfrac{\sum_p \frac{1}{h}\langle F_p, u_{bc}^{\perp}\rangle (a-p)}{\rho \mathcal{A}_a} \\ \dot{r}_a = -\dfrac{\sum_p \frac{r_a}{h}\langle F_p, u_{bc}^{\perp}\rangle}{\rho \mathcal{A}_{r_a}} \end{cases} \tag{5.6}$$

where h is the height of the Delaunay triangle in the direction of $u_{bc}^{\perp}$, $\sum_p$ is over Laguerre vertices of the cell, ρ is the coefficient of friction and $r_a^2 = a_3$. As mentioned in Chapter 4, $\rho = 1/M$ and M is supposed to be isotropic, thus $\rho = 1$. $\mathcal{A}_a$ and $\mathcal{A}_{r_a}$ are the Plateau length of the cell in its displacement and radial motion directions, respectively[1].

Compared to the isotropic case, the only difference is that in Equation 5.5 the calculation of driving force exerted on a Laguerre vertex should take into account the different specific interfacial energies γ_{ab}, γ_{bc} and γ_{ac}. Notice that γ_{ab} is an element of matrix G as defined in Equation 5.1. By introducing individual specific grain boundary energy into the motion equation, the Laguerre model is extended into the heterogeneous case.

5.1.2 Example: G for two types of grains

In a heterogeneous grain system, different types of grain boundaries have different specific interfacial energy. The general specification of the energy has been shown in Equation 5.1. Here, we focus on the special case $n_T = 2$, i.e., in the simulated material only two types of grains are supposed to be present. Such a case study was initiated by Smith [Smi48] and then by Abbruzzese and Lücke [Abb86]. Since all the grains can be classified into two classes, namely each grain is either type A or type B (A-cell or B-cell, for short), three types of grain boundaries exist in the material and hence three types of specific grain boundary energies, noted as γ_{AA}, γ_{BB} and $\gamma_{AB}(\equiv \gamma_{BA})$, respectively. The corresponding matrix G can be written as

$$G = \begin{bmatrix} \gamma_{AA} & \gamma_{AB} \\ \gamma_{AB} & \gamma_{BB} \end{bmatrix} \tag{5.7}$$

These three types of grain boundaries form four types of triple junctions in the system, i.e., three A-cells meet at a point, noted as AAA-point, three B-cells meet at a point (BBB-point), an A-cell and two B-cells meet at a point (ABB-point) and two A-cells and a B-cells meet at a point (AAB-point). From the surface tension equilibrium condition at an ABB triple junction, namely Equation 2.8, the values of γ_{BB} and γ_{AB}

[1] Comparing in 3D, $\mathcal{A}_a$ and $\mathcal{A}_{r_a}$ are the Plateau area of a cell in its displacement and radial motion directions (See §4.1).

should satisfy (see Figure 5.2(a))

$$\gamma_{BB} = 2\gamma_{AB}\cos\frac{\alpha}{2} \tag{5.8}$$

For the same reason, at an AAB triple junction (see Figure 5.2(a)),

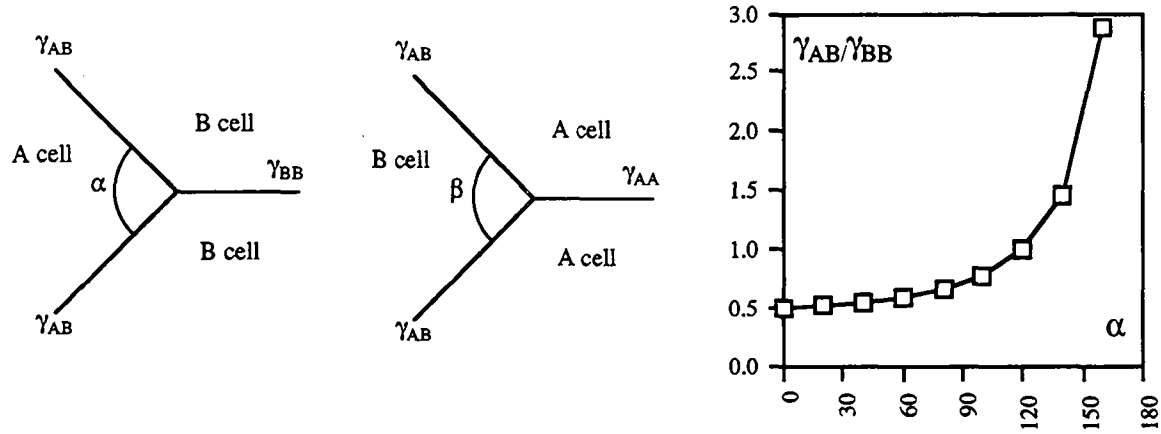

(a) dihedral angle α (b) dihedral angle β (b) dependence of γ_{AB}/γ_{BB} on α

Figure 5.2: Dihedral angles and specific grain boundary energies.

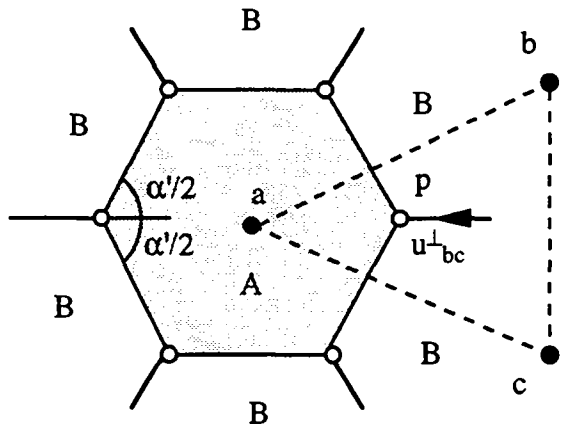

Figure 5.3: The growth direction of an isolated symmetric A-cell.

$$\gamma_{AA} = 2\gamma_{AB}\cos\frac{\beta}{2} \tag{5.9}$$

A plot of Equation 5.8 is presented in Figure 5.2(c). At an AAA or BBB point, the three dihedral angles are 120°.

By Equation 5.8, one can determine the growth direction of an isolated[2] n-sided symmetric A-cell with symmetric edge junctions (see Figure 5.3). Substituting Equation

[2]The term "isolated A-cell" means a type A cell is surrounded by type B-cells.

5.8 into 5.5 and considering the geometrical symmetry of the cell, the driving force exerted on the Laguerre vertex p comes to

$$\begin{aligned} F_p &= -\frac{1}{2}\left(\frac{\gamma_{BB}}{2\cos\frac{\alpha}{2}}u_{ab}^{\perp} + \frac{\gamma_{BB}}{2\cos\frac{\alpha}{2}}u_{ac}^{\perp} + \gamma_{BB}u_{bc}^{\perp}\right) \\ &= -\frac{\gamma_{BB}}{2}\left(-\frac{cos\frac{\alpha'}{2}}{2\cos\frac{\alpha}{2}} - \frac{cos\frac{\alpha'}{2}}{2\cos\frac{\alpha}{2}} + 1\right)u_{bc}^{\perp} \\ &= -\frac{\gamma_{BB}}{2}\left(1 - \frac{cos\frac{\alpha'}{2}}{\cos\frac{\alpha}{2}}\right)u_{bc}^{\perp} \end{aligned} \tag{5.10}$$

Since α, $\alpha' \in [0, \pi]$,

$$\begin{cases} F_p \text{ is parallel to } u_{bc}^{\perp}, \text{ if } \alpha' < \alpha; \\ F_p \text{ is opposite to } u_{bc}^{\perp}, \text{ if } \alpha' > \alpha; \end{cases}$$

Substituting Equation 5.10 into 5.6, by the symmetry of the cell, $\dot{a} = 0$ and

$$\begin{cases} \dot{r}_a < 0, \text{ if } \alpha' < \alpha; \\ \dot{r}_a > 0, \text{ if } \alpha' > \alpha; \end{cases}$$

In other words, the cell will be consumed if its dihedral angle α' is less than the equilibrium dihedral angle α, while the cell will consume its neighbors if $\alpha' > \alpha$.

Correspondingly, the growth direction of an isolated n-sided symmetric B-cell can be determined by Equations 5.5, 5.6 and 5.9. As γ_{AA} is not necessarily equal to γ_{BB}, the driving force exerted on an AAA point is different to that on a BBB point. The growth rates of an n-sided symmetric A-cell and B-cell surrounded by their heterogeneous cells are thus different.

An example of experimental validity of Equations 5.8 and 5.9 was provided by Cotterill and Mould's investigation of α-brass [Cot76]. They found that the dihedral angles $\alpha = 95°$ and $\beta = 120°$, and hence $\gamma_{AB}/\gamma_{BB} = 0.74$ and $\gamma_{AB}/\gamma_{AA} = 1$. The ratio γ_{AB}/γ_{BB} (γ_{AB}/γ_{AA}) ranging from 0.68 to 0.78 (0.74 to 1) due to the different compositions and annealing conditions has been reported [Smi48].

Notice that in Equation 5.7 γ_{AA}, γ_{BB} and γ_{AB} may be different from each other. By Equations 5.8 and 5.9, the dihedral angles α, $\beta \in [0, \pi]$ and the relations among the three parameters should satisfy

$$\begin{cases} 0.5 \leq \gamma_{AB}/\gamma_{BB} < \infty \\ 0.5 \leq \gamma_{AB}/\gamma_{AA} < \infty \\ \gamma_{AA}, \gamma_{BB}, \gamma_{AB} > 0 \end{cases} \tag{5.11}$$

Suppose in the initial state A-cells are minority population in a cell system, by Equation 5.11, all admissible combinations of the three parameters, i.e., γ_{AA}, γ_{BB} and γ_{AB} can be sorted into nine classes as shown in the first three columns of Table 5.1. The fourth column of the table shows a series of admissible matrices G which have been tested in our simulation. Cases 1, 2, and 3 have been studied by Abbruzzese and Lücke [Abb86] with their

case	γ_{AA} vs. γ_{BB}	γ_{AB} vs. $\{\gamma_{AA}, \gamma_{BB}\}$	a tested matrix G
1	$\gamma_{AA} = \gamma_{BB}$	$\gamma_{AB} < \gamma_{AA}$	$G_1 = \begin{bmatrix} 1 & 0.5 \\ 0.5 & 1 \end{bmatrix}$
2		$\gamma_{AB} = \gamma_{AA}$	$G_2 = \begin{bmatrix} 1 & 1 \\ 1 & 1 \end{bmatrix}$
3		$\gamma_{AB} > \gamma_{AA}$	$G_3 = \begin{bmatrix} 1 & 2 \\ 2 & 1 \end{bmatrix}$
4	$\gamma_{AA} < \gamma_{BB}$	$\gamma_{AA} < \gamma_{AB} < \gamma_{BB}$	$G_4 = \begin{bmatrix} 0.5 & 1 \\ 1 & 2 \end{bmatrix}$
5		$\gamma_{AB} \leq \gamma_{AA}$	$G_5 = \begin{bmatrix} 1 & 1 \\ 1 & 2 \end{bmatrix}$
6		$\gamma_{AB} \geq \gamma_{BB}$	$G_6 = \begin{bmatrix} 0.5 & 1 \\ 1 & 1 \end{bmatrix}$
7	$\gamma_{BB} < \gamma_{AA}$	$\gamma_{BB} < \gamma_{AB} < \gamma_{AA}$	$G_7 = \begin{bmatrix} 2 & 1 \\ 1 & 0.5 \end{bmatrix}$
8		$\gamma_{AB} \leq \gamma_{BB}$	$G_8 = \begin{bmatrix} 2 & 1 \\ 1 & 1 \end{bmatrix}$
9		$\gamma_{AB} \geq \gamma_{AA}$	$G_9 = \begin{bmatrix} 1 & 1 \\ 1 & 0.5 \end{bmatrix}$

Table 5.1: Admissible γ_{AA}, γ_{BB} and γ_{AB}.

statistical model. Case 2, i.e., a pure single phase system, has been simulation by Telley [Tel89a] with Laguerre model. In this study, all the nine cases have been investigated. With different matrices γ_{AB} in G, the first three cases are intensively investigated to verify the eligibility of the extended Laguerre model. The remaining six cases are briefly probed in order to further recognize the effect of matrix G on the long-term kinetic behavior of texture developing grain growth process. Before presenting the simulation results, let us first have a look of the simulation protocol.

5.2 Simulation protocol

For emulating the existence of two types of grains in a heterogeneous system, the bi-partition of cells of an initial Laguerre diagram is first discussed. A novel measurement called the coefficient of homologue neighborhood of A-cell is defined to quantitatively characterize the neighborhood of the same type cell.

5.2.1 Simulation scheme

Suppose a Laguerre diagram $L(S'^0)$ with N^0 initial cells has been constructed, in order to adapt to the two types of grains, the weighted site set S'^0 should be bipartitioned into S'^0_A and S'^0_B following some desired distributions. In our simulation, three parameters are introduced. The first two called "type A cell lower and upper eligibility bound", denoted as l_A and u_A, specify the range of type A cell radius. The third one is called "type A cell probability threshold", noted as T_A, $0 \leq T_A \leq 1$. Suppose each cell is given a random number c_i uniformly distributed in $[0,1]$. If a cell, say cell i, satisfies

$$\begin{cases} c_i \leq T_A \\ l_A \leq r_i/R^0 \leq u_A \end{cases} \tag{5.12}$$

then the cell belongs to S'^0_A, otherwise to S'^0_B, where R^0 is the mean cell radius in $L(S'^0)$. After such an initial bipartition, Laguerre cells in $L(S'^0)$ are separated into two classes and occupy F_A and F_B fraction of area in $\mathbb{T}^2$, respectively. Obviously,

$$F_A + F_B = 1 \tag{5.13}$$

In the case of two types of grains present in a grain system, three types of grain boundaries could appear in the simulated Laguerre diagram. Suppose $\gamma_{AA} = \gamma_{BB} = 1$ and $\gamma_{AB} = \gamma_{BA}$ the grain boundary energy matrix G is thus a fully symmetric matrix,

$$G = \begin{bmatrix} 1 & \gamma_{AB} \\ \gamma_{AB} & 1 \end{bmatrix} \tag{5.14}$$

where the value of γ_{AB} is subject to be modified in order to represent different specific grain boundary energy in different materials.

The simulation procedure described in §4.2.1 can be used to simulate the texture developing grain growth process. The only difference is that in this case, the specific Laguerre edge energy is specified by the type of cells and matrix G.

5.2.2 Definition of measurements

As two types of grains present in the simulated material, the mean cell radii are now measured in S'_A and S'_B, denoted as R_A and R_B, respectively. The distributions of normalized cell radii are then defined as $f(r/R)$, $f(r_A/R)$ and $f(r_B/R)$, respectively. Similarly, the distributions of cell side number in S'_A and S'_B are noted as $f_A(n)$ and $f_B(n)$, respectively. Distribution function $f_A(n)$ is defined as

$$f_A(n) = \frac{\text{the number of } n-\text{sided } A-\text{cells}}{\text{the number of cells in the whole system}},\ n = 3,4,... \tag{5.15}$$

Moreover, the distribution of cell side number in the cell system is defined as

$$f_{A\bigcup B}(n) = f_A(n) + f_B(n),\ n = 3,4,... \tag{5.16}$$

To characterize the neighborhood of the same type cells, a novel measurement called the coefficient of homologue neighborhood is monitored in our simulation.

Definition 5.1 *The coefficient of homologue neighborhood of n-sided A-cell is defined as*

$$h_n^A = \frac{1}{n \cdot \eta_n^A} \sum_j \xi_{nj}^A, \; n = 3, \; 4, \; \ldots \tag{5.17}$$

where η_n^A is the number of n-sided A-cells and ξ_{nj}^A the number of A-neighbors of the j-th n-sided A-cell.

Obviously, $0 \leq h_n^A \leq 1$, for any $n \geq 3$. The coefficient of homologue neighborhood of n-sided B-cell, noted as h_n^B and further the coefficient of non-homologue neighborhood of n-sided type A (B) cell, noted as h_n^{AB} (h_n^{BA}) can be defined in the same way. The following relationships evidently hold (see Figure 5.4):

$$\begin{cases} h_n^A + h_n^{AB} = 1 \\ h_n^B + h_n^{BA} = 1 \end{cases} \tag{5.18}$$

Suppose $cell_i$ is the unique 5-sided A-cell in the cell system as shown in Figure 5.4(a),

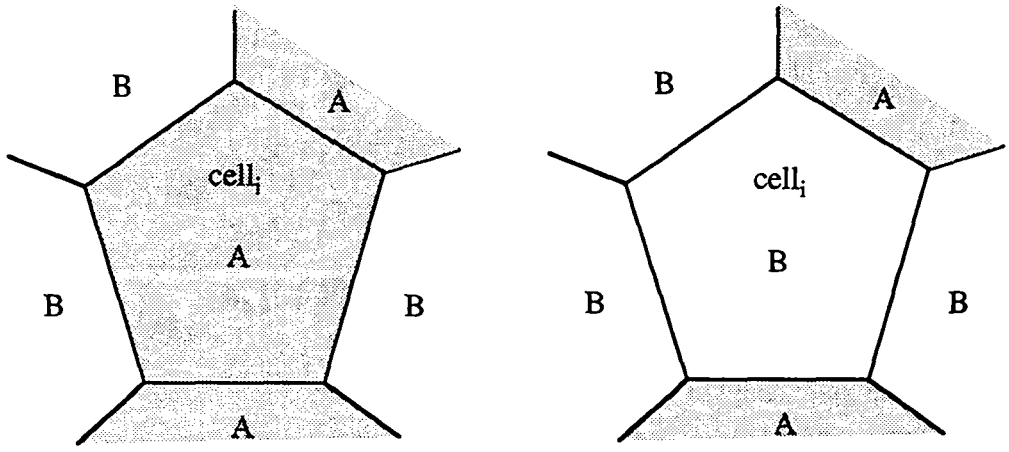

(a) $cell_i$ is a type A cell (b) $cell_i$ is a type B cell

Figure 5.4: Type A (B) cell and its neighbors.

then $h_5^A = \frac{2}{5}$ and $h_5^{AB} = \frac{3}{5}$. Similarly, in Figure 5.4(b) $h_5^B = \frac{3}{5}$ and $h_5^{BA} = \frac{2}{5}$. The mean coefficient of homologue neighborhood of A-cell, H^A is defined as

$$H^A = \frac{1}{n_{max}^A - 2} \sum_{n=3}^{n_{max}^A} h_n^A \tag{5.19}$$

where, n_{max}^A is the maximal side number of A-cells in the cell system. Evidently, $0 \leq H^A \leq 1$. In fact, parameters h_n^A and H^A reflect the extent of cluster of A-cells in the cell system. For instance,

$$\begin{cases} H^A = 0, & \text{all } A\text{-cells are isolated;} \\ 0 < H^A < 1, & \text{some } A\text{-cells are clustered;} \\ H^A = 1, & \text{in the system only } A\text{-cells exist.} \end{cases}$$

A cluster of A-cells is called an A-cluster. The dependence of h_n^A and H^A on simulation time t and on specific grain boundary energy γ_{AB} in the case of $\gamma_{AA} = \gamma_{BB}$ has been observed in our simulation.

5.3 Simulation results

Computational simulation of texture developing grain growth has been carried out on the Laguerre diagrams D_1 and D_2 initially with 1,047 and 10,117 cells in case where two types of grains are present. A standard simulation, that is the Laguerre diagram evolved till 4% initial cells remained was first carried out to make sure that the model can reproduce the physical process described by Brickenkamp and Lücke [Bri81]. For investigating the possible oscillation of the competition between two populations, a long-time simulation, i.e., the simulation continued till 2% initial cells remained, was done.

First of all, some snapshots of the evolution of D_1 are shown in Figures 5.5-5.7. Tables 5.2 and 5.3 are the data corresponding to these images. The initial state of the Laguerre diagram is shown in Figure 5.5. Evidently, the population B dominates the image. The diagram is evolved with $\gamma_{AB} = 0.74$ in Figure 5.6 and $\gamma_{AB} = 0.5$ in Figure 5.7 (in both simulations, $\gamma_{AA} = \gamma_{BB} = 1$). In the first simulation, the minority population grew to dominate the image and kept this domination till the simulation stopped. However, in the second simulation, the domination status was unstable. In the investigating scale, several switching points, i.e., at which $F_A = F_B = 0.5$ were observed as shown in Figure 5.8. Notice that in the figure the time axis is logarithmic for highlighting the oscillation cycles. It is of interest to note that in case $\gamma_{AB} = 0.5$, after sufficient simulation time ($t \geq 15.91$ in Figure 5.7(b), (c) and (d)), the same type cells are adjacent to each other by sharing short edges, while different type cells are adjacent by sharing long edges[3]. This phenomenon will be discussed in §5.3.3. In the simulations described in this section, simulation parameters are as follows.

$$\begin{cases} \Delta = 0.01, & \mu = 0.5, \\ l_A = 0, & u_A = \infty, \quad T_A = 0.1. \end{cases} \tag{5.20}$$

where, l_A, u_A and T_A are only used for generating an initial bipartition of $L(S'^0)$.

5.3.1 Standard simulation with fully symmetric G

The kinetic behavior was first observed when the Laguerre diagram D_2 with $\gamma_{AB} = 0.74$ evolved from its initial structure to the structure in which 4% initial cells remained, as shown in Figure 5.9. At the beginning of the simulation, the minority cells were surrounded by the majority. Hence, large minority cells rapidly grew by absorbing their small majority neighbors, meanwhile small minority cells were rapidly absorbed by their large majority neighbors. Due to the rapid growth of large minority cells at the beginning of evolution, the rapid growth of the mean cell radius of A-cells was observed in transient

[3]The similar phenomenon has been observed in two-phase systems, as reported in [Hol93].

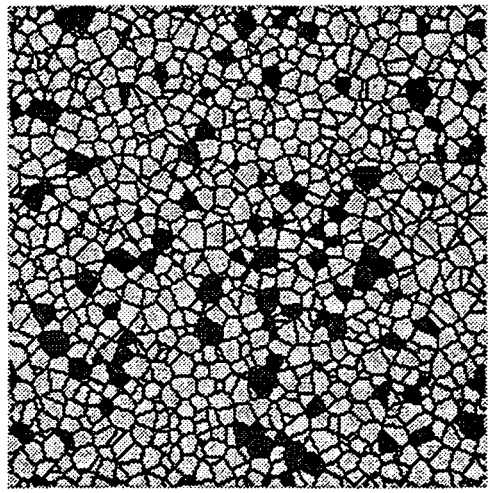

Figure 5.5: Snapshot of the initially bipartitioned Laguerre diagram D_1.

Fig. No.	time	F_A	F_B	R	R_A	R_B	No. cells
5.5	0	0.1068	0.8932	0.0309	0.0310	0.0309	1047
5.6(a)	4.316	0.2514	0.7485	0.0445	0.0547	0.0422	504
5.6(b)	12.22	0.4881	0.5118	0.0695	0.0917	0.0586	207
5.6(c)	25.42	0.6921	0.3078	0.1010	0.1254	0.0755	98
5.6(d)	176.8	0.7265	0.2734	0.2236	0.2460	0.1848	20

Table 5.2: Evolution of D_1 with $\gamma_{AB} = 0.74$.

Fig. No.	time	F_A	F_B	R	R_A	R_B	No. cells
5.5	0	0.1068	0.8932	0.0309	0.0310	0.0309	1047
5.7(a)	5.160	0.5009	0.4990	0.0493	0.0681	0.0406	409
5.7(b)	15.91	0.6700	0.3299	0.0620	0.0795	0.0462	260
5.7(c)	134.8	0.5022	0.4977	0.0940	0.0982	0.0903	113
5.7(d)	985.2	0.5489	0.4510	0.2236	0.2342	0.2123	20

Table 5.3: Evolution of D_1 with $\gamma_{AB} = 0.5$.

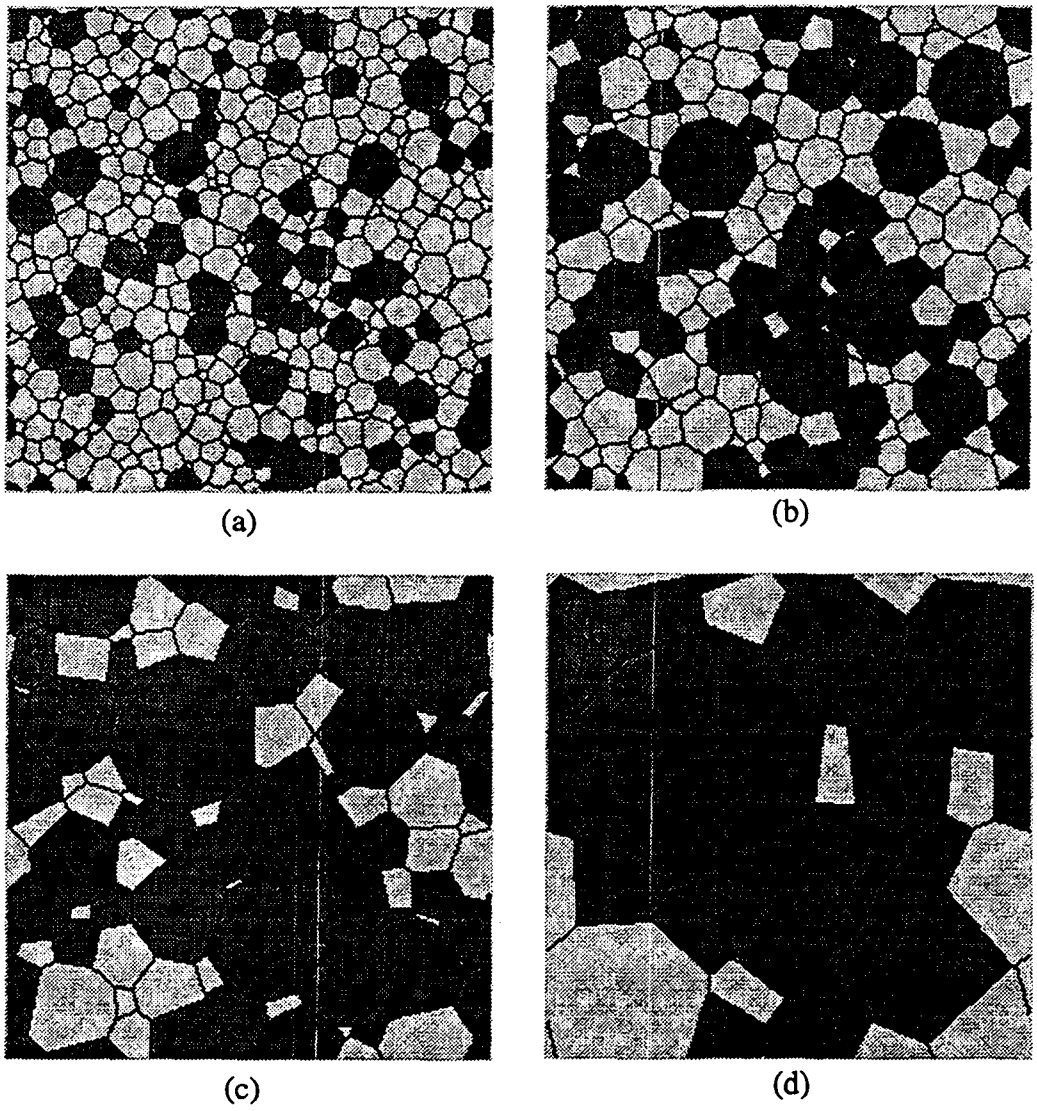

Figure 5.6: Snapshots of the evolution of D_1 with $\gamma_{AB} = 0.74$.

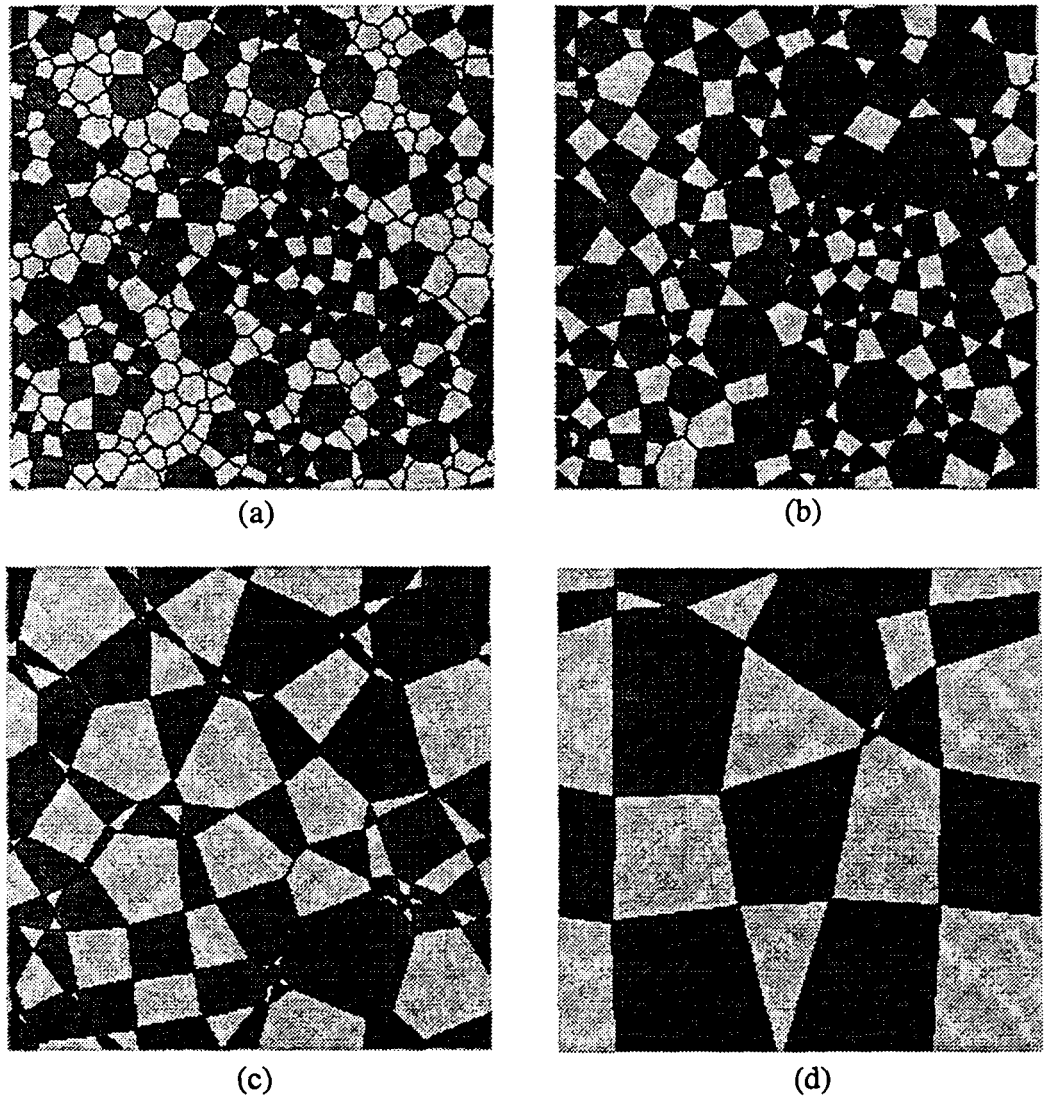

Figure 5.7: Snapshots of the evolution of D_1 with $\gamma_{AB} = 0.5$.

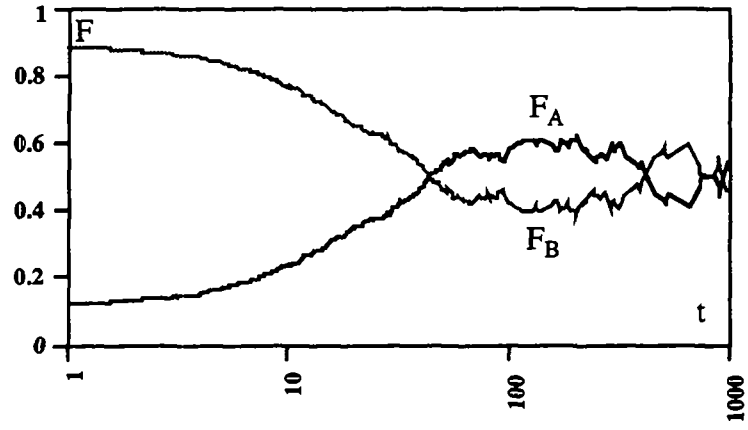

Figure 5.8: The evolution of F_A and F_B in D_1 with $\gamma_{AB} = 0.5$.

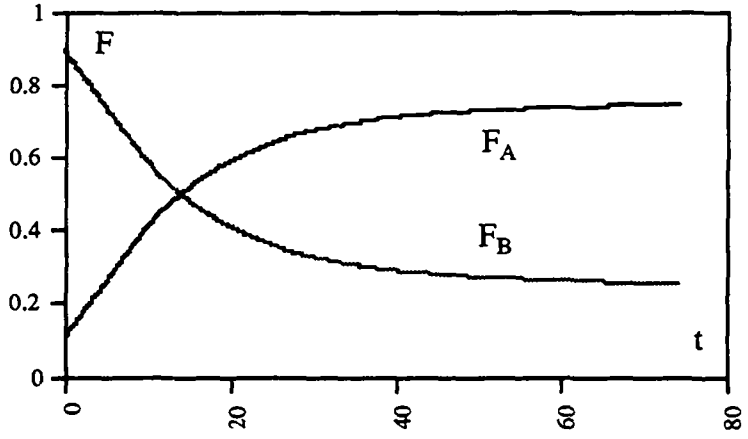

Figure 5.9: The evolution of F_A and F_B in standard simulation ($\gamma_{AB} = 0.74$).

regime (roughly, $0 \leq t \leq 30$) as shown in Figure 5.10. However, the mean cell radius of the cell system, $R(t)$ is very close to the ideal cell radius growth curve, i.e., the grain growth power law, which is shown as the thick line in the figure.

Further simulation showed that if the initial minority population was way below that of the majority, for instance $F_A^0 \leq 0.03$ and l_A, u_A and γ_{AB} were as above, then the minority population would be quickly absorbed by the majority population. Moreover, for a wide range of F_A^0, e.g., $0 < F_A^0 < 0.5$ and l_A, u_A were as above whereas $\gamma_{AB} > 1$ (i.e., Case 3 in Table 5.1), the minority population would disappear sooner or later. After the disappearance of minority population, the remaining was an isotropic grain growth process.

Figure 5.11 shows that the distribution of cell radius $f(r/R)$ is widened over time. While $f(r_A/R)$ and $f(r_B/R)$ have been enormously affected by the competition. For instance, in the initial state the distribution of $f(r_B/R)$ is very close to $f(r/R)$ (since $F_B^0 \doteq 0.9$ in this case), yet in the end of the simulation, $f(r_B/R)$ is pushed to left and its

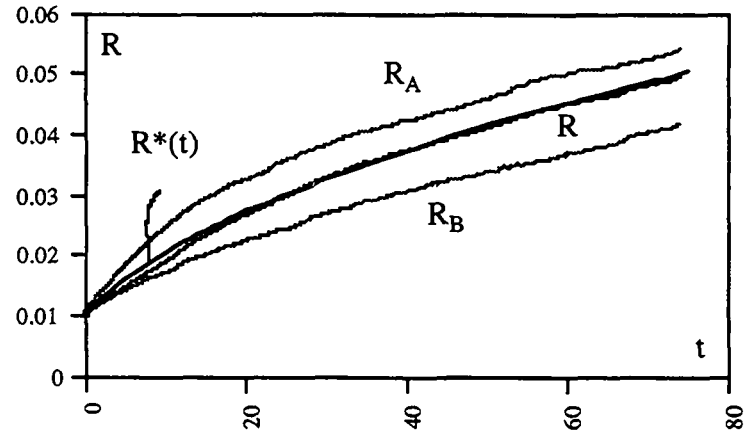

Figure 5.10: The evolution of mean cell radius in standard simulation ($\gamma_{AB} = 0.74$).

mean value is much less than that of $f(r_A/R)$. Considering the dependence of cell side number on its size, i.e., the Lewis law as described in Equation 2.12, it is natural that the distributions of side number of A- and B-cells, $f_A(n)$ and $f_B(n)$ are also seriously affected by the competition as what have happened to $f(r_A/R)$ and $f(r_B/R)$ (see Figure 5.12).

The distribution of coefficient of homologue neighborhood of n-sided A-cell, h_n^A, $n = 3, 4, ...$, at different simulation stage is illustrated in Figure 5.13(a). As in initial state the minority population is randomly distributed, minority cells are isolated from each other. In other words, minority cells are surrounded by the majority. This is why large minority cells can rapidly grow in transient regime. After sufficient evolution, the minority becomes majority, otherwise said, A-cells now cluster. In our simulation, this state occurs at $t = 74.05$, or when 4% of the initial cells remain in the Laguerre diagram. After that, a novel competition cycle starts. This time the minority population is S'_B, for $F_B = 0.2554$. Due to the increase of the mean coefficient of homologue neighborhood, the growth rate of minority population decreases. This implies that the damping of the competition increases with time. In case that the damping increases very slowly, the competition might be oscillation which will be further investigated in §5.3.3. Figure 5.13(b) shows the mean coefficient of homologue neighborhood of A-cell, H^A increases with the simulation time t.

5.3.2 Comparison with experimental results

The texture developing grain growth process observed by Brickenkamp and Lücke [Bri81] can be described as follows: $CuZn$ alloy with 20% Zn was first rolled by 90% reduction of thickness and then the rolling texture appeared. After recrystallization, the material was with a novel texture called recrystallization texture which was very different from the rolling one. During annealing, in the material so-called grain growth texture which was indeed very close to the rolling one was produced. These three textures were basically composed of two types of grains. The grain growth texture has been observed and quan-

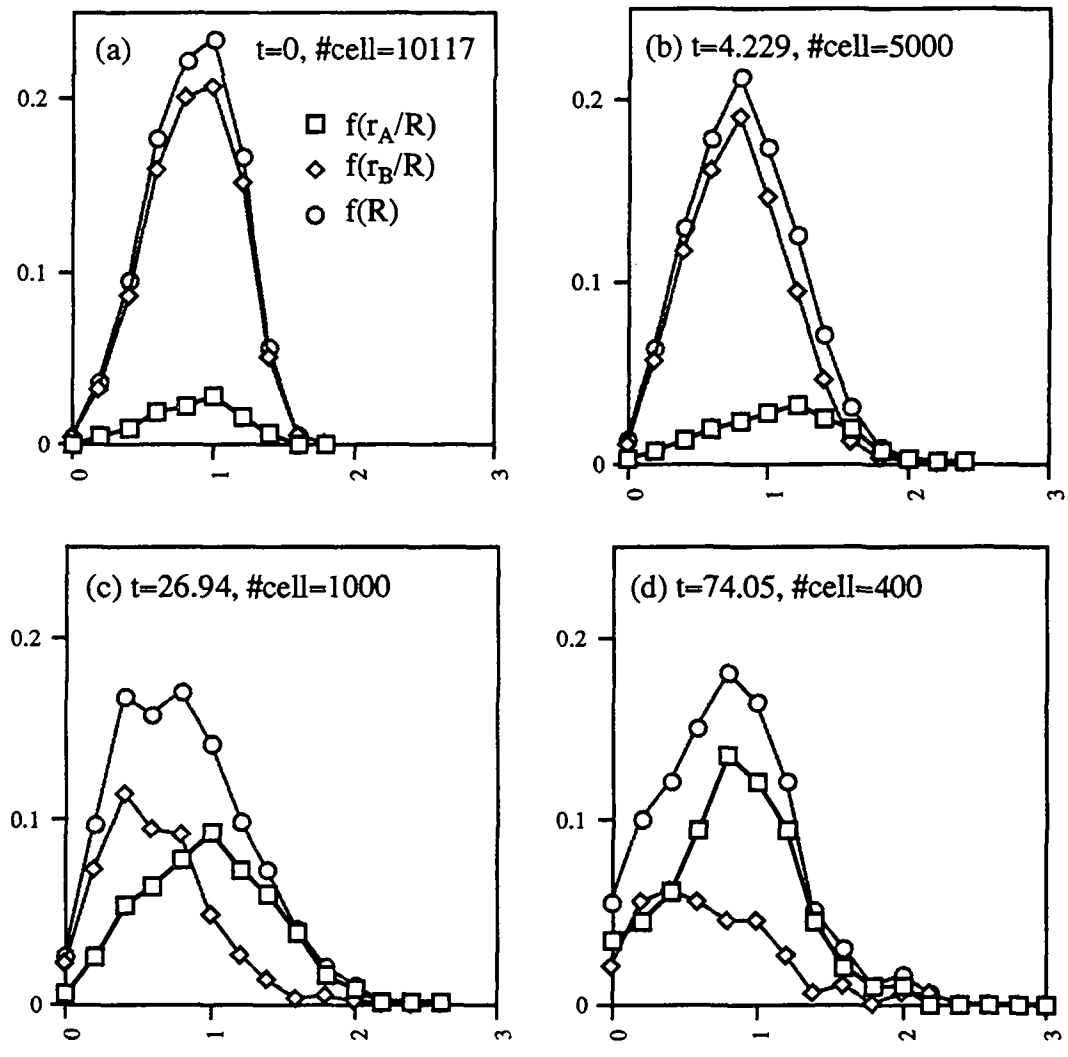

Figure 5.11: Distribution of normalized cell radius at different stages.

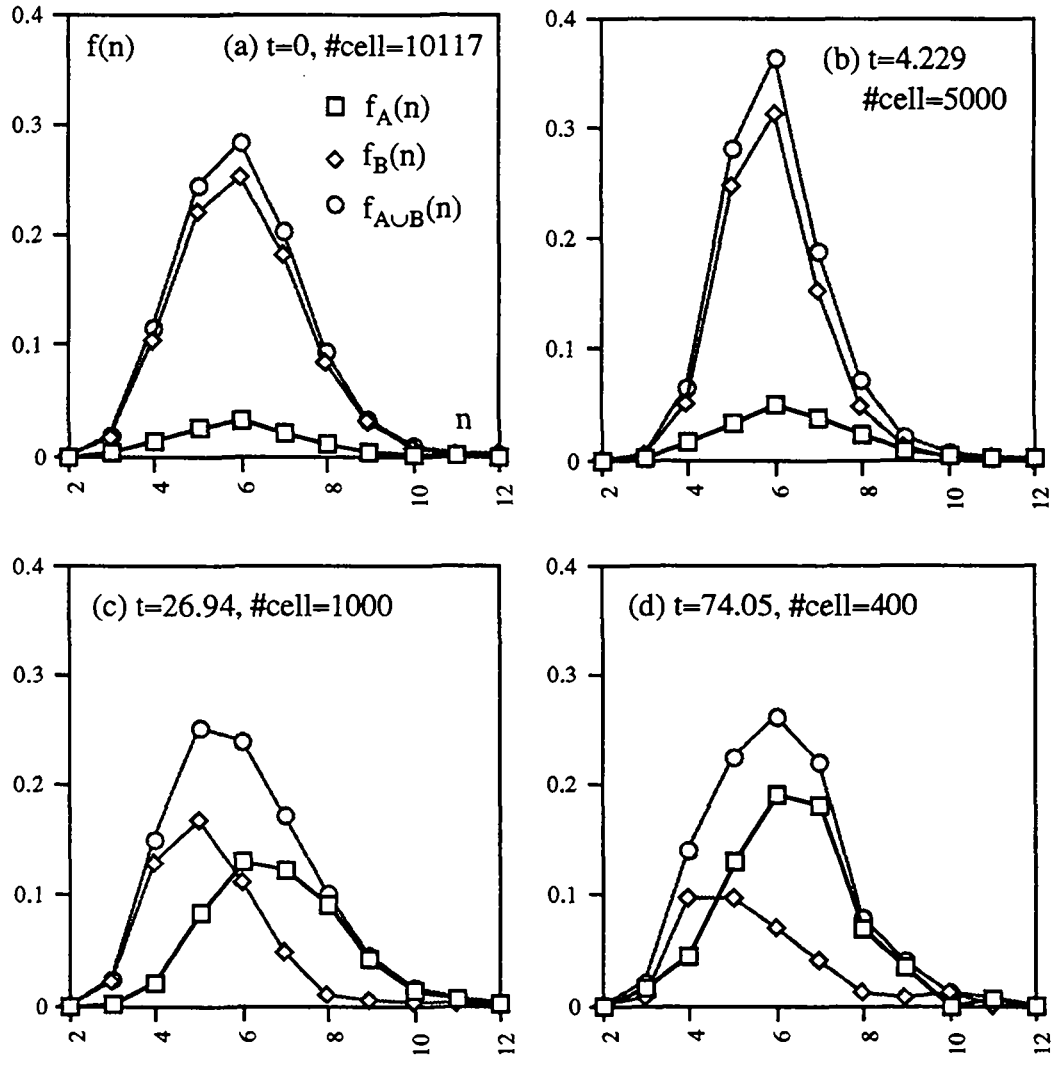

Figure 5.12: Distribution of cell side number at different stages.

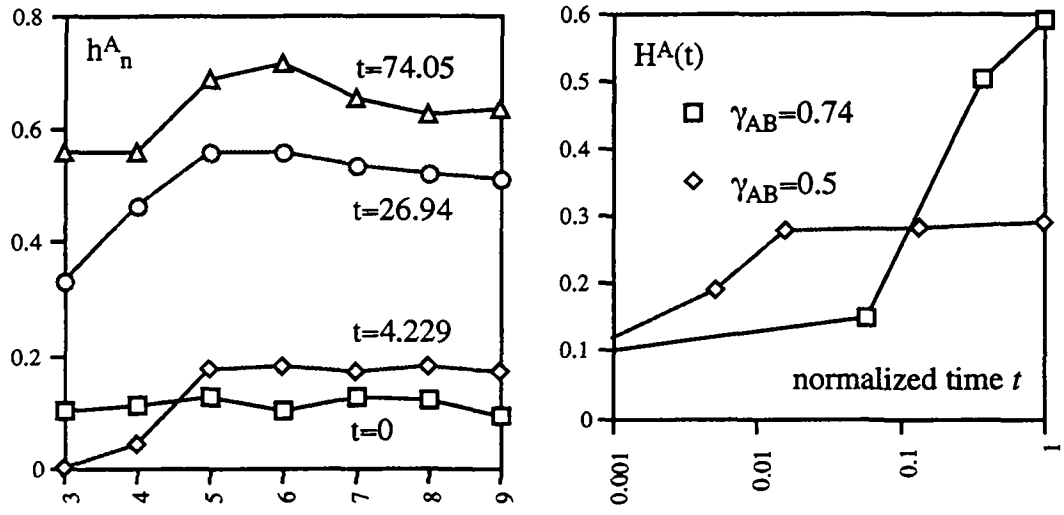

(a) evolution of distribution $h^A{}_n$ (γ_{AB}=0.74) (b) dependence of H^A on t

Figure 5.13: Distribution of h_n^A at different stages.

titatively analyzed as shown in Figures 5.14 and 5.15[4]. Their investigating scale was the normalized mean grain radius increased from 1 to 5, which is referred to as the standard (investigating) scale in our simulation.

To compare the Laguerre simulation to Abbruzzese-Lücke's statistical simulation[5] and the experimental data of α-brass reported in [Bri81], in Figures 5.14 and 5.15, the simulation time and the experiment time is normalized by the time when the mean cell radius is five times as large as the initial one. Figure 5.14 shows that Abbruzzese-Lücke's statistical simulation is always superior to the experimental curve. This may be due to the fact that the geometrical restrictions at the junction of grain boundaries can not be taken into account in the statistical model, or more precisely, that the change of coefficient of homologue cell neighborhood with respect to time is neglected in the model. However, in the Laguerre model such changes are naturally considered. Figure 5.15 shows that the three normalized mean cell radius curves are consistent with each other.

Based on the comparison, it is clearly that the texture developing grain growth process has been approximately fitted by the extended Laguerre model with the simulation parameters given in Equation 5.20 and matrix

$$G = \begin{bmatrix} 1 & 0.74 \\ 0.74 & 1 \end{bmatrix}$$

By carefully tuning γ_{AB} and the initial bipartition parameters, i.e., l_A, u_A and T_A, the fitting might be further improved.

[4]In Figures 5.14 and 5.15, the results are referred to as *Brickenkamp-Lücke*.

[5]In Figures 5.14 and 5.15, Abbruzzese-Lücke's simulation results are referred to as *Abbruzzese-Lücke*.

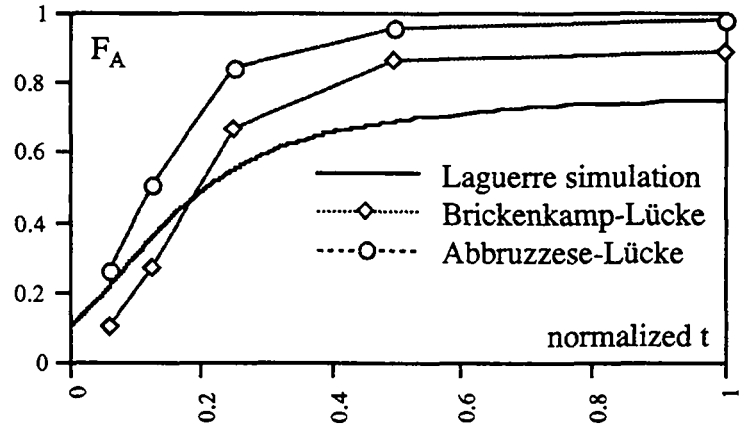

Figure 5.14: Comparison of F_A.

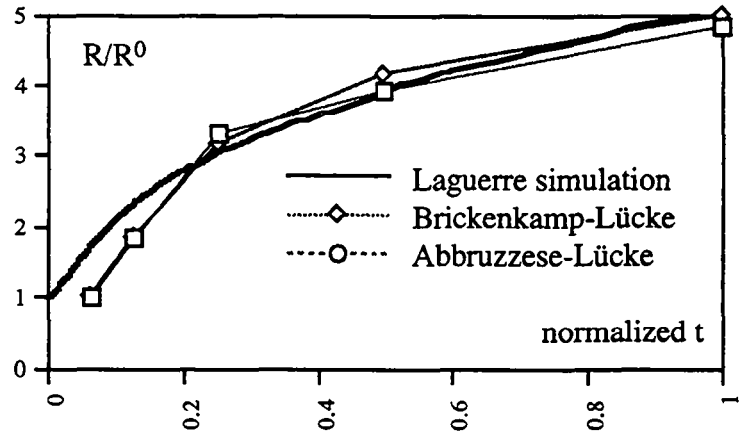

Figure 5.15: Comparison of normalized cell radius.

5.3.3 Long-time simulation with fully symmetric G

As mentioned before, it is very likely that the texture developing grain growth is a damped oscillation process. Thereby, it is of interest to find the controlling parameter in the process. The long time simulation carried on the same initial Laguerre diagrams, D_1 and D_2 is to find such parameter.

Figure 5.16 shows that the average dihedral angle is proportional to the value of γ_{AB}, as indicated in Equations 5.8 and 5.9. Moreover, Figure 5.16(b) shows that if $\gamma_{AB} = 0.5$, after sufficient annealing the same type cells are adjacent by sharing short edges and the different type cells are adjacent by sharing long edges. Figure 5.17 schematically shows two successive states of a 6-sided A-cell and its environ. As $\gamma_{AB}/\gamma_{AA} = 0.5$ and G is fully symmetric, eight Laguerre vertices move in the directions shown by the arrows in Figure 5.17(a). At certain moments between t_1 and t_2, short edges ab is permuted as $a'b'$, cd as $c'd'$, ef as $e'f'$ and gh as $g'h'$ in Figure 5.17(b). If t_1 and t_2 are two sampling instants then one finds that $h_6^A(t_1) = h_6^A(t_2) = 1/3$ for this 6-sided A-cell. From the symmetry of

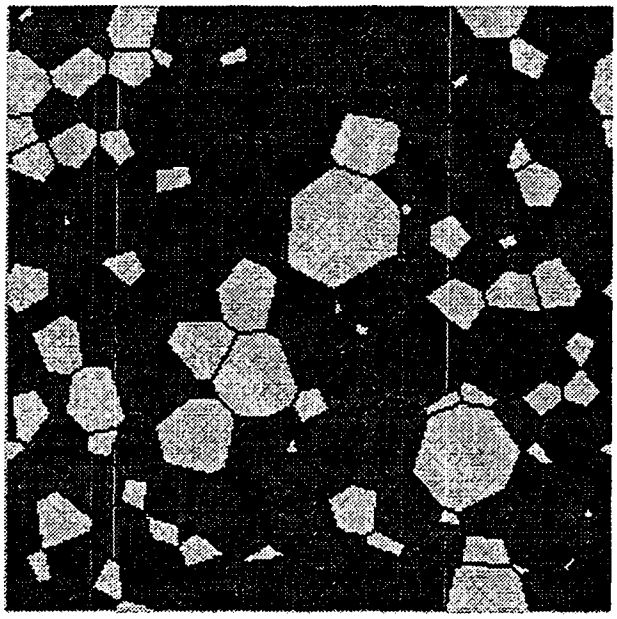

(a) γ_{AB}=0.74, t=155.5, F_A=0.7256

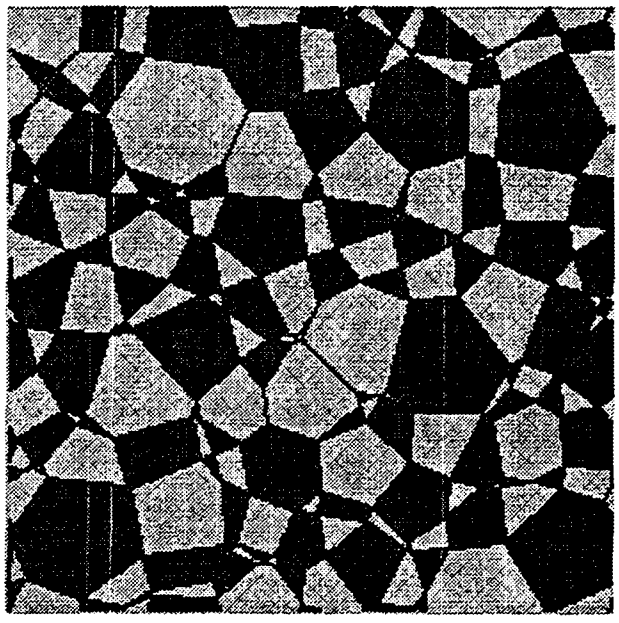

(b) γ_{AB}=0.5, t=896.2, F_A=0.5190

Figure 5.16: Snapshots of final state of D_2 with $\gamma_{AB} = 0.7$ and 0.5.

the cell and its neighbors, at next sampling instant t_3, one may find that edges $a'b'$, $c'd'$, $e'f'$ and $g'h'$ are replaced by ab, cd, ef and gh. Thus, the mean coefficient of homologue neighborhood of the A-cell is almost time-invariant. Figure 5.16(b) shows that almost all cells have the same neighborhood, thus H^A stagnates at a certain level in long term regime. In our simulation, with $\gamma_{AB} = 0.5$, $H^A \doteq 0.3$ in the regime as shown in Figure 5.18(a). The dependence of H^A on γ_{AB} is plotted in Figure 5.18(b) based on simulation of D_2 with different γ_{AB}. It is apparent that H^A increases with γ_{AB}.

The long-time simulation showed that if $\gamma_{AB} = 0.74$, there was only one switching point appearing at time $t = 13.1$ in the investigating scale. After the switching point, A-cells was the majority population in the diagram till the simulation finished, as shown in Figure 5.19. In case that $\gamma_{AB} = 0.5$, four switching points appeared in the same investigating scale, i.e., at time $t = 5.185$, 231.4, 696.2 and 895.7, sequentially. Thereby, three oscillation cycles of F_A (as well as F_B) were observed, as shown in Figure 5.21. Notice that in the figure the time axis is logarithmic.

The simulation makes it clear that the texture developing grain growth is a damped oscillation process and γ_{AB} is the controlling parameter. A critical γ^c_{AB} exists between 0.62 and 0.74 such that if $\gamma_{AB} < \gamma^c_{AB}$, then F_A is oscillated, otherwise said, F_A will have more than one switching point[6]. Even in this case, the oscillation eventuates in an equilibrium, i.e., $F_A = F_B = 0.5$, as long as the process can last to that time. Such tendency clearly appears in Figure 5.21, for the amplitude of the oscillation is continuously decreasing.

Figures 5.20 and 5.22 show the growth kinetics of mean cell radius with $\gamma_{AB} = 0.74$ and 0.5, respectively. In the case of $\gamma_{AB} = 0.74$, the growth curve of mean cell radius of the cell system, $R(t)$ is very close to the ideal growth curve shown as $R^*(t)$ in Figure 5.20. While in the case of $\gamma_{AB} = 0.5$, the curve of $R(t)$ is superior to $R^*(t)$ in transient regime and inferior to $R^*(t)$ in long term regime, as shown in Figure 5.22. It is of interest to note that the curves of $R_A(t)$ and $R_B(t)$ possess three cross points at which $R_A = R_B$. These cross points occuring at $t = 276.6$, 810.2 and 888.8, have been shown in Figure 5.23. To make comparison, the switch points of F_A are plotted on time-axis in the same figure.

The damped oscillation of F_A in texture developing grain growth process is not counterintuitive. As the specific grain boundary matrix G is fully symmetric, the minority population grow more quickly than the majority in case γ_{AB} is sufficiently smaller than γ_{BB}. For instance, suppose $\gamma_{AB}/\gamma_{AA} = 1/\sqrt{2}$ and $\gamma_{AA} = \gamma_{BB}$, then the equilibrium dihedral angles α and β are $\pi/2$ and the isolated cell with five or more sides will expand. Suppose at the beginning of the process A-cells are the minority population and hence isolated, then F_A will increase quickly till the moment when B-cells are surrounded by A-cells. After that moment, a new circle of competition starts. This time, it is B-cell that has the privilege of growth. If there were no damping in the cell system, then a lossless oscillation would occur. Since the same type cells tend to cluster, the mean coefficient of homologue neighborhood of A-cell (B-cell) increases and hence the growth rate of minority large cell decreases. In our simulation, when H^A increased sufficiently slowly (with $\gamma_{AB} = 0.5$), an underdamped oscillation was observed, while H^A increased

[6]The range in which the critical γ^c_{AB} exists could be further precise by more simulations with different γ_{AB}/γ_{AA}.

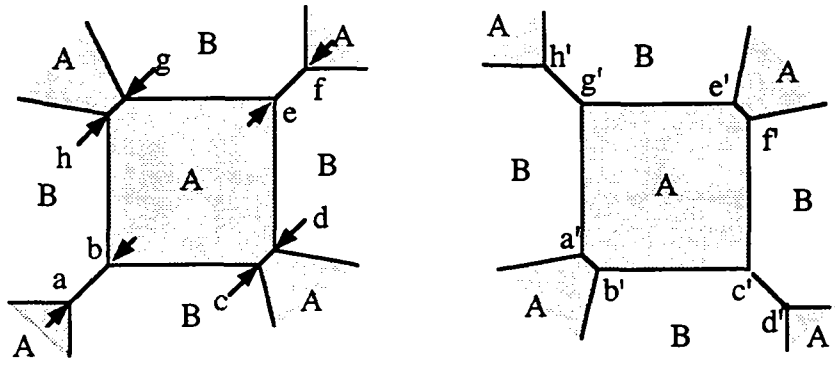

(a) $t=t_1$, $h^A{}_6=1/3$ (b) $t=t_2$, $h^A{}_6=1/3$

Figure 5.17: The neighborhood changes of an A-cell at successive moment ($\gamma_{AB} = 0.5$).

sufficiently quickly (with $\gamma_{AB} = 0.74$), an overdamped oscillation was recored. Based on the simulation and analysis, such conclusions may be drawn that in case G is fully symmetric, the oscillation of the texture developing grain growth process can be controlled by γ_{AB} and the cluster of the same type cells in the process can be quantitatively described by parameters h_n^A (h_n^B) and H^A (H^B).

To our knowledge, this oscillation phenomenon has not been reported either by experiment or by computational simulation. However, with the special grain boundary specific energy matrix G, the oscillatory competition between F_A and F_B is possible as demonstrated in the simulation.

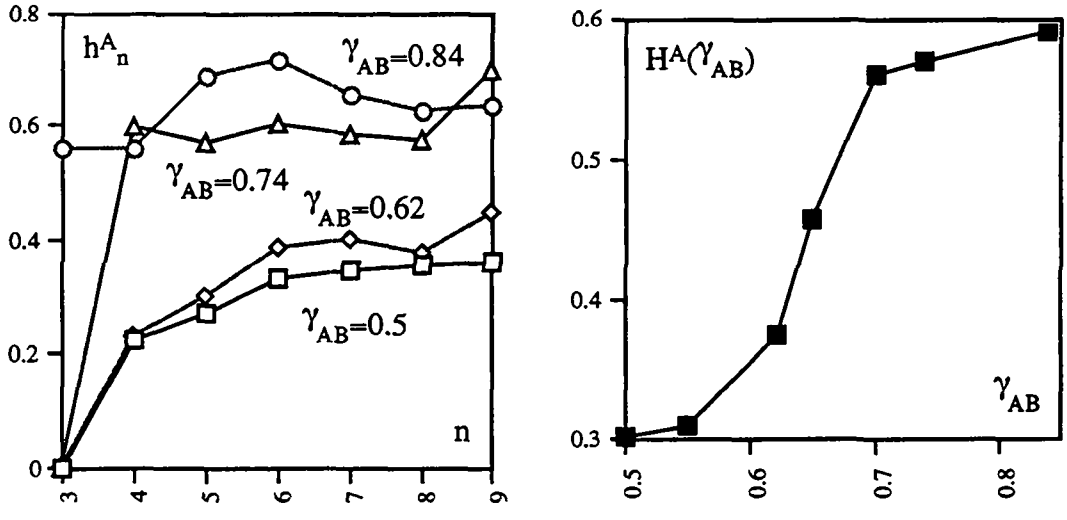

(a) distribution of $h^A{}_n$ under different γ_{AB} (b) dependence of H^A on γ_{AB}

Figure 5.18: Dependence of H^A on γ_{AB}.

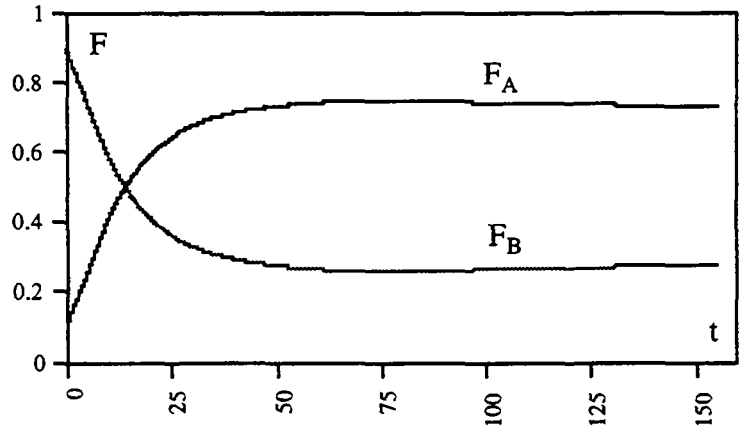

Figure 5.19: Evolution of F_A and F_B in long-time simulation ($\gamma_{AB} = 0.74$).

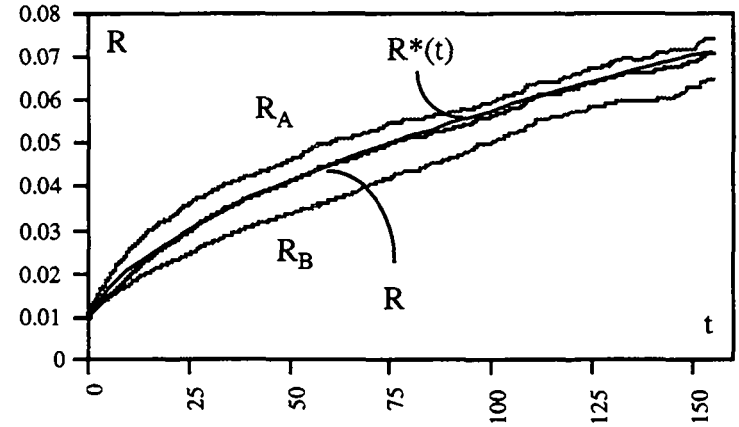

Figure 5.20: Evolution of R_A and R_B in long-time simulation ($\gamma_{AB} = 0.74$).

5.3.4 Long-time simulation with non-fully symmetric G

The cases that specific grain boundary energy matrix G is non-fully symmetric, i.e., Cases 4-9 in Table 5.1 have been investigated. The evolution of Laguerre diagram D_1 and D_2 has been simulated with the parameters given by Equation 5.20 and matrix G_4 to G_9, one after another. The computational results ($F_A(t)$ curve) are summarized in Figure 5.24. To compare different curves, simulation time t has been normalized to 1 in the figure. Notice that a Laguerre vertex may be incident to three A- or B-cells, the driving force exerted on the vertex is thus affected by the value of γ_{AA} and γ_{BB}. Thereby, the two populations possess different privilege of growth in case $\gamma_{AA} \neq \gamma_{BB}$. For instance, in matrix G_5, as $\gamma_{AA}/\gamma_{BB} = 1/2$ and $\gamma_{BB} = 2$, a large ($n > 6$) B-cell in a B-cluster grows more quickly than a large A-cell in a A-cluster. However, the minority population grows more quickly than the majority, for $\gamma_{AB}/\gamma_{BB} = 1/2$. So, finally, B-cells disappear altogether. Concerning matrix G_4, even a large B-cell in a B-cluster grows more quickly and a large A-cell in a A-cluster grows more slowly as $\gamma_{AA}/\gamma_{BB} = 1/4$, the process is still dominated by the

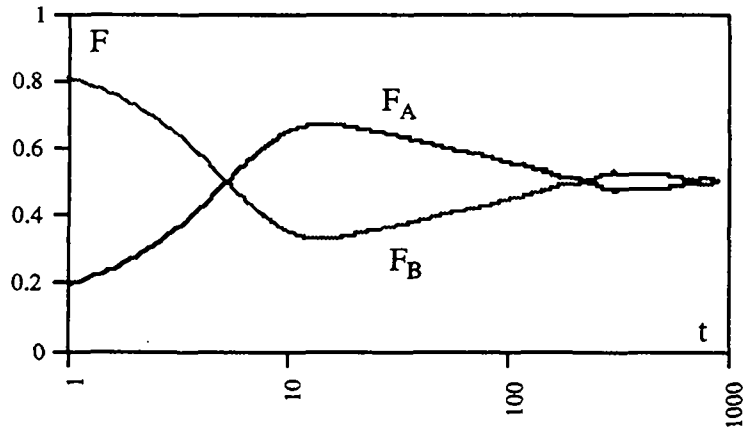

Figure 5.21: Evolution of F_A and F_B in long-time simulation ($\gamma_{AB} = 0.5$).

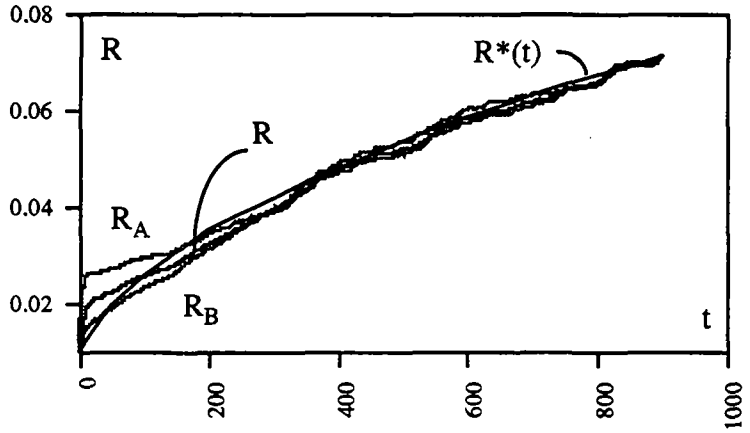

Figure 5.22: The evolution of mean cell radius in long-time simulation ($\gamma_{AB} = 0.5$).

minority population growth. Therefore the final result is the same as with G_5. Matrix G_8 give the privilege of growth to large A cells in A-clusters ($\gamma_{AA}/\gamma_{BB} = 2$). However, at the beginning of the process A-cells are isolated and hence the privilege can not be applied. On the other hand, as $\gamma_{AB}/\gamma_{BB} = 1$, there is no privilege for the minority population. Thus the process stops with a very small A population. With the same privilege for large A-cell in A-cluster ($\gamma_{AA}/\gamma_{BB} = 2$), but no privilege for minority population ($\gamma_{AB}/\gamma_{BB} = 2$), as in Matrix G_9, then A-cells quickly disappear.

In sum, once matrix G is no longer fully symmetric, the oscillation of the process is highly improbable in practice.

5.4 Summary

In this chapter, the 2D Laguerre model for normal grain growth in pure single phase system proposed by Telley, Liebling, Mocellin and Righetti [Tel89a, Tel92a] is extended

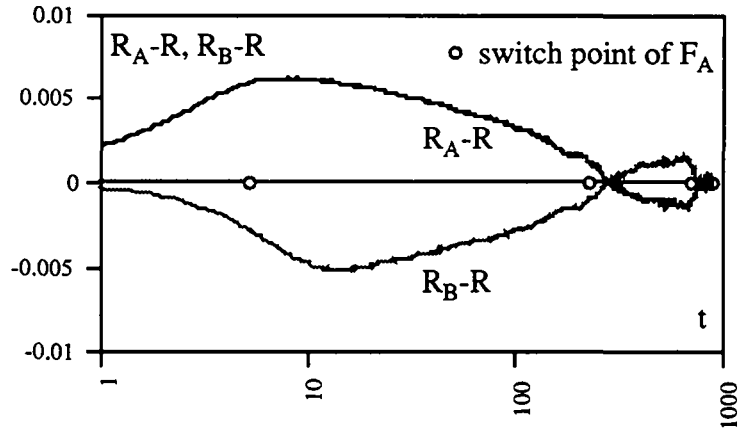

Figure 5.23: Another presentation of evolution of mean cell radius ($\gamma_{AB} = 0.5$).

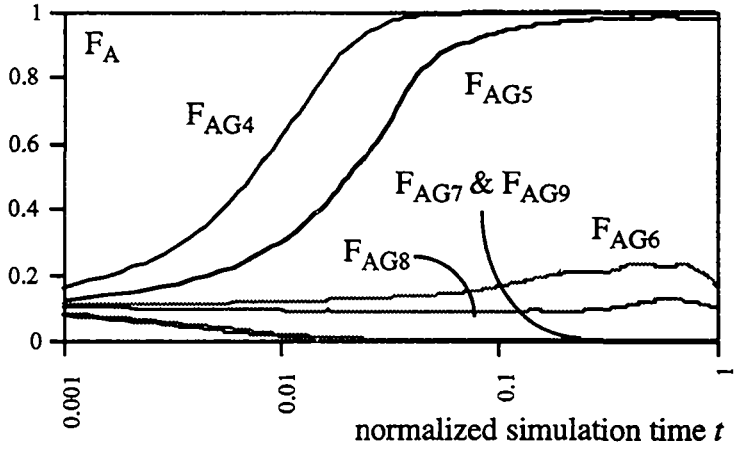

Figure 5.24: The evolution of F_A with different non-fully symmetric matrix G.

to the heterogeneous case. It is known that crystallographic textures are likely to develop under such circumstance.

By Applying this model to the two types of grains case, first simulation results show that the kinetic behavior of the texture developing grain growth process have been approximately reproduced. As the Laguerre simulation can provide the microstructure of the simulated system, it is an important complement of Abbruzzese and Lücke's statistical simulation [Abb86]. The long-time simulations bring to light the nature of competition between these two populations of cells. To our knowledge, this oscillation phenomenon has not been reported either by experiment or by computational simulation.

The cluster of A-cells during the system evolution has been parameterized by h_n^A and H^A. Simulations show that H^A increases with time, in case A-cells are the minority population in the initial state. These parameters strongly depends on γ_{AB}. Therefore, γ_{AB} is the main controlling parameter in the heterogeneous grain growth process, in case matrix G is fully symmetric. On the other hand, Figures 5.13(a) and 5.18(a) show that

h_n^A is not independent of the side number of cell n. However, such dependence has not yet been understood.

As in our model the competition between the two populations can be controlled by the initial bipartition and the specific grain boundary energy matrix G, the further study of this model may provide interesting prompts to the so-called "grain boundary design" [Wat92] of polycrystalline materials.

Chapter 6

Conclusive Remarks

In this study, the dynamic Laguerre and weighted Delaunay diagrams in the three-dimensional unit flat torus have been developed based on the work of Telley, Righetti, Liebling and Mocellin [Tel89a, Tel90, Tel92b, Tel93, Rig92]. It has been shown that given a set $\bar{S}$ of N sites in $\mathbb{T}^3$, by the facet-flip procedure [Rig92], the construction of Delaunay diagram of $\bar{S}$ can be completed in $O(N^3 \log N)$ time. Thereby the procedure is indeed an algorithm. In turn, given a set $\bar{S}'$ of N weighted sites in $\mathbb{T}^3$, the weighted Delaunay diagram of $\bar{S}'$ can be transformed from the unweighted one by linearly increasing site weight from zero to the specific value. The time complexity of the transformation is $O((m+N^2)\log N)$, where m is the number of topological events induced during the transformation. Finally, given a set $\bar{S}'(J)$ of N weighted sites in $\mathbb{T}^3$ and a time interval $J=[0,T]$, the dynamic weighted Delaunay diagram of $\bar{S}'(J)$ can be maintained in $O(\frac{T}{\delta}(m+N^2)\log N)$ time, where m is the maximum of the number of topological events induced in one simulation step, i.e., during $\frac{T}{\delta}$ unit time. The convergence of these algorithms has been proved based on the following assumption: The given weighted site set satisfies the general motion condition. The velocity of site is a linear function of time and in a given time interval each site leaves the canonic unit cube at most $O(1)$ number of times.

With 3D dynamic Laguerre and Delaunay diagrams, the isotropic and anisotropic grain growth in polycrystalline materials has been simulated. Continuing to use the methodology of Telley [Tel89a], a motion equation of weighted site of Laguerre diagram is derived based on Burke and Turnbull's simple kinetic model. The evolution of the Laguerre diagram governed by the motion equation reproduced the main attributes of the physical process, i.e., the grain growth power law, the distribution of grain size and shape and its scaling behavior in long-term regime. So, the eligibility of the 3D Laguerre model for representing grain growth is confirmed by simulation. Assuming the specific grain boundary energy depends on the simulated material crystallography and the misorientation of grains which form the boundary whereas the mobility of grain boundaries is isotropic, the anisotropic grain growth in 3D has been simulated, as well as the distribution of misorientations.

To simulate texture developing grain growth in two dimensions, the 2D Laguerre model [Tel89a] is generalized to the heterogeneous case. Textured grain growth has been simulated in its simplest case, i.e, two types of grains present in the Laguerre diagram. This simulation provides a geometrical evidence for the corresponding statistical theory proposed by Abbruzzese, Lücke and co-workers [Abb86]. The possibility of oscillatory competition between two populations of cells has be evidenced by simulation for the first time.

People are still far away from their goal to predict the grain growth process as a function of annealing conditions. Nevertheless we have full confidence that one day people can, as Shakespeare wrote (Macbeth, Act I, Scene III), "...look into the seeds of time and say which grain will grow and which will not".

Bibliography

[Abb86] G. Abbruzzese, I. Heckelmann and K. Lücke, "A theory of texture controlled grain growth–I. Derivation and general discussion of the model; –II. Numerical and analytical treatment of grain growth in the presence of two texture components", Acta Metall., **34**, 905-914, 1986; **36**, 55-68, 1988

[Abo70] D.A. Aboav, "The arrangement of grains in a polycrystal" Metallography, **3**, 383-390, 1970

[Abo92] D.A. Aboav, "The topology of a polycrystal in three dimensions", Materials Science Forum, **94**, 275-280, 1992

[Alb92] G. Albers and T. Roos, "Voronoi diagrams of moving points in higher dimensional spaces", in Proc. of Third Scandinavian Workshop on Algorithm Theory, Helsinki, Finland, 399-409, 1992

[Alb95] G. Albers, J.S.B. Mitchell, L.J. Guibas and T. Roos, "Voronoi diagrams of motion points", unpublished manuscript, 1995

[And84] M.P. Anderson, D.J. Srolovitz, G.S. Grest, P.S. Sahni, "Computer simulation of grain growth: I. Kinetics, II. Grain size distribution, topology and local dynamics, III. Influence of a particle dispersion, IV. Anisotropic grain boundary energies", Acta Metall., **32**, 783-791, 793-802, 1429-1438, **33**, 509-520, 1984

[And85] J.C. Anderson, "Materials Science", Van Nostrand Reinhold, Workingham, UK, 1985

[And89] M.P. Anderson and G.S. Grest, "Computer simulation of normal grain growth in three dimensions", Phil. Mag., **B59**, 293–329, 1989

[Atk88] H.V. Atkinson, "Theories of normal grain growth in pure single phase systems", Acta Metall., **36**, 469-491, 1988

[Aur87] F. Aurenhammer, "Power diagram: Properties, algorithms and applications", SIAM J. Comput., **16**, 78-96, 1987

[Avr39] M. Avirami, "Kinetics of phase change: General theory", J. Chemical Physics, **7**, 1103-1112, 1939

[Bec54] P.A. Beck, "Annealing of cold worked metals", Adv. Phys., **3**, 245-324, 1954

[Bri81] W. Brickenkamp, K. Lücke, "Texture development during grain growth of rolled and annealed α-brass sheets", Proc. 6th ICOTOM, 570-580, Tokyo, Japan, 1981

[Bur52] J.E. Burke and D. Turnbull, "Recrystallization and grain growth" Progress in Metal Physics, **3**, 218-292, 1952

[Car87] C. Carry and A. Mocellin, "Structural superplasticity in single phase crystalline ceramics", Ceramics International, **13**, 89-98, 1987

[Cot76] P. Cotterill and P.R. Mould, "Recrystallization and Grain Growth in Metals", Surrey University Press, London, UK, 1976

[Dav59] C. Davis, "The set of non-linearity of a convex piecewise-linear function", Scripta Math., **24**, 219-227, 1959

[Del34] B. Delaunay, "Sur la sphère vide", Bulletin de l'Acadamie des Sciences de l'URSS, Classe des Sciences Mathmatiques et Naturelles, 793-800, 1934

[Des83] R. Descartes, "Principles of Philosophy", (translated, with explanatory notes by V.R. Miller, R.P. Miller), D. Reidel, Dordrecht, Holland, 1983

[Dob89] D.P. Dobkin, M.J. Laszlo, "Primitives for the manipulation of three-dimensional subdivisions", Algorithmica, **4**, 3-32, 1989

[Dou93] E.R. Dougherty, "Mathematical Morphology in Image Processing", Dekker, New York, USA, 1993

[Ede87] H. Edelsbrunner, "Algorithms in Combinatorial Geometry", Springer-Verlag, Berlin, Germany, 1987

[Edw94] S.F. Edwards, K.D. Pithia, "A note on the Aboav-Weaire law", Physica, **A 250**, 577-584, 1994

[Fel57] P. Feltham, "Grain growth in metals", Acta Metall., **5**, 97-105, 1957

[For85] M.A. Fortes and A.C. Ferro, "Topology and transformations in cellular structures", Acta Metall., **19**, 1491-1496, 1985

[Fuc95] K. Fuchizaki, T. Kusaba and K. Kawasaki, "Computer modeling of three–dimensional cellular pattern growth", Phil. Mag., **B71**, 333–357, 1995

[Ful52] R.L. Fullman, "Boundary migration during grain growth", in "Metal Interfaces", American Society for Metals, Metals Park, Ohio, USA, 179-207, 1952

[Gol69] H. Goldstein, "Classical Mechanics", Addison-Wesley, Reading, UK, 1969

[Got92] G. Gottstein and F. Schwarzer, "On the orientation dependence of grain boundary energy and mobility", Materials Science Forum, **94**, 187-208, 1992

[Has71] G.C. Hasson and C. Goux, "Interfacial energies of tilt boundaries in aluminium: Experimental and theoretical determination", Scripta Metall., **5**, 889-894, 1971

[Hil65] M. Hillert, "On the theory of normal and abnormal grain growth" Acta Metall., **13**, 227-238, 1965

[Hol93] E.A Holm, D.J. Srolovitz and J.W. Cahn, "Microstructural evolution in two-dimensional two-phase polycrystals", Acta Metall., **41**, 1119–1136, 1993

[Ima85] H. Imai, M. Iri and K. Murota, "Voronoi diagram in the Laguerre geometry and its applications", SIAM J. Comput., **14**, 93–105, 1985

[Isa66] E. Isaacson and H.B. Keller, "Analysis of Numerical Methods", John Wiley, New York, USA, 1966

[Joe89] B. Joe, "Three-dimensional triangulation from local transformations", SIAM J. Sci. Stat. Comput., **10**, 718–741, 1989

[Joe91] B. Joe, "Construction of three-dimensional Delaunay triangulations using local transformations", Computer Aided Geometric Design, **8**, 123-142, 1991

[Joe93] B. Joe, "Construction of K-dimensional Delaunay triangulations using local transformations", SIAM J. Sci. Comput., **14**, 1415-1436, 1993

[Joh39] W.A. Johnson and R.F. Mehl, "Reaction kinetics in processes of nucleation and growth", Trans. AIMME, **135**, 415-458, 1939

[Kaw89] K. Kawasaki, T. Nagai and K. Nakashima, "Vertex models for two-dimensional grain growth", Phil. Mag., **B60**, 399-421, 1989

[Kaw93] K. Kawasaki, T. Nagai, T. Okuzono and K. Fuchizaki, "Computer simulation studies of simplified models of cellular systems", in "Modeling of Coarsening and Grain Growth", C.S. Pande, S.P. Marsh (Eds.), 295-310, TMS, USA, 1993

[Kun93] U. Kunaver and D. Kolar, "Computer simulation of anisotropic grain growth in ceramics", Acta Metall., **41**, 2255-2263, 1993

[Kur80] S.K. Kurtz and F.M.A. Carpay, "Microstructure and normal grain growth in metals and ceramics", J. Appl. Phys., **51**, 5725–5754, 1980

[Kur93] S.K. Kurtz, S. Kumar, J.R. Banavar, H. Zhang, "Normal grain growth in metals and ceramics: constraints of statistical topology and geometry", in "Modeling of Coarsening and Grain Growth", C.S. Pande, S.P. March (Eds.), 167-182, TMS, USA, 1993

[Lee81] D.T. Lee and R.L. Drysdale, "Generalization of Voronoi diagram in plane", SIAM J. Comput., **10**, 73-87, 1981

[Lie92] T.M. Liebling, A. Mocellin, H. Telley, F. Righetti, H. Clémençon and C. Indermitte, "Nouvelles approches dans la modélisation et simulation de processus de croissance en science des matériaux et en biologie", Cahiers du CERO, **34**, 117-138, 1992

[Lie95] T.M. Liebling, A. Mocellin and X. Xue "3D dynamic power diagram polycrystal grain growth models", submitted to Zeitschrift für Angenandte Mathematik und Mechanik, 1995

[Lou74] N.P. Louat, "On the theory of normal grain growth", Acta. Metall., **22**, 721-724, 1974

[Mat94] K. Matsuura, Y. Itoh, M. Kudoh, T. Ohmi and K. Ishii, "Three-dimensional grain size distribution in SUS304 stainless steel", ISIJ International, **34**, 186 (1994)

[Mcm70] P. McMullen, "The maximal number of faces of a convex polytope", Mathematika, **17**, 179-184, 1970

[Mar93] S.P. Marsh, R.A. Masumura and C.S. Pande, "Vertex-based simulation of two-dimensional grain growth", in "Modeling of Coarsening and Grain Growth", C.S. Pande, S.P. March (Eds.), 339-345, TMS, USA, 1993

[Mul89] W.W. Mullins and J. Viñals, "Self-similarity and growth kinetics driven by surface free energy reduction", Acta Metall., **37**, 991–997, 1989

[Mul92] P.A. Mulheran, "Mean field simulation of normal grain growth", Acta Matell., **40**, 1827-1833, 1992

[Nak89] K. Nakashima, T. Nagai, K. Kawasaki, "Scaling behavior of two-dimensional domain growth: Computer simulation of vertex models", J. Stat. Phy., **57**, 759-787, 1989

[Oka92] A. Okabe, B. Boots and K. Sugihara, "Spatial Tessellations: Concepts and Applications of Voronoi Diagrams", John Wiley, Chichester, UK, 1992

[Ran92] V. Randle, "Microtexture Determination and Its Applications", The Institute of Materials, London, UK, 1992

[Rhi74] F.N. Rhines and K.R. Craig, "Mechanism of steady-state grain growth in aluminum", Metall. Trans., **5**, 413–425, 1974

[Rig89] F. Righetti, T.M. Liebling and A. Mocellin, "The use of large scale Potts pseudo-atomic model fro 3D grain growth simulation", Acta Stereol., **8**, 459–464, 1989

[Rig92] F. Righetti, "Modélisation 3-D d'amas polycristallins et methodologie d'analyse de leurs images microscopiques", Thèse 1016, Département de Mathématiques, Ecole Polytechnique Fédérale de Lausanne, Switzerland, 1992

[Riv83] N. Rivier, "On the structure of random tissues of froths, and their evolution", Phil. Mag., **B47**, L45-L49, 1983

[Roo91] T. Roos, "Dynamic Voronoi diagrams", PhD Thesis, University of Würzburg, Germany, 1991

[Smi48] C.S. Smith, "Grains, phases, and interfaces: an interpretation of microstructure", Trans. Met. Soc., AIME, **175**, 15-51, 1948

[Smi52] C.S. Smith, "Grain shapes and other metallurgical applications of topology", in "Metal Interfaces", American Society for Metals, Metals Park, Ohio, USA, 65-108, 1952

[Soa85] A. Soares, A.C. Ferro and M.A. Fortes, "Computer simulation of grain growth in a bidimensional polycrystal", Scripta Metall., **19**, 1491–1496, 1985

[Sug94] K. Sugihara, "Robust Grift wrapping for the three–dimensional convex hull", J. Computer and System Sciences, **49**, 391-407, 1994

[Tel89a] H. Telley, "Modélisation et simulation bidimensionnelle de la croissance des polycristaux", Thèse 780, Département de Mathématiques, Ecole Polytechnique Fédérale de Lausanne, Switzerland, 1989

[Tel89b] H. Telley, A. Mocellin and T.M. Liebling, "2D grain growth viewed as a purely topological phenomenon: Models and computational results", Acta Stereol., **8**, 453-458, 1989

[Tel90] H. Telley, "Static and dynamic weighted Delaunay triangulation in the Euclidean space and in the flat torus: Properties, algorithms and applications", Report UIUCDCS-R-90-1662, Univ. of Illinois, Urbana-Champaign, IL, USA, 1990

[Tel92a] H. Telley, T.M. Liebling, A. Mocellin and F. Righetti, "Simulating and modeling grain growth as the motion of a weighted Voronoi diagram", Materials Science Forum, **94**, 301–306, 1992

[Tel92b] H. Telley, "Delaunay triangulations in the flat torus", Technical Report RO 920929, Département de Mathématiques, Ecole Polytechnique Fédérale de Lausanne, Switzerland, 1992

[Tel93] H. Telley, T.M. Liebling and A. Mocellin, "The Laguerre model of grain growth", Technical Report RO 931024, Département de Mathématiques, Ecole Polytechnique Fédérale de Lausanne, Switzerland, 1993

[Ver75] J.D. Verhoeven, "Fundamentals of Physical Metallurgy", John Wiley and Sons, New York, USA, 1975

[Von52] J. von Neumann, "Written discussion on grain topology and the relationship to growth kinetics", in "Metal Interfaces", American Society for Metals, Metals Park, Ohio, USA, 108-113, 1952

[Vor07] G. Voronoi, "Nouvelles applications des parametres continus la theorie des formes quadratique", Journal für die Reine und Angewandte Mathematik, **133**, 97-178, 1907, **134**, 198-287, 1908, and **136**, 67-178, 1909

[Wat92] T. Watanabe, "Grain boundary character distribution (GBCD) analysis of grain growth-related phenomena in polycrystalline materials", Materials Science Forum, **94**, 209-220, 1992

[Wea74] D. Weaire, "Some remarks on the arrangement of grains in a polycrystal" Metallography, **7**, 157-160, 1974

[Wea84] D. Weaire and N. Rivier, "Soap, cells, and statistics-random patterns in two dimensions", Contemporary Physics, **25**, 59-99, 1984

[Whi86] P. Whittle, "Systems in Stochastic Equilibrium", John Wiley, Chichester, UK, 1986

[Wil52] W.M. Williams, C.S. Smith, "A study of grain shape in an aluminium alloy and other applications of stereoscopic microradiography", Trans. AIME, **194** 755-765, 1952

[Wol92] D. Wolf and S. Yip (Eds.), "Materials Interfaces: Atomic-Level Structure and Properties", Chapman & Hall, London, UK, 1992

[Xue94] X. Xue, H. Telley and T.M. Liebling, "First Results on 3D simulation grain growth using Laguerre diagrams", Proc. of 14th IMACS World Congress on Computational and Applied Mathematics, Atlanta, GA, USA, 1007-1012, 1994

[Xue95] X. Xue, T.M. Liebling and A. Mocellin, "First simulation results on anisotropic grain growth with Laguerre model", accepted by Materials Science Forum, 1995

Index

Curriculum Vitae

Name:	Xinjian XUE
Address:	34, Rue du Center, 1025 Saint-Sulpice VD
Birth Date:	December 6, 1954
Birth place:	Jiangsu, China
Nationality:	Chinese
Civil Status:	Married

Education:

1. Diploma in Electrical Engineering, Shanghai University of Technology, China, 1978
2. M.S. in Electrical Engineering, Shanghai University of Technology, China, 1987
3. Cours postgrade en informatique technique "Réseaux de Neurones Biologiques et Artificiels", Département d'Informatiques, Ecole Polytechnique Fédérale de Lausanne, 1991
4. Cours postgrade en rechecrche opérationnelle "Optimisation et Applications", Département de Mathématiques, Ecole Polytechnique Fédérale de Lausanne, 1995

Professional Experience:

1978-1983	Assistant, Department of Electrical Engineering, Shanghai University of Technology, Shanghai, China
1987-1991	Lecturer, Department of Electrical Engineering, Shanghai University of Technology, Shanghai, China
1991-1995	Assistant à l'Ecole Polytechnique Fédérale de Lausanne, Département de Mathématiques, Chaire de Recherche Opérationnelle, Prof. Th.M. Liebling